Experimental Studies of Zero Pressure-Gradient Turbulent Boundary-Layer Flow

by

Jens M. Österlund

Department of Mechanics

Typsatt i $\mathcal{AMS}$-LaTeX med KTHs *thesis*-stil.

Jens M. Österlund 1999 Experimental studies of zero pressure-gradient turbulent boundary layer flow

Department of Mechanics, Royal Institute of Technology
SE-100 44 Stockholm, Sweden

Abstract

This thesis deals with the problem of high Reynolds number zero pressure-gradient turbulent boundary layers in an incompressible flow without any effects of heat-transfer. The zero-pressure gradient turbulent boundary layer is one of the canonical shear flows important in many applications and of large theoretical interest. The investigation was carried out through an experimental study in the MTL wind-tunnel at KTH, where the fluctuating velocity components and the fluctuating wall-shear stress in a turbulent boundary layer were measured using hot-wire and hot-film anemometry. Attempts were made to answer some basic and "classical" questions concerning turbulent boundary boundary layers.

The classical two layer theory was confirmed and constant values of the slope of the logarithmic overlap region (*i.e.* the von Kármán constant) and the additive constants were found and estimated to $\kappa = 0.38$, $B = 4.1$ and $B_1 = 3.6$ ($\delta = \delta_{95}$). The inner limit of overlap region was found to scale on the viscous length scale (ν/u_τ) and was estimated to be $y^+ = 200$, *i.e.* considerably further out compared to previous knowledge. The outer limit of the overlap region was found to scale on the outer length scale and was estimated to be $y/\delta = 0.15$. This also means that a universal overlap region only can exist for Reynolds numbers of at least $Re_\theta \approx 6000$. The values of the newly determined limits explain the Reynolds number variation found in some earlier experiments.

Measurements of the fluctuating wall-shear stress using the hot-wire-on-the-wall technique and a MEMS hot-film sensor show that the turbulence intensity $\tau_{\mathrm{r.m.s.}}/\tau_w$ is close to 0.41 at $Re_\theta \approx 9800$.

A numerical and experimental investigation of the behavior of double wire probes were carried out and showed that the Péclet number based on wire separation should be larger than about 50 to ensure an acceptably low level of thermal interaction.

Results are presented for two-point correlations between the wall-shear stress and the streamwise velocity component for separations in both the wall-normal-streamwise plane and the wall-normal-spanwise plane. Turbulence producing events are further investigated using conditional averaging of isolated shear-layer events. Comparisons are made with results from other experiments and numerical simulations.

Descriptors: Fluid mechanics, turbulence, boundary layers, high Reynolds number, zero-pressure gradient, hot-wire, hot-film anemometry, oil-film interferometry, structures, streak spacing, micro-electro-mechanical-systems.

Preface

This thesis is an experimental study of high Reynolds number zero pressure-gradient turbulent boundary layer flow and is based on the following papers.

Paper 1. Österlund, J. M., Johansson, A. V., Nagib, H. M. & Hites, M. H. 1999 A note on the overlap region in turbulent boundary layers. Accepted for publication in *Phys. of Fluids.*

Paper 2. Österlund, J. M., Johansson, A. V., Nagib, H. M. & Hites, M. H. 1999 Mean-flow characteristics of High Reynolds Number Turbulent Boundary Layers from Two Facilities. To be submitted.

Paper 3. Österlund, J. M. & Johansson, A. V. 1999 Turbulence Statistics of Zero Pressure-Gradient Turbulent Boundary Layers. To be submitted.

Paper 4. Bake, S. & Österlund, J. M. 1999 Measurements of skin-friction fluctuations in turbulent boundary layers with miniaturized wall-hot-wires and hot-films. Submitted to *Phys. of Fluids.*.

Paper 5. Österlund, J. M. & Johansson, A. V. 1994 Dynamic behavior of hot-wire probes in turbulent boundary layers. Published in Advances in turbulence V, 398–402, 1995.

Paper 6. Österlund, J. M., Lindgren, B. & Johansson, A. V. 1999 Structures in zero pressure-gradient turbulent boundary layers. To be submitted.

Paper 7. Österlund, J. M. & Johansson, A. V. 1999 Turbulent Boundary Layer Experiments in the MTL Wind-Tunnel.

Contents

CHAPTER 1

Introduction

Whenever a fluid flows over a solid body, such as the hull of a ship or an aircraft, frictional forces retard the motion of the fluid in a thin layer close to the solid body. The development of this layer is a major contributor to flow resistance and is of great importance in many engineering problems.

The concept of a *boundary layer* is due to Prandtl (1904) who showed that effects of friction within the fluid (viscosity) are present only in a very thin layer close to the surface. If the flow velocity is high enough the flow in this layer will eventually become unordered, swirling and chaotic or simply described as being *turbulent*. The transition from laminar to turbulent flow state was first investigated by Reynolds (1883) who made experiments on the flow of water in glass tubes visualizing the flow state using ink as a passive marker. He found that the flow state was determined solely by a non-dimensional parameter that is since then called the *Reynolds number*. The Reynolds number is a measure of the ratio between inertial and viscous forces in the flow, *i.e.* a high Reynolds number flow is dominated by inertial forces.

The motion of a fluid is governed by the Navier-Stokes equations, named after Navier and Stokes who first formulated them in 1845. The Navier-Stokes equations are nonlinear and time dependent partial differential equations and only a few analytical solutions exist for simple flows. No analytical solutions exist for turbulent flows and to solve the equations for turbulent flows one has to do numerical simulations. The computational effort increases rapidly with increasing Reynolds number and for most practical engineering flow cases it is not possible to solve the full problem numerically even with todays most powerful super-computers. Therefore, one usually makes a simplification of the problem by splitting the velocity field into a mean and a fluctuating part, as first done by Reynolds (1895), and averaging the equations over time. The resulting statistical description is the Reynolds averaged equations. This new set of equations is not closed, new terms appears in the averaging process and they need to be modeled. The statistical quantities needed in models can be determined from simple low Reynolds number flows using direct numerical simulations (DNS) or from experiments.

The Reynolds number in typical engineering applications with boundary layer flow are often several orders of magnitude larger than what is possible
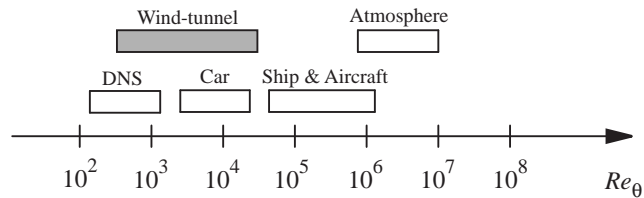
FIGURE 1.1. Typical Reynolds number in applications and attainable in lab facilities and simulations.

to achieve in direct numerical simulations or even compared to what is achievable in most experiments, see figure 1.1. Therefore, there is a gap in Reynolds number between practical applications and the experiments which form the basis for our knowledge of turbulence and turbulence modeling. Experiments at high Reynolds number is therefore of primary importance to reveal Reynolds number trends that might have a large influence in many fluid dynamic applications.

In the present study experiments on turbulent boundary layer flow with zero-pressure-gradient have been performed using hot-wire and hot-film measurement techniques. The goal was to extend the current knowledge of turbulent flows into high Reynolds number regime and to generate a database available to the research community.
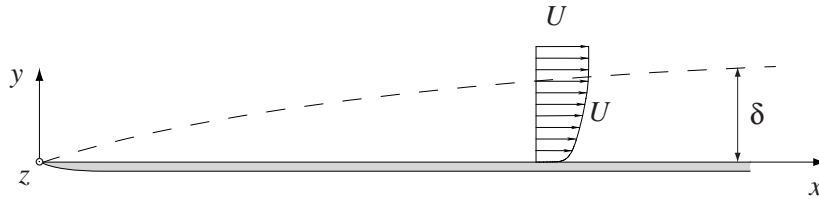
Basic concepts

FIGURE 2.1. Turbulent boundary layer with thickness δ and free-stream velocity U_∞ (vertical scale greatly expanded).

We here consider a turbulent flow in the immediate vicinity of a wall generated by the uniform flow of a free-stream (with the velocity U_∞) of a viscous incompressible fluid. The origin of the co-ordinate axes is placed at the leading edge of the wall. The x-axis is oriented in the streamwise direction, the y-axis in the wall normal direction and the z-axis in the direction parallel to the leading edge, see figure 2.1. The wall is considered to be infinitely wide in the spanwise (z) direction and infinitely long in the streamwise (x) direction. The flow conditions in the spanwise direction are uniform, in the statistical sense, with respect to the z-axis.

The flow is governed by the incompressible *Navier-Stokes equations* and the continuity equation, which are given by

$$\frac{\partial U_i}{\partial t} + U_j \frac{\partial U_i}{\partial x_j} = -\frac{1}{\rho}\frac{\partial P}{\partial x_i} + \nu \frac{\partial^2 U_i}{\partial x_j^2} \tag{2.1}$$

$$\frac{\partial U_i}{\partial x_i} = 0 \tag{2.2}$$

where U_i is the velocity vector, P is the pressure, and ρ and ν are the density and kinematic viscosity of the fluid. Summation is implied over repeated indices.

In the turbulent boundary layer the velocity components fluctuate randomly with respect to time and space around a mean value. This leads naturally to the Reynolds decomposition of the velocity into a mean and a fluctuating

part. The velocity components for, the zero pressure-gradient boundary layer, in the different co-ordinate directions can thus be introduced, in the streamwise direction

$$U(x, y, z, t) = \overline{U}(x, y) + u(x, y, z, t), \tag{2.3}$$

in the wall normal direction

$$V(x, y, z, t) = \overline{V}(x, y) + v(x, y, z, t), \tag{2.4}$$

and in the spanwise direction

$$W(x, y, z, t) = w(x, y, z, t), \tag{2.5}$$

where the mean values are designated by an overbar and the fluctuating part by small letters. The same kind of decomposition is also used for the pressure

$$P(x, y, z, t) = \overline{P}(y) + p(x, y, z, t) \tag{2.6}$$

where the x dependence for P disappears by definition of the problem.

For statistically steady turbulence averaging can be done either in the homogeneous z direction or as a time average. In the present case the averaged value of a quantity is simply defined by

$$\overline{Q}(x, y) = \lim_{T \to \infty} \frac{1}{T} \int_0^T Q(x, y, z, t') dt' \tag{2.7}$$

where the z dependence disappears because it is a homogeneous direction.

2.1. Boundary layer equations

Equations for the flow in the boundary layer are derived by insertion of the Reynolds decomposition (2.3–2.5) into the Navier-Stokes equations 2.1 and subsequent averaging yield the Reynolds averaged equations and the mean continuity equation. [1] With the standard boundary layer approximations of negligible streamwise diffusion and constant pressure through the boundary layer we obtain

$$\overline{U}\frac{\partial \overline{U}}{\partial x} + \overline{V}\frac{\partial \overline{U}}{\partial y} = \frac{\partial}{\partial y}\left(-\overline{uv} + \nu\frac{\partial \overline{U}}{\partial y}\right) \tag{2.8}$$

$$\frac{\partial \overline{U}}{\partial x} + \frac{\partial \overline{V}}{\partial y} = 0. \tag{2.9}$$

The corresponding boundary conditions are

$$\overline{U}(x, y = 0) = \overline{V}(x, y = 0) = 0, \tag{2.10}$$

$$\overline{U}(x, y \to \infty) = U_\infty. \tag{2.11}$$

This set of equations are indeterminate since there are more unknowns than equations. This is known as the closure problem and additional relations or

---

[1] The analysis below was worked out jointly with prof. A. Johansson

hypotheses concerning the Reynolds stress $-\overline{uv}$ is needed to close this set of equations.

Full similarity of the mean velocity profile, like the solutions for a laminar boundary layer, does not exist for the turbulent boundary layer. Instead, we seek similarity solutions for the velocity profiles in the inner and outer regions of the boundary layer separately.

In the works of von Kármán (1921, 1930), Prandtl (1927, 1932) and Millikan (1938) we find the classical theories for the turbulent boundary layer. Discussions of the classical theories can be found in Hinze (1975), Tennekes & Lumely (1972), Schlichting (1979) and Landahl & Mollo-Christensen (1987). There exists numerous refinements and competing theories in the literature and the works of Coles (1956, 1962), Clauser (1956) Barenblatt (1993); Barenblatt & Prostokishin (1993); Barenblatt & Chorin (1999), George *et al.* (1997), Rotta (1950, 1962) and Zagarola *et al.* (1997); Zagarola & Smits (1998b,a), may be consulted.

2.2. Inner region

The inner layer was first treated in the classical work by Prandtl (1932). We define the governing length scale to be $l_* = \nu/u_\tau$, where $u_\tau^2 = \tau_w/\rho$, τ_w is the wall shear stress, and derive a normalized wall distance $y^+ = y/l_* = yu_\tau/\nu$. We assume outer geometrical restrictions (*i.e.* the outer length scale) to be of negligible influence sufficiently close to the wall, and assume the velocity and Reynolds shear stress profiles to be universal functions of y^+

$$\frac{\overline{U}}{u_\tau} = f(y^+) \tag{2.12}$$

and

$$-\frac{\overline{uv}}{u_\tau^2} = g(y^+). \tag{2.13}$$

It is easily seen that the leading order balance obtained from the boundary layer equations 2.8 is given by

$$0 = f'' + g', \tag{2.14}$$

which can be integrated once

$$f'(y^+) = -g(y^+) + f'(0) = -g(y^+) + 1 \tag{2.15}$$

which is seen to be compatible with the 'law-of-the-wall' assumptions 2.12 and 2.13.

2.3. Outer region

For the outer layer description we define a governing length scale Δ, where Δ is some measure of the boundary layer thickness. A normalized wall distance

can be formed as $\eta = y/\Delta$. Assume that we can expand the normalized mean velocity in a straight forward asymptotic expansion

$$\frac{\overline{U}}{U_\infty} \;=\; F(\eta, Re_*) \;\sim\; F_0(\eta) + \varepsilon_1(Re_*)F_1(\eta) + \varepsilon_2(Re_*)F_2(\eta) + \ldots \quad (2.16)$$

where F_i are of order unity and ε_i are gauge functions such that $\varepsilon_{n+1} = o(\varepsilon_n)$, see *e.g.* Hinch (1991). The gauge functions are assumed to approach zero as the Reynolds number Re_* tends to infinity. Also assume

$$\frac{-\overline{uv}}{u_\tau^2} = G_0(\eta) + h.o.t. \tag{2.17}$$

If the velocity scale for the normalization of the Reynolds shear stress is left open, or chosen as different from u_τ (see George *et al.* 1997) consistency would require that the ratio u_τ/U_∞ has to be assumed to approach a constant at infinite Reynolds numbers.

2.4. Overlap region

For (infinitely) large Reynolds numbers the description (2.12,2.13) for $y^+ \to \infty$ should coincide with that given by (2.16,2.17) for $\eta \to 0$. This is the classical two-layer hypothesis of Millikan (1938). Hence, for large enough Reynolds numbers there should be an overlap region

$$l_* \ll y \ll \Delta \tag{2.18}$$

where both descriptions are valid simultaneously. The matching of the Reynolds shear stress simply gives that g and G_0 should be constant (and equal) in the overlap region.

In the classical approach for the matching of the velocity we first construct the normalized velocity gradient

$$\frac{y}{u_\tau} \frac{\partial \overline{U}}{\partial y}. \tag{2.19}$$

This non-dimensional measure should be the same in the outer and the inner layer description in the overlap region, *i.e.*

$$\frac{y}{u_\tau} \frac{\partial \overline{U}}{\partial y} = y^+ f'(y^+) = \frac{U_\infty}{u_\tau} \eta F_0'(\eta) + \varepsilon_1 \frac{U_\infty}{u_\tau} \eta F_1'(\eta) = const. \tag{2.20}$$

From this approach we get the overlap velocity distribution given by

$$y^+ f'(y^+) = const = \frac{1}{\kappa} \tag{2.21}$$

resulting in the log-law

$$f = \frac{1}{\kappa} \ln y^+ + B \tag{2.22}$$

and for both sides of (2.20) to be of the same order of magnitude we get

$$F_0' = 0 \quad \Rightarrow \quad F_0 = const (= 1) \tag{2.23}$$

and

$$\varepsilon_1 = \frac{u_\tau}{U_\infty} \tag{2.24}$$

which introduced in (2.20) gives

$$\eta F_1' = const = \frac{1}{\kappa} \tag{2.25}$$

$$\Rightarrow \quad F_1 = \frac{1}{\kappa} \ln \eta - B_1 \tag{2.26}$$

or equivalently

$$\frac{U_\infty - \overline{U}}{u_\tau} = -\frac{1}{\kappa} \ln \eta + B_1. \tag{2.27}$$

The log-law (2.22) together with the matching of the shear stress is indeed compatible with the integrated form of the boundary layer equation in 'inner similarity form', *i.e.* eq.(2.15), as $y^+ \to \infty$ ($g \to 1$ as $y^+ \to \infty$).

2.5. Similarity description of the outer layer

From the above analysis we get the outer layer description (with $\varepsilon_n = \varepsilon_1^n$) as

$$\frac{\overline{U}}{U_\infty} = 1 + \gamma F_1(\eta) + \gamma^2 F_2(\eta) + \mathcal{O}(\gamma^3), \tag{2.28}$$

where

$$\gamma = \frac{u_\tau}{U_\infty}. \tag{2.29}$$

Integrating the expression (2.28) from $\eta = 0$ to infinity yields

$$\Delta = \frac{\delta_*}{\gamma} \left\{ -\frac{1}{\int_0^\infty F_1 d\eta} + \gamma \frac{\int_0^\infty F_2 d\eta}{\left(\int_0^\infty F_1 d\eta \right)^2} + O(\gamma^2) \right\} \tag{2.30}$$

where we have used the definition of the displacement thickness (and that $\eta = y/\Delta$). We can here choose the definition of Δ such that

$$\int_0^\infty F_1 d\eta = -1 \tag{2.31}$$

which hence gives that

$$\Delta = \frac{\delta_*}{\gamma} \left\{ 1 + \gamma \int_0^\infty F_2 d\eta + O(\gamma^2) \right\}. \tag{2.32}$$

To leading order this is the Clauser-Rotta lengthscale (Rotta 1950; Clauser 1956).

We wish to reformulate the boundary layer equation in similarity form by use of the expression (2.28) and the definition of Δ (eq. 2.32). For this purpose we need to estimate du_τ/dx and $d\Delta/dx$. By combining (2.22) with (2.28,2.26) we obtain the logarithmic friction law

$$\frac{U_\infty}{u_\tau} = \frac{1}{\kappa} \ln \frac{\Delta u_\tau}{\nu} + B + B_1, \tag{2.33}$$

from which we readily derive

$$\frac{\Delta}{u_\tau} \frac{du_\tau}{dx} \Big/ \frac{d\Delta}{dx} = \mathcal{O}\left(\gamma\right). \tag{2.34}$$

In estimating $d\Delta/dx$ we first remember that for a zero pressure-gradient turbulent boundary layer we have

$$\frac{d\theta}{dx} = \left(\frac{u_\tau}{U_\infty}\right)^2 = \gamma^2 \tag{2.35}$$

where θ is the momentum loss thickness

$$\theta = \int_0^\infty \frac{\overline{U}}{U_\infty} \left(1 - \frac{\overline{U}}{U_\infty}\right) dy \tag{2.36}$$

which by use of (2.28) and (2.32) can be expressed as

$$\frac{\theta}{\delta_*} = 1 - \gamma \int_0^\infty F_1^2 d\eta + \mathcal{O}(\gamma^2) \tag{2.37}$$

Hence the contributions from F_2 vanish to order γ in this expression and we note that the shape factor $H_{12} = \delta_*/\theta$ can be expressed as

$$H_{12} = \left[1 - \gamma \int_0^\infty F_1^2 d\eta\right]^{-1} + \mathcal{O}(\gamma^2) \tag{2.38}$$

i.e. the shape factor will approach unity (from above) as the Reynolds number tends to infinity ($u_\tau/U_\infty \to 0$). The relation (2.38) is also consistent with the variation found for the shape factor (see figure 17 of paper 7). From (2.37) we obtain by use of (2.34), (2.35)

$$\frac{d\delta_*}{dx} = \frac{d\theta}{dx} \left(1 + \mathcal{O}(\gamma)\right) = \gamma^2 + \mathcal{O}\left(\gamma^3\right), \tag{2.39}$$

$$\frac{d\Delta}{dx} = \frac{1}{\gamma} \frac{d\delta_*}{dx} \left(1 + \mathcal{O}(\gamma)\right) = \gamma + \mathcal{O}\left(\gamma^2\right). \tag{2.40}$$

For the reformulation of the boundary layer equation we need

$$\frac{\partial \eta}{\partial x} = -\frac{\eta}{\Delta} \frac{d\Delta}{dx} = -\frac{\eta}{\delta_*} \left(\gamma^2 + \mathcal{O}\left(\gamma^3\right)\right), \tag{2.41}$$

$$\frac{\partial \eta}{\partial y} = \frac{1}{\Delta} = \frac{1}{\delta_*} \left(\gamma + \mathcal{O}\left(\gamma^2\right)\right). \tag{2.42}$$

Introduction of (2.28) into the boundary layer equation (2.8), where the viscous term may be neglected, and by use of (2.34), (2.41), (2.42) and the continuity equation we get the leading order balance

$$-\eta F_1' = G_0'. \tag{2.43}$$

The similarity formulation to leading order of the boundary layer equation, *i.e.* (2.43) can easily be seen to be consistent with the overlap matching results. As $\eta \to 0$ we can expand G_0 as

$$G_0 = C_0 + C_1 \eta + \mathcal{O}(\eta^2). \tag{2.44}$$

The matching for the Reynolds shear stress gives in combination with equation (2.15) (since $f' \to 0$ as $y^+ \to \infty$) that $g \to 1$ as $y^+ \to \infty$ and hence that $G_0 \to 1$ as $\eta \to 0$. Hence, the constant C_0 is determined to 1. For the first order correction for the beginning of the outer region we further get, from equation (2.43), (since $F_1' = 1/(\kappa\eta)$) that $C_1 = -1/\kappa$.

To summarize the above analysis for the outer region we conclude that to leading order the governing lengthscale is

$$\Delta = \delta_* \frac{U_\infty}{u_\tau} \tag{2.45}$$

and the normalized wall distance is

$$\eta = \frac{y}{\delta_*} \frac{u_\tau}{U_\infty}. \tag{2.46}$$

The velocity distribution can now be written as a defect law

$$\frac{U_\infty - \overline{U}}{u_\tau} = -F_1(\eta) + \mathcal{O}(\gamma), \tag{2.47}$$

where, in the overlap region, F_1 is given by (2.26).

It is interesting to note that the logarithmic friction law takes the form (2.33) which also can be written as

$$\frac{U_\infty}{u_\tau} = \frac{1}{\kappa} \ln \frac{\delta_* U_\infty}{\nu} + B + B_1 \tag{2.48}$$

which hence is an explicit relation between U_∞/u_τ and the Reynolds number, Re_{δ_*}, for which it also can be written as

$$c_f = 2 \left[\frac{1}{\kappa} \ln Re_{\delta_*} + B + B_1 \right]^{-2} \tag{2.49}$$

In the following papers an alternative form with Re_θ instead of Re_{δ_*} will be used, partly to enable comparisons with existing proposals in the literature.

Experiments

3.1. History

Historically, knowledge of the structure of turbulent boundary layers was gained experimentally from wind-tunnel measurements. Among the early measurements are those carried out by Schultz-Grunow (1940), Ludwieg & Tillman (1950), Klebanoff (1955) and Smith & Walker (1959). For an extensive survey of the empirical knowledge of the early data the reader is referred to Coles (1962) classical paper. In the survey by Fernholz & Finley (1996) more recent experiments can be found.

Modern computers have recently become fast enough to perform direct numerical simulations of the Navier-Stokes equations for fully turbulent flows, although only at low Reynolds number and in simple geometries, see *e.g.* the landmark papers by Kim *et al.* (1987) and Spalart (1988). The first simulation of a turbulent boundary layer was made by the latter, at Re_θ up to 1410. Since then several boundary layer simulations have been made, also at different of pressure gradients, see *e.g.* Skote *et al.* (1998).

From the large number of experiments performed during the years several important conclusions can be drawn. First, it is of primary importance to make very accurate and preferably independent measurements of the wall-shear stress. Secondly, at high Reynolds number the distance from the probe to the wall has to be determined with extremely high accuracy (because of the small viscous length scale). These two goals seem obvious, but was fulfilled only in a few experiments. In the present experimental set-up a large effort was made to fulfill these conditions.

3.2. Experimental set-up

The flow field of a zero pressure-gradient turbulent boundary layer was established on a seven meter long flat plate mounted in the test section of the MTL wind-tunnel at KTH. The MTL wind tunnel is of closed-return type designed with low disturbance level as the primary design goal. A brief description of the experimental set-up is given below. A more detailed description of the boundary layer experimental set-up can be found in paper 7. After the test section the flow passes through diffusers and two 90° turns before the fan. A large fraction of the wind-tunnel return circuit is equipped with noise-absorbing
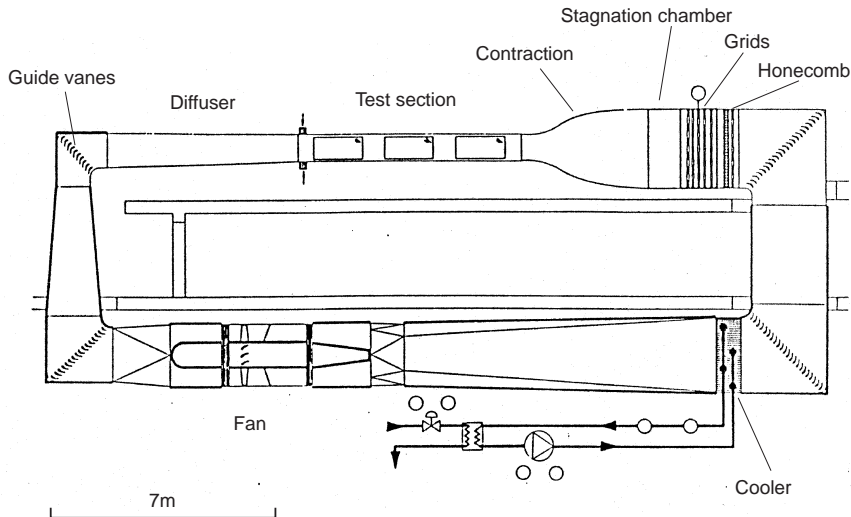
FIGURE 3.1. Schematic of the MTL wind tunnel facility at KTH

walls to reduce acoustic noise. The high flow quality of the MTL wind-tunnel was reported by Johansson (1992). For instance, the streamwise turbulence intensity was found to be less than 0.02%. The air temperature can be controlled within ±0.05 °C, which was very important for this study since the primary measurement technique was hot-wire/hot-film anemometry, where a constant air temperature during the measurement is a key issue. The test section has a cross sectional area of 0.8 m (high) × 1.2 m (wide) and is 7 m long. The upper and lower walls of the test section can be moved to adjust the pressure distribution. The maximum variation in mean velocity distribution along the boundary layer plate was ±0.15%.

The plate is a sandwich construction of aluminum sheet metal and square tubes in seven sections plus one flap and one nose part, with the dimensions 1.2 m wide and 7 m long excluding the flap. The flap is 1.5 m long and is mounted in the first diffuser. This arrangement makes it possible to use the first 5.5 m of the plate for the experiment. One of the plate sections was equipped with two circular inserts, one for a plexiglas plug where the measurements were carried out, and one for the traversing system. The traversing system was fixed to the plate to minimize vibrations and possible deflections. The distance to the wall from the probe was determined by a high magnification microscope. The absolute error in the determination of the wall distance was within ±5μm.

The boundary layer was tripped at the beginning of the plate and the two-dimensionality of the boundary layer was checked by measuring the spanwise

variation of the wall shear stress τ_w. The maximum spanwise variation in friction velocity $u_\tau = \sqrt{\tau_w/\rho}$ was found to be less than $\pm 0.7\%$.

The ambient conditions were monitored by the measurement computer during the experiments using an electronic barometer and thermometer (FCO 510 from Furness Ltd., UK). The reference conditions used in the calibration of the probes were determined using a Prandtl tube in the free-stream directly above the measurement station. The pressure and temperature were monitored at all times during the experiments using a differential pressure transducer and a thermometer connected directly to the measurement computer. The accuracy of the pressure measurement was 0.25 % and the accuracy of the temperature measurement was 0.02 °C.

Constant temperature hot-wire anemometry was used in all velocity measurements. All hot-wire probes were designed and built at the lab. Three sizes of single-wire probes were used in the experiments with wire diameters of: 2.5, 1.27 and 0.63 μm and a length to diameter ratio always larger than 200.

The MEMS hot-film used in the wall-shear stress measurements was designed by the MEMS group at UCLA/Caltec (Jiang *et al.* 1996, 1997; Ho & Tai 1998). It was flush-mounted with a printed circuit board for electrical connections which in turn was flush-mounted into a Plexiglas plug fitting into the instrumentation insert of the measurement plate-section. Accurate alignment of the chip surface and the circuit board and the flat plate was achieved using a microscope during the mounting of the sensor set-up. The MEMS sensor chip has four rows of 25 sensors each with a spanwise separation of 300 μm, see figure 3.7. The length of the hot-film is 150μm and the width 3μm. It is placed on a 1.2μm thick silicon-nitride diaphragm with dimensions 200μm $\times$ 200μm. Thermal insulation of the hot-film to the substrate is provided by a 2μm deep vacuum cavity underneath the diaphragm.

The anemometer system (AN1003 from AA lab systems, Israel) had a built-in signal conditioner and the signals from the anemometer were digitized using an A/D converter board (A2000 from National Instruments, USA) in the measurement computer. The A/D converter has 12 bit resolution and four channels which could be sampled simultaneously at rates up to 1 MHz divided by the number of channels used. The complete experiment was run from a program on the measurement computer which controlled the tunnel velocity, the positioning of probes, digitization of the anemometer signals, monitoring of the pressures and the temperature.

3.3. Results

Different sets of experiments were run with the set-up described in section 3.2 and are summarized in table 1. Single-wire measurements (SW) were carried out at 5 different streamwise positions $x = \{1.5, 2.5, 3.5, 4.5, 5.5\}$ at 10 different mean velocity settings ranging from 10 to 55 m/s. At the position $x = 5.5$ m

	Re_θ	Quantity	Pos. (x)	Ref.
SW	2500–27300	U	1.5–5.5	paper 1 & 2
XW	6900–22500	U, V	5.5	paper 3
VW	6900–22500	U, W	5.5	paper 3
MEMS-WW	9700	τ_w	5.5	paper 4
MEMS-MEMS	9700	$\tau_w, \tau_w(\Delta z)$	5.5	paper 6
MEMS-SW 1	9700	$\tau_w, U(\Delta x, \Delta y)$	5.5	paper 6
MEMS-SW 2	9700	$\tau_w, U(\Delta y, \Delta z)$	5.5	paper 6

TABLE 1. Overview of the different sets of experiments.

experiments with three different probe sizes were also conducted. An X-probe was used at the position $x = 5.5$ m for measurements (XW) of the simultaneous streamwise U and wall-normal velocity V components. The simultaneous streamwise and spanwise W velocity components were measured (VW) using a V-probe. The MEMS hot-film sensor, with 25 individual hot-films distributed in the spanwise direction, was utilized to measure the simultaneous skin-friction in two points at different spanwise separations. The MEMS hot-film sensor was also used to measure simultaneously the skin-friction and the streamwise velocity separated in either the x-y plane (MEMS-SW 1) or separated in the y-z plane (MEMS-SW 2).

The mean skin friction was determined using oil-film interferometry and the near-wall method. The result is shown in figure 3.2. A fit to c_f by a variant of the logarithmic skin friction law, namely

$$c_f = 2 \left[\frac{1}{\kappa} \ln(Re_\theta) + C \right]^{-2}, \tag{3.50}$$

was made for each of the data sets. The value of the von Kármán constant determined in this way was $\kappa = 0.384$ and the additive constant was found to be $C = 4.08$, see paper 2. The resulting logarithmic skin-friction laws agree very well with each other and also with the correlation by Fernholz & Finley (1996).

The large set of single-wire measurements gave a unique possibility to investigate topics such as the mean velocity scaling laws. In figures 3.3 and 3.4 the mean velocity profiles from single-wire measurements in the Reynolds number range $2500 < Re_\theta < 27700$ are shown in inner and outer scaling. Also shown in the figures are the logarithmic laws with the newly determined values of the log-law constants $\kappa = 0.38$, $B = 4.1$ and $B_1 = 3.6$ (paper 1).

The scaling law in the overlap region was investigated using the normalized slope of the mean velocity profile,

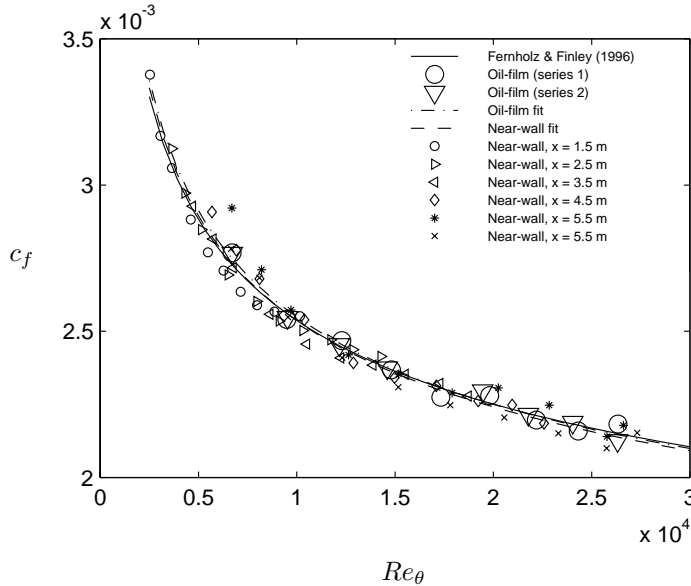$$\Xi = \left(y^+ \frac{d\overline{U}^+}{dy^+} \right)^{-1}. \tag{3.51}$$

FIGURE 3.2. Skin-friction coefficient c_f using the oil-film and near wall methods (paper 7), shown with best-fit logarithmic friction laws from equation 3.50 and the correlation by Fernholz & Finley (1996).

In a logarithmic region of the profiles Ξ is constant and equal to κ. The value of Ξ was calculated by taking an average of the individual profiles at a constant wall distance in inner scaling while omitting the part of the profiles where $\eta > M_o$. Similarly, the profiles were again averaged at constant outer-scaled distances from the wall for $y^+ > M_i$. The parameters M_i and M_o are the inner and outer limits of the overlap region. In Figure 3.5, the averaged Ξ is shown together with error bars representing a 95% confidence interval. A region where a nearly constant Ξ very accurately represents the data is evident in both figures. This clearly supports the existence of a logarithmic overlap region within the appropriate range of the parameters M_i and M_o. The choice of the appropriate limits was subsequently selected based on the y values where the error bar deviates significantly from the horizontal line in the figures. This was based on an iteration of the limits until a consistent result was obtained. The resulting values for the inner and outer limits are $M_i \approx 200$ and $M_o \approx 0.15$, respectively.

Statistical quantities, such as the turbulence intensities, were investigated in paper 3. The peak values of the absolute and relative intensities are shown in figure 3.6. Also shown in figure 3.6 are corresponding values obtained from direct numerical simulations by Spalart (1988), Moser *et al.* (1999) and Alvelius
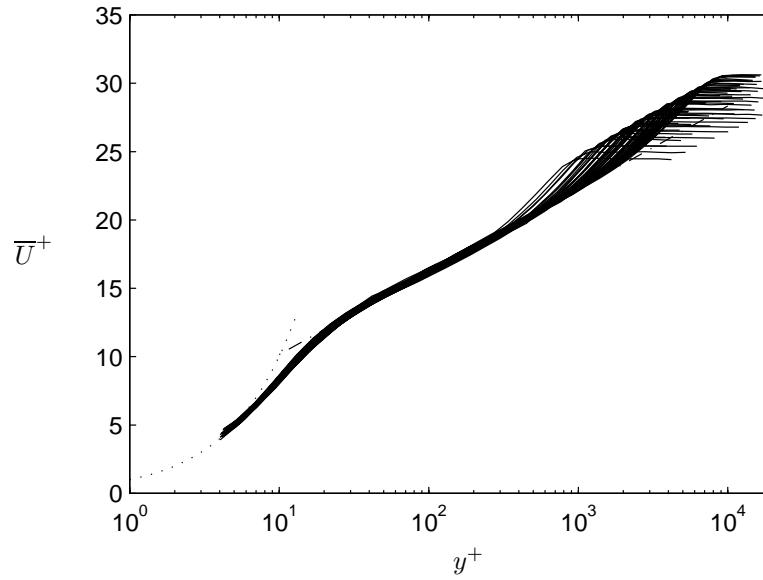
FIGURE 3.3. Profiles of the mean velocity in inner-law scaling. $2530 < Re_\theta < 27300$. Dash-dotted line: $\frac{1}{0.38} \ln y^+ + 4.1$.
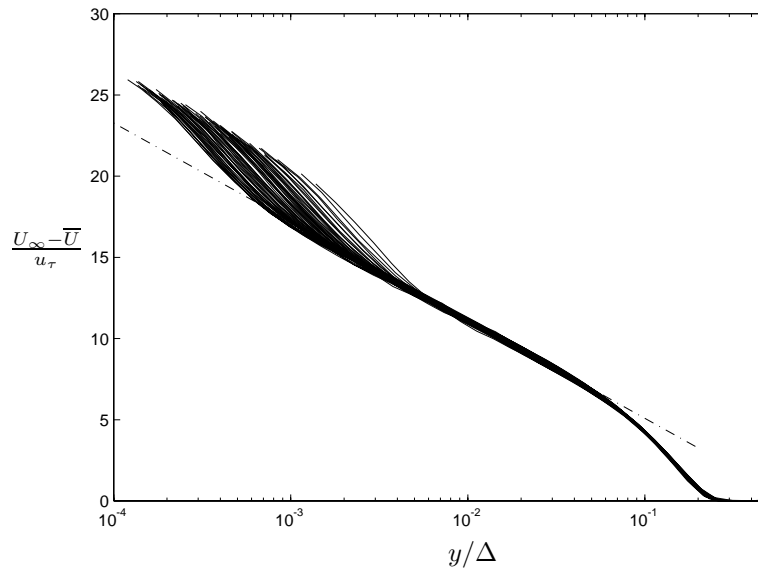

FIGURE 3.4. Profiles of the mean velocity in outer-law scaling. Log-law constants $\kappa = 0.38$ and $B_1^\Delta = 1.62$. $2530 < Re_\theta < 27300$
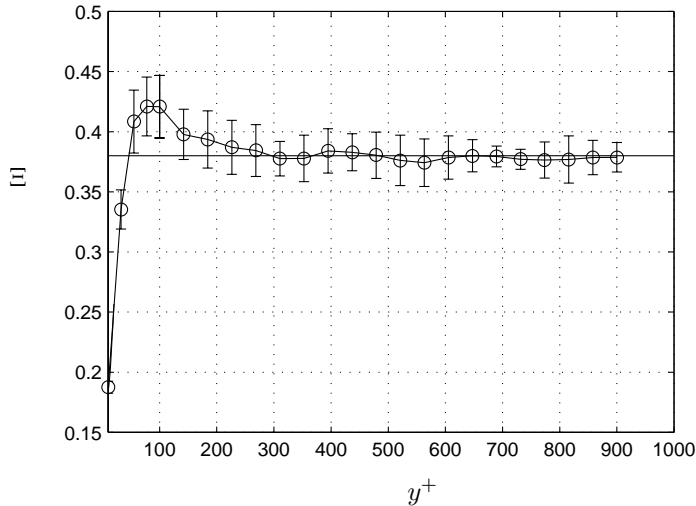
FIGURE 3.5. Normalized slope of mean profile, Ξ, shown in inner scaling; only the part of the profiles in which $\eta < 0.15$ was used and the horizontal line corresponds to $\kappa = 0.38$

(1999), where the first is a boundary layer simulation and the last two are channel flow simulations. One should keep in mind in the comparisons with the DNS-data that the channel flow has a somewhat different character, where Reynolds number effects on turbulence production etc. can be related to the relative influence of the pressure gradient. This can partly be seen from the integrated form of the mean flow equation. An increasing trend is visible in figure 3.6. The increase in $\sqrt{\overline{u^2}}/u_\tau$ is about 7% for the present data in this Reynolds number range but the increase in $\sqrt{\overline{u^2}}/\overline{U}$ is only about half of that. For $\sqrt{\overline{u^2}}/u_\tau$ one can observe a significant difference between the channel flow and boundary layer DNS data. The present set of experimental data smoothly extends the boundary layer DNS-results to substantially higher Reynolds numbers, with a continued increase of the maximum intensity. One could expect a levelling off to occur at high Reynolds numbers. From the results in figure 3.6 it is not really possible to determine an asymptotic level of $(\sqrt{\overline{u^2}}/u_\tau)_{\mathrm{max}}$ but it can be judged to be at least 2.9. The peak value of $\overline{v^2}$ is seen in figure 3.6 to increase with the Reynolds number in a manner similar to the variation in the peak value for $\overline{u^2}$. At the high Reynolds number end a decreasing trend is seen that is probably due to spatial averaging effects. The increase in $(\overline{v^2}/u_\tau)_{\mathrm{max}}$ for $Re_\theta < 13000$ seems consistent with the low Reynolds number DNS-results. Fernholz & Finley (1996) reported max-values of about 1.4 for $Re_\theta = 20920$
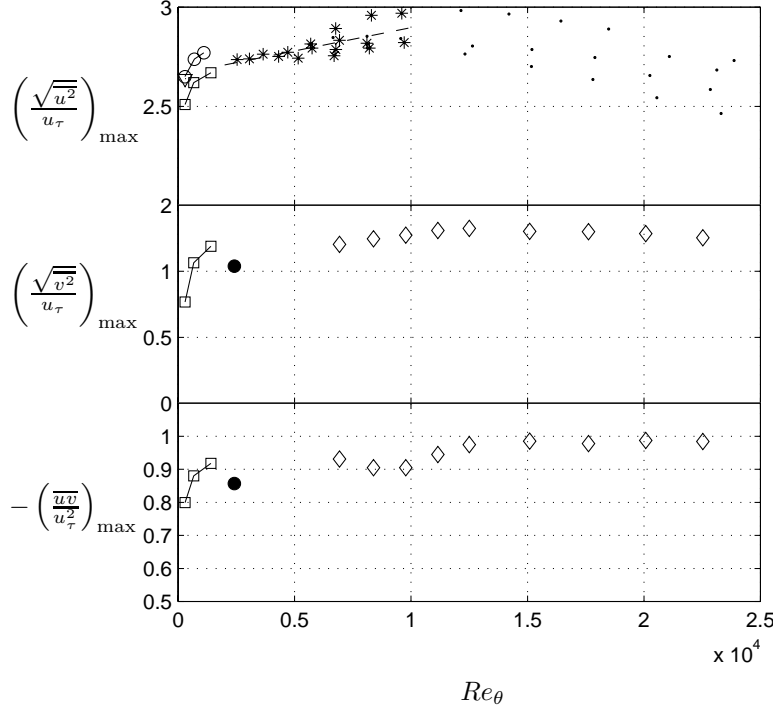
FIGURE 3.6. Maximum streamwise turbulence intensity ($x = 5.5$m). $*$: Present experiment, $6.5 < L^+ < 10$. Dashed line: linear regression to the present experiment. ($\cdot$): Present experiment, $L^+ > 10$ (spread is partially due to use of three different probe sizes). $\diamond$: X-probe data. $\circ$: DNS of channel flow by Moser *et al.* (1999). $\square$: DNS of zero pressure gradient boundary layer by Spalart (1988). ∇: DNS of channel flow by Alvelius (1999). $\bullet$: LDV results from boundary layer flow at $Re_\theta = 2420$ by Karlsson & Johansson (1988).

obtained with a probe size of about 26 in wall-units. This is in reasonable agreement with the results in figure 3.6.

The Reynolds number variation of the shear-stress peak value is shown in figure 3.6. The peak values show an increasing trend with Reynolds number that flattens out very close to unity for Reynolds numbers above about 15000. The increasing trend at low Reynolds numbers also here seems consistent with the DNS-results.

Miniaturized wall-hot-wires and a MEMS hot-film were used to measure the fluctuating wall-shear stress (reported in paper 4). In figure 3.8 results
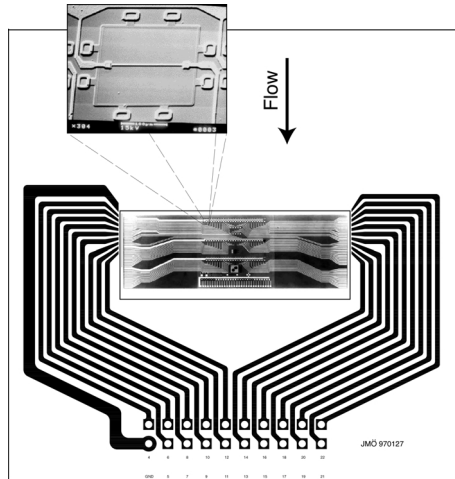
FIGURE 3.7. MEMS hot-film sensor chip from UCLA/Caltech (Jiang *et al.* 1996), mounted in the center of a printed circuit board providing the electrical connections. A blow-up of one of the vacuum insulated hot-films is also shown.

for the skin-friction intensity T_{τ_w} are presented, for all experiments performed in this investigation, against the active sensor length in viscous units. The data show a decrease in intensity for increasing probe dimensions as a result of spatial averaging (see *e.g.* Johansson & Alfredsson 1983; Ligrani & Bradshaw 1987). The limiting value of the turbulence intensity for small probe lengths is here found to be about 0.41. For comparison the results from the wall-hot-wire experiments at MIT in a turbulent boundary layer in air flow by Alfredsson *et al.* (1988) are also shown in figure 3.8 and show good agreement with the present data. The resulting intensity from the MEMS hot-film of 0.35 is more than 10% too low and can probably be attributed to remaining heat losses in the diaphragm that modifies the dynamic response compared to the static one. Still, the result represents a major improvement compared to previous findings using hot-films in air where values of about 0.1 are reported for the relative intensity of the wall shear stress fluctuations. Also, the rapid development in MEMS technology will probably lead towards large improvements in the near future. The wall-hot-wire of type 3, with the wire welded onto prongs flush with the wall, show a behavior similar to the hot-film. The plausible explanation being that heat flux from the wire, which is only a few μm above the wall, is partly absorbed by the wall and transferred back to the fluid, in a mechanism similar to that for the hot-film. A connected issue is that the sensitivity of
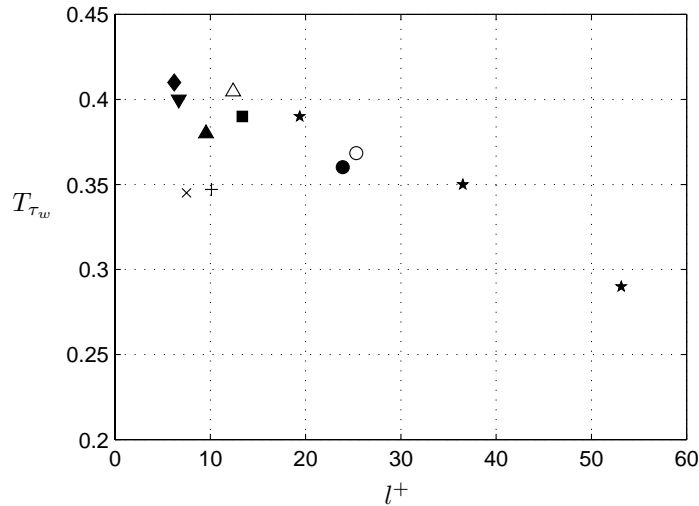
FIGURE 3.8. Turbulent skin friction intensity T_{τ_w}. Present experiments, ∘: WW1, MTL, +: WW3, MTL, ×: MHF, MTL, △: WW2, MTL, •: WW1, LaWiKa, ▲: WW2, LaWiKa, ■: WW2, LaWiKa, ◆: WW2, LaWiKa, ▼: WW2, LaWiKa (for details see table 2 in paper 4). ⋆: experiment by Alfredsson *et al.* (1988).

type 3 wall-hot-wires is very low due to damping resulting from the proximity of the wall.

Kline *et al.* (1967), showed that a significant part of the turbulence could be described in terms of deterministic events, and that in the close proximity of the wall the flow is characterized by elongated regions of low and high speed fluid of fairly regular spanwise spacing of about $\lambda^+ = 100$. Sequences of ordered motion occur randomly in space and time where the low-speed streaks begin to oscillate and to suddenly break-up into a violent motion, a "burst". Kim *et al.* (1971) showed that the intermittent bursting process is closely related to shear-layer like flow structures in the buffer region. To obtain quantitative data to describe the structures a reliable method to identify bursts with velocity or wall-shear stress measurements is needed. Kovasznay *et al.* (1970) were the first to employ conditional averaging, using a trigger, to study individual events such as bursts or ejections. The triggering signal must be intermittent and closely associated with the event under study. Wallace *et al.* (1972) and Willmart & Lu (1972) introduced the uv quadrant splitting scheme. Blackwelder & Kaplan (1976) developed the VITA technique to form a localized measure of
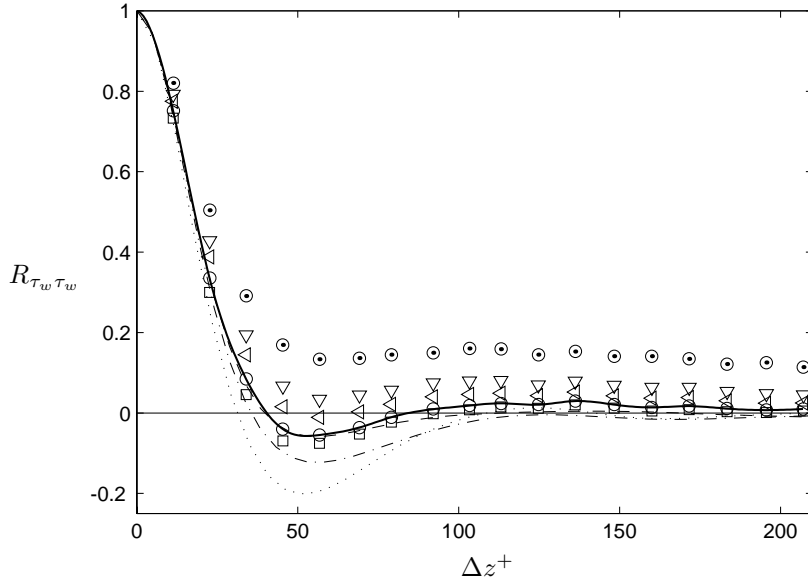
FIGURE 3.9. Spanwise correlation coefficient $R_{\tau_w \tau_w}$ as a function of Δz^+, $Re_\theta = 9500$. Present data, $\odot$: unfiltered, $\triangledown$: $f_c^+ = 1.3 \times 10^{-3}$, $\triangleleft$: $f_c^+ = 2.6 \times 10^{-3}$, $\circ$: $f_c^+ = 5.3 \times 10^{-3}$, $\square$: $f_c^+ = 7.9 \times 10^{-3}$, —: spline fit to $\circ$. DNS of channel flow, $--$: $Re_\tau = 590$, $-\cdot-$: $Re_\tau = 385$, $\cdots$: $Re_\tau = 180$ (Kim *et al.* 1987; Moser *et al.* 1999).

the turbulent kinetic energy and used it to detect shear-layer events. For a comprehensive overview of the literature in the field of coherent structures the reader is referred to the review article by Robinson (1991).

In paper 6 the mean spanwise separation between low-speed streaks in the viscous sub-layer was investigated using a MEMS array of hot-films. The spanwise cross correlation coefficient between the wall-shear stress signals

$$R_{\tau_w \tau_w}(\Delta z) = \frac{\overline{\tau_w(z)\tau_w(z + \Delta z)}}{\tau_w'^2}, \tag{3.52}$$

obtained from two hot-films separated a distance Δz^+ in the spanwise direction was used to estimate the mean streak spacing. At high Reynolds numbers contributions to the spanwise correlation coefficient from low frequency structures originating in the outer region conceals the contributions from the streaks and no clear (negative) minimum is visible in figure 3.9 for the measured correlation coefficient (shown as $\odot$). This behavior was found also by others, see *e.g.* Gupta *et al.* (1971). A trend is clearly visible in the relatively low Reynolds number

simulations by Kim *et al.* (1987) and Moser *et al.* (1999) where at their high Reynolds number the minimum is less pronounced. In an attempt to reveal and possibly obtain the streak spacing also from the high Reynolds number data in the present experiment we applied a high-pass (Chebyshev phase-preserving) digital filter to the wall-shear stress signals before calculating the correlation coefficient. This procedure reveals the content from the streaks and enhances the variation in the correlation coefficient. A variation of the cut-off frequency revealed no significant dependence of the position of the minimum on the cut-off. The cut-off frequency was chosen to damp out frequencies coming from structures larger than about 2500 viscous length scales corresponding to the boundary layer thickness. The filtered correlation is shown for different cut-off frequencies in figure 3.9. The correlation decrease rapidly and a broad minimum is found at $\Delta z^+ \approx 55$ giving a mean streak spacing of $\lambda^+ \approx 110$. The correlation coefficient is close to zero for separations $\Delta z^+ > 100$.

CHAPTER 4

Concluding Remarks

Experimental results were presented for turbulent boundary layer measurements spanning over one decade in Reynolds number, $2500 < Re_\theta < 27000$.

The classical two layer theory was confirmed and constant values of the slope of the logarithmic overlap region (*i.e.* von Kármáns constant) and the additive constants were found and estimated to $\kappa = 0.38$, $B = 4.1$ and $B_1 = 3.6$ ($\delta = \delta_{95}$). The inner limit of overlap region was found to scale on the viscous length scale (ν/u_τ) and was estimated to be $y^+ = 200$, *i.e.* considerably further out compared to previous knowledge. The outer limit of the overlap region was found to scale on the outer length scale and was estimated to be $y/\delta = 0.15$. This means that a universal overlap region can only be expected for Reynolds numbers larger than $Re_\theta \approx 6000$. The newly determined limits also explain the Reynolds number variation found in some earlier experiments.

Measurements of the fluctuating wall-shear stress using the hot-wire-on-the-wall technique and a MEMS hot-film sensor show that the turbulence intensity $\tau_w/\tau_{\text{r.m.s.}}$ is close to 0.41 at $Re_\theta \approx 9800$. This was also substantiated by near-wall single-wire measurements.

A numerical and experimental investigation of the behavior of double wire probes were carried out and showed that the Péclet number based on wire separation should be larger than about 50 to keep the interaction at an acceptable level.

Results are presented for two-point correlations between the wall-shear stress and the streamwise velocity component for separations in both the wall-normal-streamwise plane and the wall-normal-spanwise plane. Results are presented for the streak spacing and the propagation velocity of near wall shear layer events. Turbulence producing events are further investigated using conditional averaging of isolated events detected using the VITA technique. Comparisons are made with results from other experiments and numerical simulations.

Acknowledgments

I would like to sincerely thank my supervisor Prof. Arne Johansson for accepting me as his student, imparting his knowledge and and guiding me through the maze of turbulence research. Arne has read and and given constructive criticism an all manuscripts in this work.

I also would like to thank Prof. Henrik Alfredsson for innumerable helpful discussions about fluid mechanics and especially turbulence experiments.

My thanks to Prof. Hassan Nagib at IIT, with whom I had the great pleasure to work with during his stay at KTH. The enthusiastic and creative comments from Hassan has been invaluable when finishing this work.

I also wish to thank Dr. Erik Lindborg for clarifying discussions on the analysis of the boundary layer similarity analysis.

My special thanks go to my dear friend and former colleague Alexander Sahlin together with who I started out doing the experiments leading to this thesis. Alexander's sound knowledge of fluid dynamics has been invaluable help throughout this work.

Many thanks go to the faculty, my colleagues and fellow students at the Department of Mechanics for a pleasant, stimulating and inspiring atmosphere. Especially I want to thank my friends and room mates Torbjörn Sjögren and Björn Lindgren who have made my time in the lab most enjoyable.

I wish to thank Marcus Gällstedt and Ulf Landén for help with designing and building many of the experiments and for skillful assistance in the laboratory.

Last but not the least, I want to thank my parents and family for their support and especially, Ulrika for your love.

References

ALFREDSSON, P. H., JOHANSSON, A. V., HARITONIDIS, J. H. & ECKELMANN, H. 1988 The fluctuation wall-shear stress and the velocity field in the viscous sublayer. *Phys. Fluids A* **31**, 1026–33.

ALVELIUS, K. 1999 Studies of turbulence and its modeling through large eddy- and direct numerical simulation. PhD thesis, Department of Mechanics, Royal Institute of Technology, Stockholm.

BARENBLATT, G. I. 1993 Scaling laws for fully developed turbulent shear flows. part 1. basic hypotheses and analysis. *J. Fluid Mech.* **248**, 513–520.

BARENBLATT, G. I. & CHORIN, A. J. 1999 Self-similar intermediate structures in turbulent boundary layers at large reynolds numbers. PAM 755. Center for Pure and Applied Mathematics, University of California at Berkeley.

BARENBLATT, G. I. & PROSTOKISHIN, V. M. 1993 Scaling laws for fully developed turbulent shear flows. part 2. processing of experimental data. *J. Fluid Mech.* **248**, 521–529.

BLACKWELDER, R. F. & KAPLAN, R. E. 1976 On the wall structure of the turbulent boundary layer. *J. Fluid Mech.* **76**, 89–112.

CLAUSER, F. H. 1956 The turbulent boundary layer. *Advances Appl. Mech.* **4**, 1–51.

COLES, D. E. 1956 The law of the wake in the turbulent boundary layer. *J. Fluid Mech.* **1**, 191–226.

COLES, D. E. 1962 The turbulent boundary layer in a compressible fluid. R 403-PR. The RAND Corporation, Santa Monica, CA.

FERNHOLZ, H. H. & FINLEY, P. J. 1996 The incompressible zero-pressure-gradient turbulent boundary layer: An assessment of the data. *Prog. Aerospace Sci.* **32**, 245–311.

GEORGE, W. K., CASTILIO, L. & WOSNIK, M. 1997 Zero-pressure-gradient turbulent boundary layer. *Applied Mech. Reviews* **50**, 689–729.

GUPTA, A. K., LAUFER, J. & KAPLAN, R. E. 1971 Spatial structure in the viscous sublayer. *J. Fluid Mech.* **50**, 493–512.

HINCH, E. J. 1991 *Perturbation methods*. Cambridge University Press.

HINZE, J. O. 1975 *Turbulence*, 2nd edn. McGraw-Hill.

HO, C.-M. & TAI, Y.-C. 1998 Micro-electro-mechanical-systems (MEMS) and fluid flows. *Ann. Rev. Fluid Mech.* **30**, 579–612.

Jiang, F., Tai, Y.-C., Gupta, B., Goodman, R., Tung, S., Huang, J. B. & Ho, C.-M. 1996 A surface-micromachined shear stress imager. In *1996 IEEE Micro Electro Mechanical Systems Workshop (MEMS '96)*, pp. 110–115.

Jiang, F., Tai, Y.-C., Walsh, K., Tsao, T., Lee, G. B. & Ho, C.-H. 1997 A flexible mems technology and its first application to shear stress sensor skin. In *1997 IEEE Micro Electro Mechanical Systems Workshop (MEMS '97)*, pp. 465–470.

Johansson, A. V. 1992 A low speed wind-tunnel with extreme flow quality - design and tests. In *Prog. ICAS congress 1992*, pp. 1603–1611. ICAS-92-3.8.1.

Johansson, A. V. & Alfredsson, P. H. 1983 Effects of imperfect spatial resolution on measurements of wall-bounded turbulent shear flows. *J. Fluid Mech.* **137**, 409–421.

Karlsson, R. I. & Johansson, T. G. 1988 Ldv measurements of higher order moments of velocity fluctuations in a turbulent boundary layer. In *Laser Anemometry in Fluid Mechanics*. Ladoan-Instituto Superior Técnico, 1096 L.C., Portugal.

von Kármán, T. 1921 Ueber laminare un turbulente Reibung. *Z. angew. Math. Mech.* pp. 233–252, NACA TM 1092.

von Kármán, T. 1930 Mechanische Aehnlichkeit und Turbulenz. *Nachr. Ges. Wiss. Göttingen, Math. Phys. Kl.* pp. 58–68, NACA TM 611.

Kim, H. T., Kline, S. J. & Reynolds, W. C. 1971 The production of turbulence near a smooth wall in a turbulent boundary layer. *J. Fluid Mech.* **50**, 133–160.

Kim, J., Moin, P. & Moser, R. 1987 Turbulence statistics in fully developed channel flow. *J. Fluid Mech.* **177**, 133–166.

Klebanoff, P. S. 1955 Characteristics of turbulence in a boundary layer with zero pressure gradient. TR 1247. NACA.

Kline, S. J., Reynolds, W. C., Schraub, F. A. & Runstadler, P. W. 1967 The structure of turbulent boundary layers. *J. Fluid Mech.* **30**, 741.

Kovasznay, L. G., Kibens, V. & Blackwelder, R. S. 1970 Large-scale motion in the intermittent region of a turbulent boundary layer. *J. Fluid Mech.* **41**, 283–325.

Landahl, M. T. & Mollo-Christensen, E. 1987 *Turbulence and Random Processes in Fluid Mechanics*. Cambridge University Press.

Ligrani, P. M. & Bradshaw, P. 1987 Spatial resolution and measurement of turbulence in the viscous sublayer using subminiature hot-wire probes. *Experiments in Fluids* **5**, 407–417.

Ludwieg, H. & Tillman, W. 1950 Investigations of the wall shearing stress in turbulent boundary layers. TM 1285. NACA.

Millikan, C. B. 1938 A critical discussion of turbulent flows in channels and circular tubes. In *Proceedings of the Fifth International Congress of applied Mechanics*.

Moser, R. D., Kim, J. & Mansour, N. N. 1999 Direct numerical simulation of turbulent channel flow up to $Re_\theta = 590$. *Phys. Fluids* **11** (4), 943–945.

Prandtl, L. 1904 Ueber die Flüssigkeitsbewegung bei sehr kliner Ribung. In *Verhandlungen des III. Internationalen Mathematiker-Kongress, Heidelberg*, pp. 484–491.

PRANDTL, L. 1927 Ueber den Reibungswiderstand strömender Luft. *Ergebn. Aerodyn. Versuchsanst. Göttingen* **3**, 1–5.

PRANDTL, L. 1932 Zur turbulenten Strömung in Rohren und längs Platten. *Ergebn. Aerodyn. Versuchsanst. Göttingen* **4**, 18–29.

REYNOLDS, O. 1883 On the experimental investigation of the circumstances which determine whether the motion of water shall be direct or sinuous, and the law or resistance in parallel channels. *Phil. Trans. Roy. Soc. Lond.* **174**, 935–982.

REYNOLDS, O. 1895 On the dynamical theory of incompressible viscous fluids and the determination of the criterion. *Phil. Trans. Roy. Soc. A* **186**, 123–164.

ROBINSON, S. K. 1991 Coherent motions in the turbulent boundary layer. *Ann. Rev. Fluid Mech.* **23**, 601–639.

ROTTA, J. C. 1950 Über die Theorie der Turbulenten Grenzschichten. Mitt. M.P.I. Ström. Forschung Nr 1, also available as NACA TM 1344.

ROTTA, J. C. 1962 Turbulent boundary layers in incompressible flow. In *Progress in aeronautical sciences* (ed. A. Ferri, D. Küchemann & L. H. G. Sterne), , vol. 2, pp. 1–219. Pergamon press.

SCHLICHTING, H. 1979 *Boundary layer theory*. McGraw-Hill.

SCHULTZ-GRUNOW, F. 1940 Neues Reibungswiederstandsgesetz für glatte Platten. *Tech. Rep.* 8. Luftfahrtforschung, translated as *New frictional resistance law for smooth plates*, NACA TM-986, 1941.

SKOTE, M., HENKES, R. & HENNINGSON, D. 1998 Direct numerical simulation of self-similar turbulent boundary layers in adverse pressure gradients. In *Flow, Turbulence and Combustion*, , vol. 60, pp. 47–85. Kluwer Academic Publishers.

SMITH, D. W. & WALKER, J. H. 1959 Skin-friction measurements in incompressible flow. NASA TR R-26.

SPALART, P. R. 1988 Direct simulation of a turbulent boundary layer up to $Re_\theta = 1410$. *J. Fluid Mech.* **187**, 61–98.

TENNEKES, H. & LUMELY, J. L. 1972 *A first cource in turbulence*. The MIT press.

WALLACE, J. M., ECKELMANN, H. & BRODKEY, R. 1972 The wall region in turbulent shear flow. *J. Fluid Mech.* **54**, 39–48.

WILLMART, W. W. & LU, S. S. 1972 Structure of the Reynolds stress near the wall. *J. Fluid Mech.* **55**, 65–92.

ZAGAROLA, M. V., PERRY, A. E. & SMITS, A. J. 1997 Log laws or power laws: The scaling in the overlap region. *Phys. Fluids* **9** (7), 2094–100.

ZAGAROLA, M. V. & SMITS, A. J. 1998*a* Mean-flow scaling of turbulent pipe flow. *J. Fluid Mech.* **373**, 33–79.

ZAGAROLA, M. V. & SMITS, A. J. 1998*b* A new mean velocity scaling for turbulent boundary layers. In *Proceedings of FEDSM'98*.

Paper 1

A note on the overlap region in turbulent boundary layers

By Jens M. Österlund[1], Arne V. Johansson[1], Hassan M. Nagib[2] & Michael H. Hites[2]

[1]Dept. of Mechanics, KTH, SE-100 44 Stockholm, Sweden
[2]Illinois Institute of Technology, Chicago, IL 60616, USA

Two independent experimental investigations of the behavior of turbulent boundary layers with increasing Reynolds number were recently completed. The experiments were performed in two facilities, the MTL wind tunnel at KTH and the NDF wind tunnel at IIT. Both experiments utilized oil-film interferometry to obtain an independent measure of the wall-shear stress. A collaborative study by the principals of the two experiments, aimed at understanding the characteristics of the overlap region between the inner and outer parts of the boundary layer, has just been completed. The results are summarized here, utilizing the profiles of the mean velocity, for Reynolds numbers based on the momentum thickness ranging from 2,500 to 27,000. Contrary to the conclusions of some earlier publications, careful analysis of the data reveals no significant Reynolds number dependence for the parameters describing the overlap region using the classical logarithmic relation. However, the data analysis demonstrates that the viscous influence extends within the buffer region to $y^+ \approx 200$, compared to the previously assumed limit of $y^+ \approx 50$. Therefore, the lowest Re_θ value where a significant logarithmic overlap region exists is about 6,000. This probably explains why a Reynolds number dependence had been found from the data analysis of many previous experiments. The parameters of the logarithmic overlap region are found to be constant and are estimated to be: $\kappa = 0.38$, $B = 4.1$ and $B_1 = 3.6$ ($\delta = \delta_{95}$).

In the classical theory, the overall description of a turbulent boundary layer is dependent on two separate inner and outer length scales. The outer length scale is commonly taken as the thickness of the boundary layer δ, and the inner length scale as the viscous length $l^* = \nu/u_\tau$, where $u_\tau = \sqrt{\tau_w/\rho}$ is the friction velocity, τ_w is the skin friction and ρ is the density of the air. Dimensional analysis of the dynamic equations with boundary conditions leads to a scaling of the mean velocity profile in the inner and the outer parts of the boundary

layer in the form:

$$\overline{U}^+ = \frac{\overline{U}}{u_\tau} = f\left(y^+\right); \quad \overline{y}^+ = \frac{yu_\tau}{\nu} \tag{1}$$

$$\frac{U_\infty - \overline{U}}{u_\tau} = F\left(\eta\right); \quad \eta = \frac{y}{\delta} \tag{2}$$

At sufficiently large Reynolds numbers, it is assumed that there is a region of overlap, $\nu/u_\tau \ll y \ll \delta$, where the law of the wall (1) and the defect law (2) simultaneously hold. Matching (Millikan 1938) the relations (1) and (2) gives one of the classical results in turbulence theory, i.e., the logarithmic overlap region: in inner variables,

$$\overline{U}^+ = \frac{1}{\kappa} \ln\left(y^+\right) + B \tag{3}$$

and in outer variables

$$\frac{U_\infty - \overline{U}}{u_\tau} = -\frac{1}{\kappa} \ln\left(\eta\right) + B_1 \tag{4}$$

By combining Equations (3) and (4) one obtains the logarithmic skin friction law

$$\frac{U_\infty}{u_\tau} = \frac{1}{\kappa} \ln\left(\frac{\delta u_\tau}{\nu}\right) + B + B_1 \tag{5}$$

Recently, due primarily to inconsistencies with trends of experimental data, several researchers have investigated alternatives to the classical theory Barenblatt (1993); George *et al.* (1997); Zagarola & Smits (1998).

Based on extensive data from two independent experiments, this investigation targets three main issues related to the overlap region between the inner and outer parts of turbulent boundary layers under zero pressure gradient: the functional form of the overlap, the extent of the overlap and any Reynolds number dependence that may exist in the overlap parameters.

The experiments were carried out in the MTL wind tunnel Johansson (1992) at the department of mechanics, KTH and the NDF wind tunnel at IIT. At KTH, a seven-meter long flat plate was mounted in the test section of the MTL wind tunnel. Measurements of the turbulent boundary layer were performed at five different streamwise stations, $x = 1.5, 2.5, 3.5, 4.5$, and 5.5 m for ten different speeds. At IIT, a 9 m long and 0.457 m diameter cylinder was mounted in the test section of the NDF-tunnel Hites (1997); Ornt (1999). Measurements were taken at x = 1.84, 3.65, 7.33 m using five free-stream velocities. In both experiments, the measurement of the velocity profiles was done using hot-wire techniques, the skin friction was measured using oil-film interferometry, and the Reynolds numbers based on the momentum thickness ranged from 2,500 to 27,000.
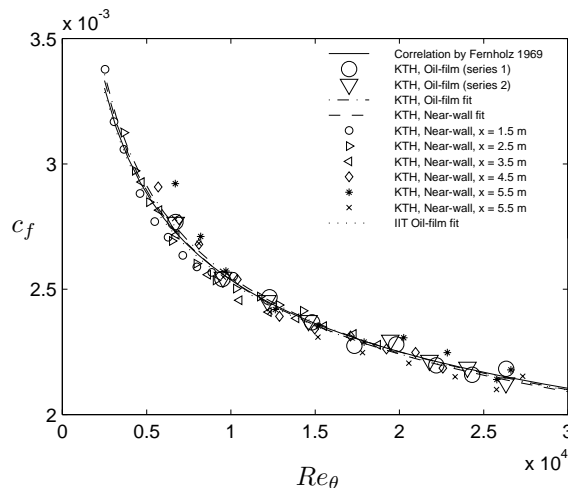
FIGURE 1. Skin-friction coefficient using the oil-film and near-wall methods Österlund (1999), shown with best-fit logarithmic friction laws from Equation (6) and the correlation by Fernholz (1971).

The skin-friction was measured independently of the velocity measurements using oil-film interferometry in a set-up similar to Fernholz *et al.* (1996), see Fig. 1. The reproducibility of c_f obtained with this technique was $\pm 1\%$. A fit to c_f by a variant of the logarithmic skin friction Law (5), namely

$$c_f = 2 \left[\frac{1}{\kappa} \ln(Re_\theta) + C \right]^{-2} , \tag{6}$$

was made and the friction velocity used in scaling the data was calculated as $u_\tau = U_\infty (c_f/2)^{1/2}$. The value of the von Kármán constant determined in this way was, $\kappa = 0.384$ and additive constant, $C = 4.08$. However, it is not possible to determine the additive constants B and B_1 by this method. In Fig. 1, the results from the oil-film measurements together with the values of the skin friction determined from the mean velocity by the near-wall technique Österlund (1999), are shown together with the calculated best fits using Equation (6). The determined logarithmic skin-friction laws agree very well with each other and also with the correlation developed by Fernholz (1971).

In order to investigate the scaling in the overlap, a normalized slope of the mean velocity profile,

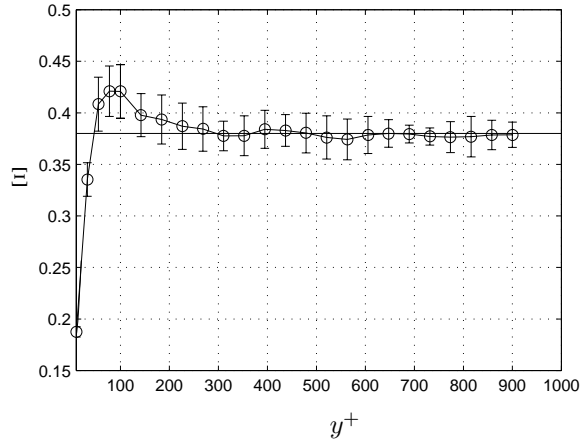$$\Xi = \left(y^+ \frac{d\overline{U}^+}{dy^+} \right)^{-1} , \tag{7}$$

FIGURE 2. Normalized slope of mean profile, Ξ, shown in inner
scaling; only the part of the profiles in which $\eta < 0.15$ was used
and the horizontal line corresponds to $\kappa = 0.38$

was utilized. In a logarithmic region of the profiles Ξ is constant and equal
to κ. The value of Ξ was calculated by taking an average of the individual
profiles at a constant wall distance in inner scaling while omitting the part
of the profiles where $\eta > M_o$. Similarly, the profiles were again averaged at
constant outer-scaled distances from the wall for $y^+ > M_i$. The parameters
M_i and M_o are the inner and outer limits of the overlap region. In Figs. 2
and 3, the Ξ values averaged over all Reynolds numbers for the KTH data
are shown together with error bars representing a 95% confidence interval. A
region where a nearly constant Ξ very accurately represents the data is evident
in both figures. This clearly supports the existence of a logarithmic overlap
region within the appropriate range of the parameters M_i and M_o. The choice
of the appropriate limits was subsequently selected based on the y values where
the error bar deviates significantly from the horizontal line in the figures. This
was based on an iteration of the limits until a consistent result was obtained.
The resulting values for the inner and outer limits are $M_i \approx 200$ and $M_o \approx 0.15$,
respectively. Taking κ as the average value within the determined limits gives
a κ of about 0.38.

Next, the additive constant B was investigated by looking at the deviation
of the mean velocity from the log-function with the aid of the variable Ψ, where

$$\Psi = \overline{U}^+ - \frac{1}{\kappa} \ln y^+. \tag{8}$$

The variable Ψ is also constant in a region governed by a logarithmic law. The
average of the value of Ψ at a constant wall distance is taken for all Reynolds
numbers while omitting the part of the profile where $\eta > M_o$. In Fig. 4, Ψ
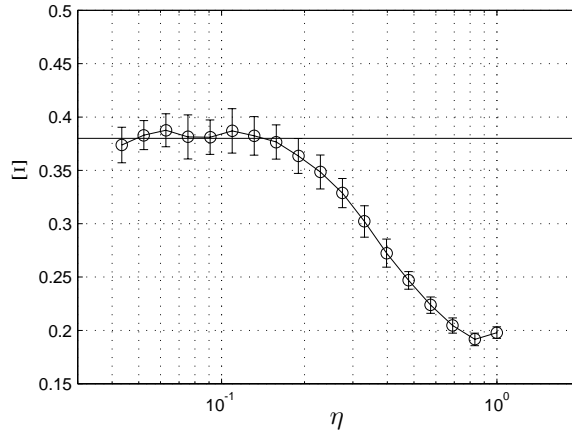
FIGURE 3. Normalized slope of mean profile, Ξ, shown in outer scaling; only the part of the profiles in which $y^+ > 200$ was used and the horizontal line corresponds to $\kappa = 0.38$

averaged over all Reynolds numbers for the KTH data is shown with error bars corresponding to a 95% confidence interval. A constant value is found over a wide range in y^+, again indicating a log-layer. Calculating the average of Ψ within the proposed limits, M_i and M_o, gives $B = 4.1$. A slight under-shoot can be seen around $y^+ = 200$ this was found to be caused by a slight Reynolds number variation of B in the lower part of the range. Using only Reynolds numbers above 8–10×10^3 eliminates the small under-shoot.

In addition to using the above described method to determine the log-law constants, we used the traditional procedure to determine κ and B by performing a least-squares type of fit to the mean velocity profiles. In Fig. 5, κ was calculated by fitting a log-law relation for each profile using the following traditional limits of the fit: $M_i = 50$ and $M_o = 0.15$. The process was also repeated with the newly established limits of $M_i = 200$ and $M_o = 0.15$. The value of κ obtained when using the traditional limits varies with Reynolds number and gives about the commonly used value of 0.41 at low Reynolds numbers. Using the new limits, that are more representative of the logarithmic law, again yields a value of $\kappa \approx 0.38$ independent of Reynolds number.

To investigate the existence of a power-law as proposed recently by several authors Barenblatt (1993); George *et al.* (1997), the following diagnostic function averaged for the KTH data is shown in Fig. 6:

$$\Gamma = \frac{y^+}{\overline{U}^+} \frac{d\overline{U}^+}{dy^+} \tag{9}$$
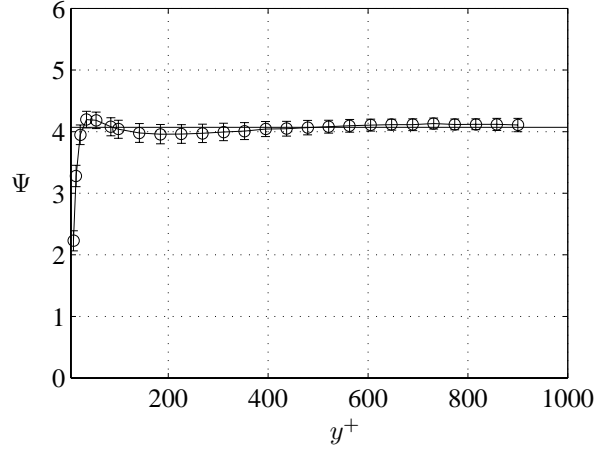
FIGURE 4. Deviation from the logarithmic function using $\kappa = 0.38$; the horizontal line correspond to $B = 4.1$, and only the part of the profiles in which $\eta < 0.15$ is shown.

The function Γ should be a constant in a region governed by a power-law. However, no region of constant Γ is depicted in Fig. 6, in particular when compared to Figs. 2 and 3. This clearly indicates that a power-law relation is less representative of the entire region of overlap between M_i and M_o.

Therefore, based on analysis of data from two recent experimental investigations it can be concluded that a logarithmic overlap region, between the inner and outer parts of the mean velocity profiles, exists for $Re_\theta > 6,000$. Establishing, based on the analysis of the data, an inner limit of the region at about $y^+ = 200$ and an outer limit at $\eta = 0.15$ demonstrated the validity of the logarithmic relation with $\kappa = 0.38$, $B = 4.1$ and $B_1 = 3.6$ ($\delta = \delta_{95}$). The data will be made available in electronic form (http://www.mech.kth.se/~jens/zpg/).
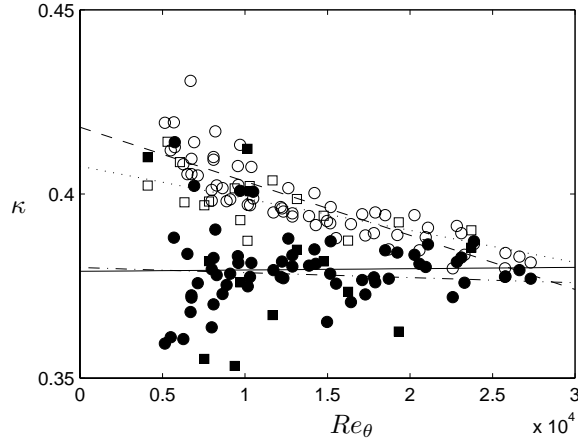
FIGURE 5. The von Kármán constant determined by a least-squares fit, with the outer limit fixed at $\eta = 0.15$ and the inner limit at M_i; ○: KTH, $M_i = 50$. ●: KTH, $M_i = 200$. Dashed line: KTH, linear fit, $M_i = 50$. Solid line: KTH, linear fit, $M_i = 200$. □: IIT, $M_i = 50$. ■: IIT, $M_i = 200$. Dotted line: IIT, linear fit, $M_i = 50$. Dash dotted line: IIT, linear fit, $M_i = 200$.
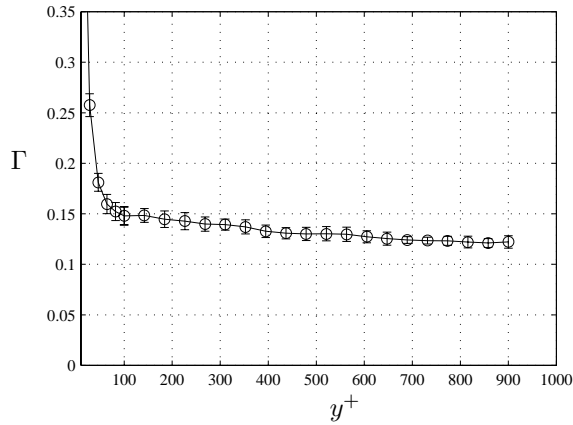

FIGURE 6. The power-law diagnostic function Γ; only the part of the profiles in which $\eta < 0.15$ is shown.

References

BARENBLATT, G. I. 1993 Scaling laws for fully developed turbulent shear flows. part 1. basic hypotheses and analysis. *J. Fluid Mech.* **248**, 513–520.

FERNHOLZ, H. H. 1971 Ein halbempirisches Gezetz für die Wandreibung in kompressiblen turbulenten Grenzschichten bei isothermer und adiabater Wand. *ZAMM* **51**, 148–149.

FERNHOLZ, H. H., JANKE, G., SCHOBER, M., WAGNER, P. M. & WARNACK, D. 1996 New developments and applications of skin-friction measuring techniques. *Meas. Sci. Technol.* **7**, 1396–1409.

GEORGE, W. K., CASTILIO, L. & WOSNIK, M. 1997 Zero-pressure-gradient turbulent boundary layer. *Applied Mech. Reviews* **50**, 689–729.

HITES, M. H. 1997 Scaling of high-reynolds number turbulent boundary layers in the national diagnostic facility. PhD thesis, Illinois Institute of Technology.

JOHANSSON, A. V. 1992 A low speed wind-tunnel with extreme flow quality - design and tests. In *Prog. ICAS congress 1992*, pp. 1603–1611. ICAS-92-3.8.1.

MILLIKAN, C. B. 1938 A critical discussion of turbulent flows in channels and circular tubes. In *Proceedings of the Fifth International Congress of applied Mechanics*.

ORNT, W. 1999 Measurements of wall-shear stress in turbulent channel and boundary layer flows. Master's thesis, Illinois Institute of Technology.

ÖSTERLUND, J. M. 1999 Experimental studies of zero pressure-gradient turbulent boundary-layer flow. PhD thesis, Department of Mechanics, Royal Institute of Technology, Stockholm.

ZAGAROLA, M. V. & SMITS, A. J. 1998 Mean-flow scaling of turbulent pipe flow. *J. Fluid Mech.* **373**, 33–79.

Paper 2

Mean-flow characteristics of High Reynolds Number Turbulent Boundary Layers from Two Facilities

By Jens M. Österlund[1], Arne V. Johansson[1], Hassan M. Nagib[2] & Michael H. Hites[2]

[1]Dept. of Mechanics, KTH, SE-100 44 Stockholm, Sweden
[2]Illinois Institute of Technology, Chicago, IL 60616, USA

The mean flow characteristics of a zero-pressure-gradient turbulent boundary layer were investigated through extensive measurements in two different high-quality flow facilities, the MTL wind-tunnel at KTH and the NDF wind-tunnel at IIT. The study was focused on exploring the characteristics of the overlap region. The wall shear stress is a key quantity in this type of study and was in both the present experiments determined through oil-film interferometry. Also a large range of reynolds numbers is crucial for this type of study. We here report results, for Reynolds numbers based on the momentum thickness ranging from 2,500 to 27,000. Contrary to the conclusions of some recent publications, the present analysis of the data reveals no significant Reynolds number dependence for the parameters describing the overlap region using the classical logarithmic relation. However, the data analysis demonstrates that the viscous influence extends within the buffer region to $y^+ \approx 200$, compared to the previously assumed limit of $y^+ \approx 50$. Therefore, the lowest Re_θ value where a significant logarithmic overlap region exists is about 6,000. This probably explains the Reynolds number dependence had been found from the data analysis of some previous experiments. The parameters of the logarithmic overlap region are here found to be constant and are estimated to be: $\kappa = 0.38$, $B = 4.1$ and $B_1 = 3.6$.

1. Introduction

In the traditional theory, the overall character of a turbulent boundary layer is given by the two disparate inner and outer length scales. The outer length scale is commonly taken as the thickness of the boundary layer δ, and the inner length scale as the viscous length $l^* = \nu/u_\tau$, where $u_\tau = \sqrt{\tau_w/\rho}$ is the friction velocity, τ_w is the skin friction and ρ is the density of the air. Dimensional analysis of the dynamic equations with boundary conditions leads to a scaling

of the mean velocity profile in the inner and the outer parts of the boundary layer in the form:

$$\overline{U}^+ = \frac{\overline{U}}{u_\tau} = f\left(y^+\right); \quad \overline{y}^+ = \frac{yu_\tau}{\nu} \tag{1}$$

$$\frac{U_\infty - \overline{U}}{u_\tau} = F\left(\eta\right); \quad \eta = \frac{y}{\delta} \tag{2}$$

At sufficiently large Reynolds numbers, it is assumed that there is a region of overlap, $\nu/u_\tau \ll y \ll \delta$, where the law of the wall (1) and the defect law (2) simultaneously hold. Matching (Millikan 1938) the relations (1) and (2) gives one of the classical results in turbulence theory, *i.e.*, the logarithmic overlap region: in inner variables,

$$\overline{U}^+ = \frac{1}{\kappa} \ln\left(y^+\right) + B \tag{3}$$

and in outer variables

$$\frac{U_\infty - \overline{U}}{u_\tau} = -\frac{1}{\kappa} \ln\left(\eta\right) + B_1. \tag{4}$$

By combining Equations (3) and (4) one obtains the logarithmic skin friction law

$$\frac{U_\infty}{u_\tau} = \frac{1}{\kappa} \ln\left(\frac{\delta u_\tau}{\nu}\right) + B + B_1. \tag{5}$$

Recently, due primarily to inconsistencies with trends of experimental data, several researchers have investigated alternatives to the classical theory Zagarola & Smits (1998*b*,*a*); George *et al.* (1996); Barenblatt & Chorin (1999).

Based on extensive data from two independent experiments, this investigation targets three main issues related to the overlap region between the inner and outer parts of turbulent boundary layers under zero pressure gradient, viz, the functional form of the overlap, the extent of the overlap and any Reynolds number dependence that may exist in the overlap parameters.

2. Experimental Setup

The experiments were carried out in the MTL-wind tunnel (Johansson 1992) at the department of mechanics, KTH and the NDF-tunnel at IIT (Nagib *et al.* 1994; Hites 1997).

At KTH a seven meter long flat plate was mounted in the test section of the MTL wind-tunnel. Zero pressure gradient was achieved by adjusting the walls opposite to the plate. The variation of the velocity outside the boundary layer was measured to be less than 0.2% of the free stream velocity. The boundary layer was tripped using DYMO brand embossing tape with letters "V". Measurements of the turbulent boundary layer were performed at five different streamwise stations, $x = 1.5, 2.5, 3.5, 4.5,$ and 5.5 m at 10 different

wind-tunnel speeds. Hot-wire anemometry probes, mounted on a traversing system protruding from the plate, were used to measure the velocity in the boundary layer. Before the wind tunnel was turned on, the initial distance from the wall to the probe was measured, with an accuracy of $\pm 5\mu$m, using a microscope. During the traversing process, a distance measuring laser system was mounted under the plate looking directly at the wire through a Plexiglas plug. This arrangement made it possible to continuously measure the sensor distance to the wall, for $y < 2$ mm, when the tunnel was running. The error of the absolute wall distance measurements was $\pm 5\mu$m

At IIT a 9 m long cylinder was mounted in the test section of the NDF-tunnel. Measurements were taken (Hites 1997; Ornt 1999) along the boundary layer of this axisymmetric body (0.46 m diameter), at x = 1.84, 3.65, 7.33 m, using five different free-stream velocities. A short fetch of sandpaper roughness was used to trigger the transition in the boundary layer at the same location for all velocities. The traversing mechanism was mounted in the side wall of the NDF wind tunnel and the initial position of the probe with respect to the surface was regularly monitored using an optical cathetometer from outside the test section. The adjustable test-section ceiling was also positioned for a zero-pressure gradient along the cylinder model. The high quality of the test section flow has been previously reported by Nagib *et al.* (1994). Additional details are found in the PhD thesis of Hites (1997).

3. Skin Friction Measurements

3.1. *Near-wall method*

One method to determine the skin friction is to measure the mean velocity gradient close to the wall in the viscous sub-layer; i.e., in the region where $y^+ < 3$. This method is not practical when making measurements at high Reynolds numbers and/or low Prandtl numbers. In the current experiments this would require performing accurate measurements closer than 30 μm from the wall, which is not possible with hot-wire techniques. Therefore, a new method to determine the wall-shear stress has been developed. The method is based on determining the skin friction from the measured velocity profile in the inner layer, using the law of the wall (Equation (1)) at a distance from the wall where it is possible to make accurate measurements. The measured velocity profile is fitted to the law-of-the-wall in a procedure minimizing the mean-square error. This is similar to what is done when using the Clauser method in the logarithmic region of the velocity profile. The problem with using the Clauser method is obvious since it assumes similarity in the overlap region, which is precisely what we want to investigate. For similar reasons the use of Preston tubes is not desirable here.

In order to utilize accurate mean velocity measurements to evaluate the wall-shear stress, the form of the law-of-the-wall was chosen from available
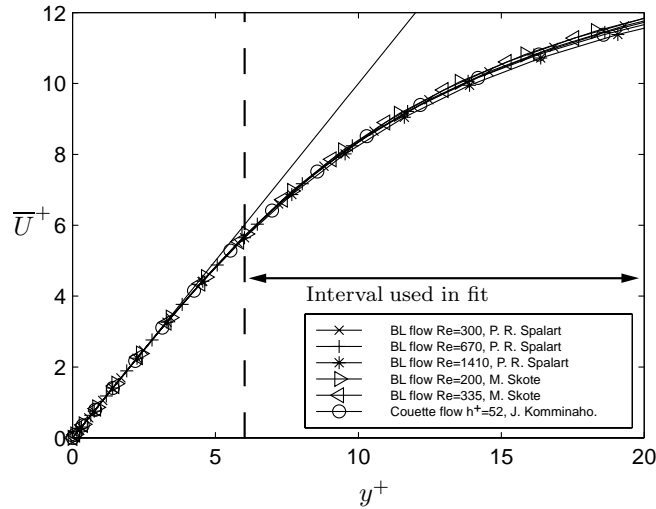
FIGURE 1. Mean velocity from DNS of boundary layer by Spalart (1988) and Skote *et al.* (1998), and Couette flow by Komminaho *et al.* (1996).

direct numerical simulations (DNS) of turbulent shear flows. Since the DNS data are available with great detail in the region where accurate measurements can be achieved and where the measurements are still well within the inner layer, the range $6 < y^+ < 20$ was selected for this near-wall method. In Figure 1, the mean velocity profiles from several recent direct numerical simulations are reproduced. The Couette flow simulation was chosen since it most closely resembles the flow in the inner part of a high Reynolds number turbulent boundary layer. In particular, there is no streamwise pressure gradient in this flow and the total shear stress is constant, over a range of distances from the wall, as shown in Figure 2. Note that for this flow $\overline{\tau}^+ = 1$ for all y^+.

3.2. *Oil-film interferometry*

Oil film interferometry was used in both experiments to measure the skin friction. The basic principle of the method is to measure the deformation of a thin film of oil when subjected to a shear stress on its top surface. A simple and convenient measurement technique is based on illuminating the oil-film by a monochromatic light and recording the change in the generated interference pattern, e.g., with a video camera (see Figure 3). The skin friction is determined from the recording of the fringe patterns and utilizing the wave length of the light source λ, the kinematic viscosity of the oil ν, the refractive index of the oil n, and the angle of the camera axes to the normal of the plate α. The accuracy of the mean skin friction value $\overline{\tau_w}$ measured by this oil-film method is better than $\pm 4\%$ (Fernholz *et al.* 1996).
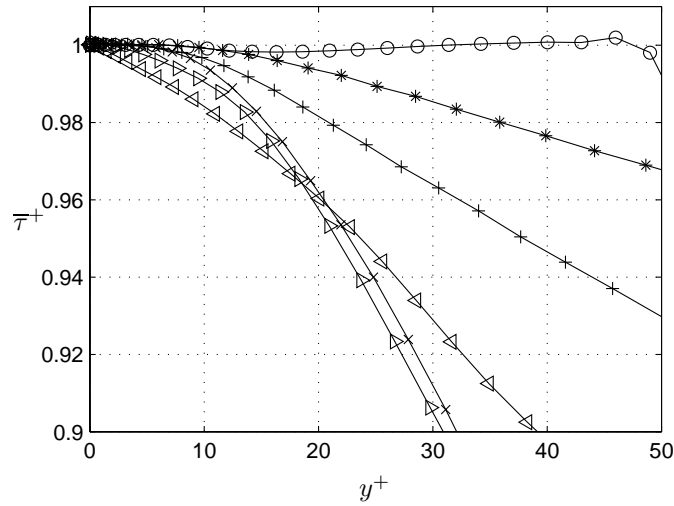
FIGURE 2. Total shear stress from DNS calculations; for legend see Figure 1
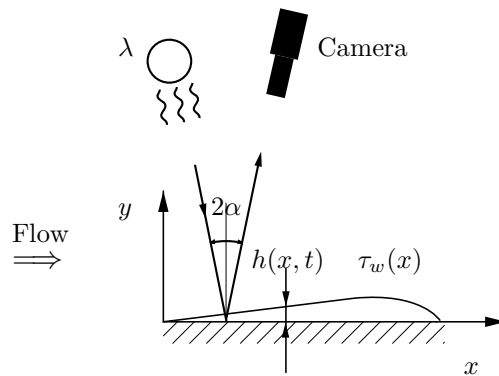

FIGURE 3. Schematic of oil-film technique.

4. Skin Friction Results

The results from the skin friction measurements are summarized in Figure 1. The oil-film measurements from the KTH experiments are plotted together with the skin friction law derived from the similar IIT experiments. Based on the velocity profiles from the KTH experiments the skin friction was also evaluated using the near-wall method.
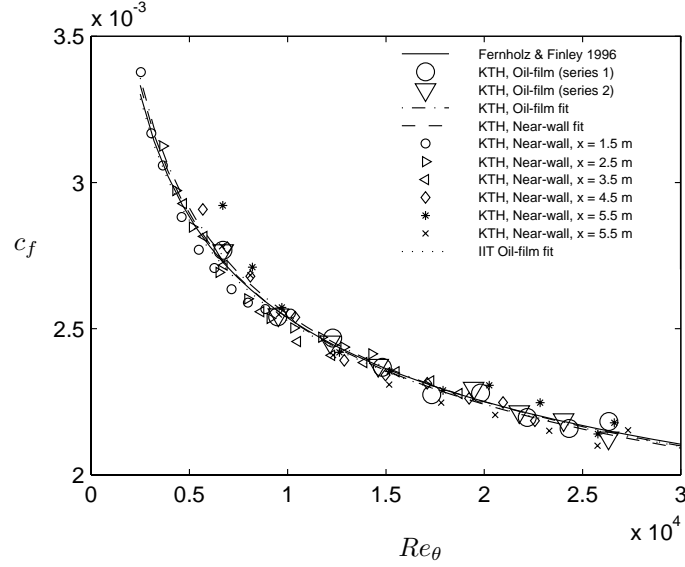
FIGURE 4. Skin-friction coefficient using the oil-film and near-wall methods (paper 8), shown with best-fit logarithmic friction laws from Equation (6) and Fernholz & Finley (1996).

A fit to c_f by a variant of the logarithmic skin friction law (Equation (5)), namely

$$c_f = 2 \left[\frac{1}{\kappa} \ln(Re_\theta) + C \right]^{-2}, \tag{6}$$

was made for each of the data sets and the friction velocity used in scaling the data was then calculated as $u_\tau = U_\infty (c_f/2)^{1/2}$. The value of the von Kármán constant determined in this way was $\kappa = 0.384$ and the additive constant was found to be $C = 4.08$. However, it is not possible to determine the additive constants B and B_1 by this method.

In Figure 1, the results from the oil-film measurements together with the values of the skin friction determined from the mean velocity by the near-wall technique (paper 8), are shown together with the calculated best fits using Equation (6). The resulting logarithmic skin-friction laws agree very well with each other and also with the correlation by Fernholz & Finley (1996).

5. Mean Velocity

In Figure 5, the mean velocity profiles from the 70 experiments at KTH and the 15 data sets from the IIT experiments are shown in inner scaling. A very nice collapse of the data is displayed even far out from the wall. A logarithmic profile with constants from a best fit to the KTH data is also shown. The
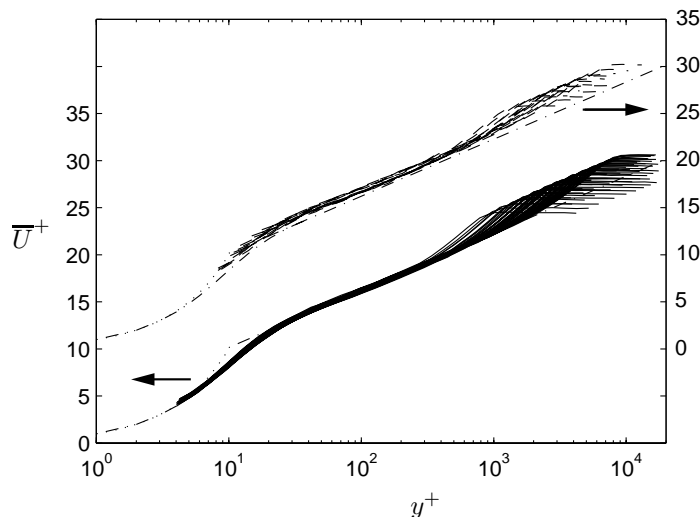
FIGURE 5. Mean velocity inner scaling; solid lines: data from KTH, dashed lines: data from IIT, dash-dotted lines: log-law with constants $\kappa = 0.38$ and $B = 4.1$, and note shift of axis.

constants were found to be: $\kappa = 0.38$, $B = 4.1$ and $B_1 = 3.6$, see section 6. The IIT experiment gives the same value of the von Kármán constant, κ, but different values of the additive constants, which is seen as a vertical shift, from the KTH log-profile, in figures 5 and 6.

In Figure 6 the same data are replotted using classical outer scaling and the collapse is very good, although the IIT data again shows another value of the additive constant.

The boundary layer thickness δ is a quantity which cannot be exactly defined and is commonly taken as y when $\overline{U}/U_\infty = 0.95$ here denoted δ_{95} and used throughout this article. Other definitions that are often used include the Rotta-Clauser length $\Delta = \delta^* U_\infty / u_\tau$, first used by Rotta (1950), or the Coles δ_{ct} which is defined as the distance to the wall of the point of maximum deviation from the log law, in the outer part of the boundary layer. Comparisons between the defect mean-velocity profiles in the outer part of the boundary layer using different outer length scales are shown in Figure 7. To put them all on the same axis each scaling is multiplied by the mean of the ratio between the length scale under consideration and δ_{95}, for all Reynolds numbers.

Except for the scaling with θ, which is somewhat worse than the others, no clear preference for an outer scale can be derived from this figure. However, the Rotta-Clauser length scale, Δ, has the advantage of being an integral length
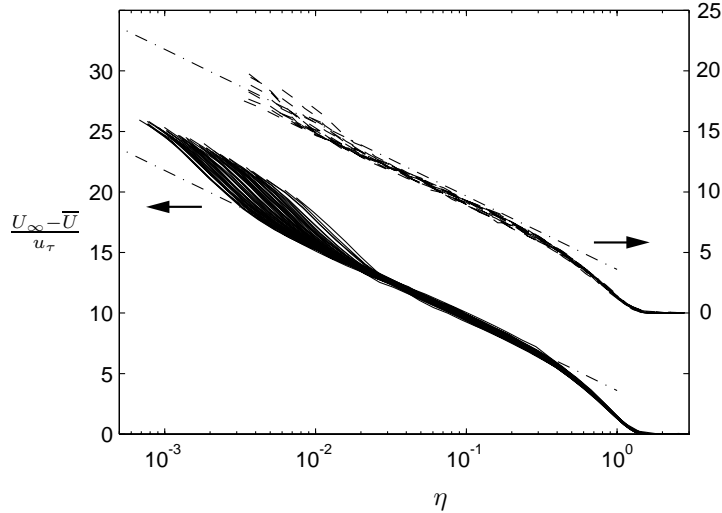
FIGURE 6. Mean velocity outer scaling; solid lines: data from
KTH, dashed lines: data from IIT, dash-dotted lines: log-law
with constants $\kappa = 0.38$ and $B_1 = 3.6$, and note shift of axis.

scale and is thus easier to determine from experimental data, also with relatively
few data points across the boundary layer.

To further investigate the mutual scaling between the thicknesses we show
the normalized outer length scale ratios in Figure 8. The ratios are multiplied
by the average ratio over all Reynolds numbers to better show the variation.
The Rotta-Clauser and Coles boundary layer thicknesses again show a similar
behavior and increase slightly with Re_θ. The ratio of the momentum thickness
and δ_{95} exhibits the opposite behavior and decreases with Re_θ. This explains
the poor scaling with θ in Figure 7.

Coles (1962) formed a uniformly valid velocity profile by adding the inner
(1) and outer (2) solutions and removing the common part to arrive at:

$$
\begin{aligned}
\overline{U}^+ &= f(y^+) - F(y/\delta_{ct}) + F(y/\delta_{ct})_{cp} \\
&= f(y^+) + \frac{\Pi}{\kappa} w(y/\delta_{ct}),
\end{aligned}
\tag{7}
$$

where $w(y/\delta_{ct})$ is the Coles wake function and Π the wake strength. The
wake function is normalized so that $w(1) = 2$. In Figure 9, the calculated
wake strength, Π, is shown as a function of Re_θ. For low values of Re_θ, the
magnitude of Π is increasing with increasing Re_θ, but for $Re_\theta > 10,000$ the
data indicate an approximately constant value. A slightly decreasing trend was
observed by Coles for intermediate Reynolds numbers. Here, any such trend is
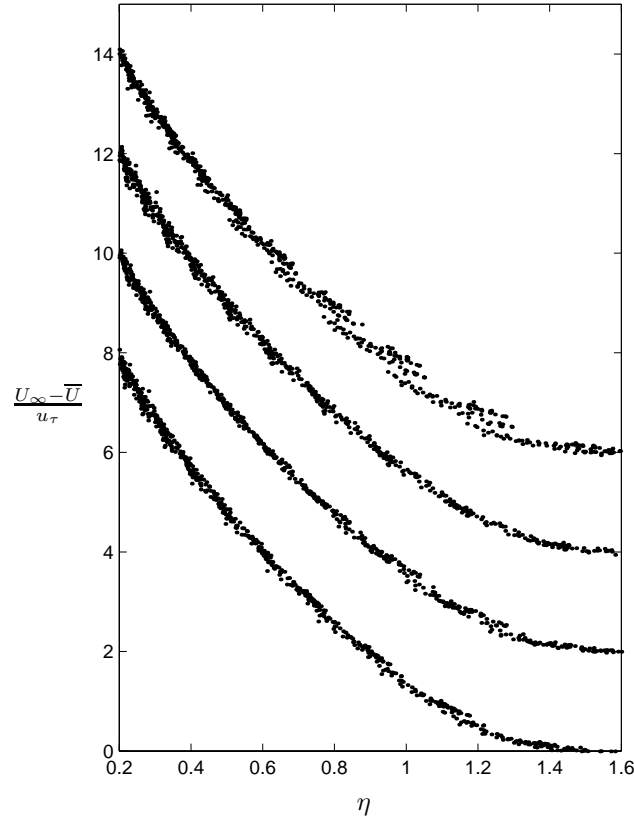
FIGURE 7. Mean velocity in outer scaling with the different definitions for η: y/δ_{95}, $(y/\Delta)\langle\Delta/\delta_{95}\rangle$, $(y/\delta_{ct})\langle\delta_{ct}/\delta_{95}\rangle$ and $(y/\theta)\langle\theta/\delta_{95}\rangle$, where averages over Re_θ are denoted by$\langle...\rangle$; note data is shifted upwards with an increment of 2 units between each set.

hardly visible. A difference from the data analysis of Coles is that we here have used the new values ($\kappa = 0.38$, $B = 4.1$) for the log-layer parameters. This explains the lower value of Π obtained here as compared to the value of about 0.55 found by Coles (with $\kappa = 0.41$, $B = 5$).
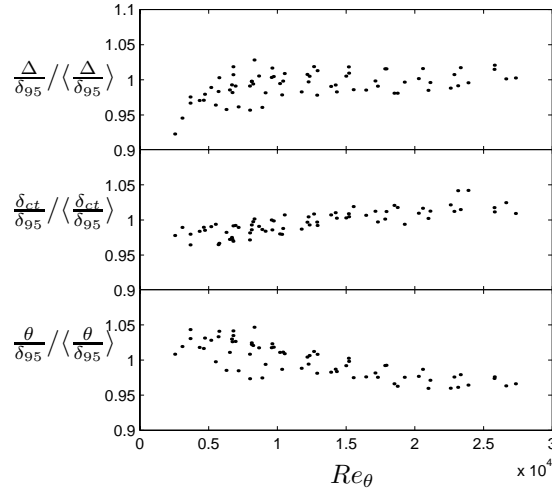
FIGURE 8. Normalized outer length scale ratios, where $\langle...\rangle$ denotes mean values for all Re_θ cases.

6. Scaling in the overlap region

In order to investigate the scaling in the overlap region, a normalized slope of the mean velocity profile,

$$\Xi = \left(y^+ \frac{d\overline{U}^+}{dy^+} \right)^{-1},$$ (8)

was utilized. In a logarithmic region of the profiles Ξ is constant and equal to κ. The value of Ξ was calculated by taking an average of the individual profiles at a constant wall distance in inner scaling while omitting the part of the profiles where $\eta > M_o$. Similarly, the profiles were again averaged at constant outer-scaled distances from the wall for $y^+ > M_i$. The parameters M_i and M_o are the inner and outer limits of the overlap region. In Figures 10 and 11, the averaged Ξ is shown together with error bars representing a 95% confidence interval. A region where a nearly constant Ξ very accurately represents the data is evident in both figures. This clearly supports the existence of a logarithmic overlap region within the appropriate range of the parameters M_i and M_o. The choice of the appropriate limits was subsequently selected based on the y values where the error bar deviates significantly from the horizontal line in the figures. This was based on an iteration of the limits until a consistent result was obtained. The resulting values for the inner and outer limits are $M_i \approx 200$ and $M_o \approx 0.15$, respectively. Taking κ as the average value within the determined limits gives a κ of about 0.38.
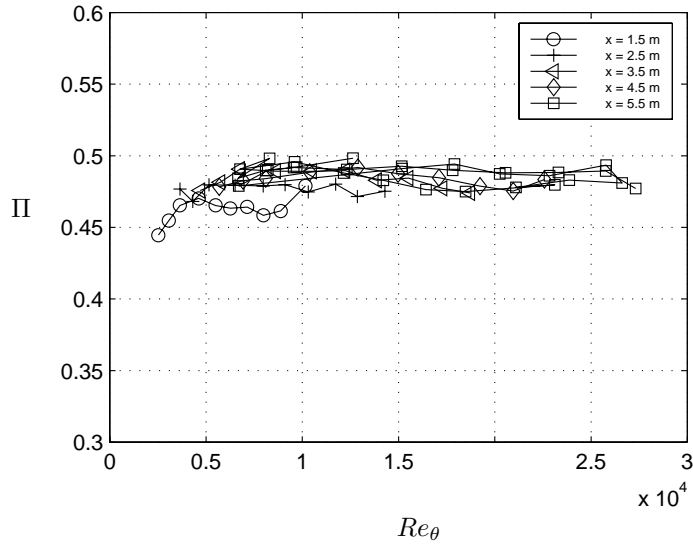
FIGURE 9. Strength of the wake component, Π. Measurements from five different X-positions is shown. Note that this is not directly comparable to Coles strength of the wake since the new set of log-law constants was used, see section 6.
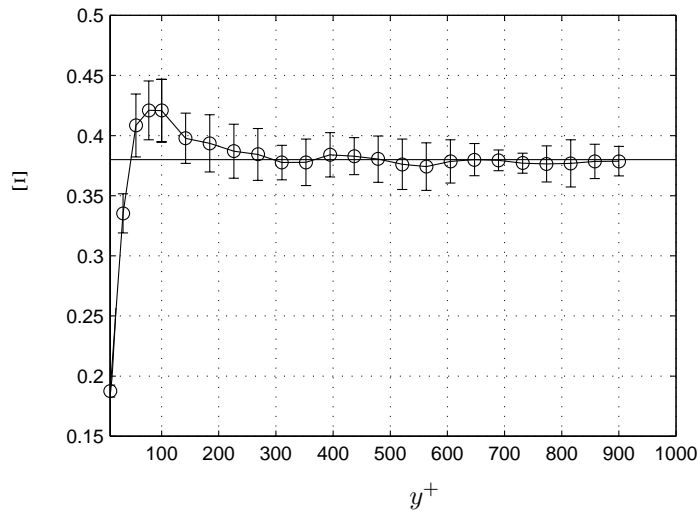

FIGURE 10. Normalized slope of mean profile, Ξ, shown in inner scaling; only the part of the profiles in which $\eta < 0.15$ was used and the horizontal line corresponds to $\kappa = 0.38$
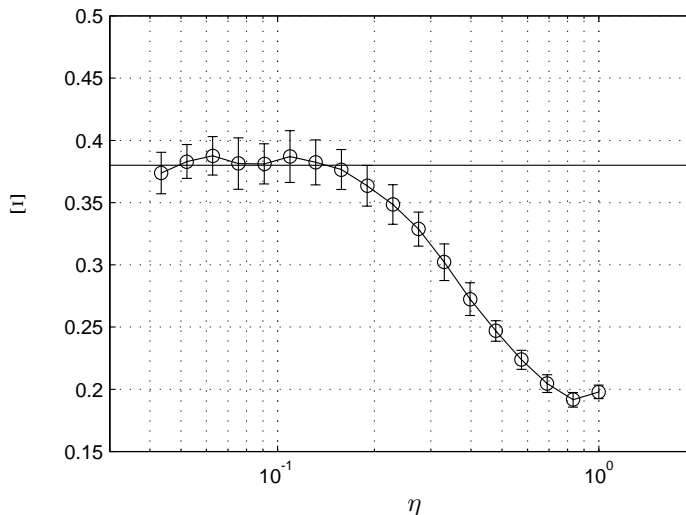
FIGURE 11. Normalized slope of mean profile, Ξ, shown in outer scaling; only the part of the profiles in which $y^+ > 200$ was used and the horizontal line corresponds to $\kappa = 0.38$

Next, the additive constants B and B_1 were investigated by looking at the deviation of the mean velocity profiles, in inner and outer scaling, from the log-profile with the aid of the variables Ψ and Ψ_1, where

$$\Psi = \overline{U}^+ - \frac{1}{\kappa} \ln y^+ \tag{9}$$

$$\Psi_1 = \frac{U_\infty - \overline{U}}{u_\tau} + \frac{1}{\kappa} \ln \eta \tag{10}$$

The variables Ψ and Ψ_1 are also constant in a region governed by a logarithmic law. The average of the value of Ψ and Ψ_1, respectively, at a constant wall distance is taken for all Reynolds numbers while omitting the part of the profile where $\eta > M_o$ in the calculation of Ψ and $y^+ < 200$ in the calculation of Ψ_1. In Figure 12, Ψ is shown with error bars corresponding to the standard deviation. A constant value is found over a wide range in y^+, again indicating a log-layer. Calculating the average of Ψ within the proposed limits, M_i and M_o, gives $B = 4.1$. In Figure 13 Ψ_1 is presented in the same manner as for Ψ and gives the value of the additive constant in the outer scaled log-law $B_1 = 3.6$. Note that the constant B_1 depends on the definition of δ. Here δ_{95} was used.

In addition to using the above described method to determine the log-law constants, we used the traditional procedure to determine κ and B by performing a least-squares type of fit to the mean velocity profiles. In Figure 14, κ was calculated by fitting a log-law relation for each profile using the following

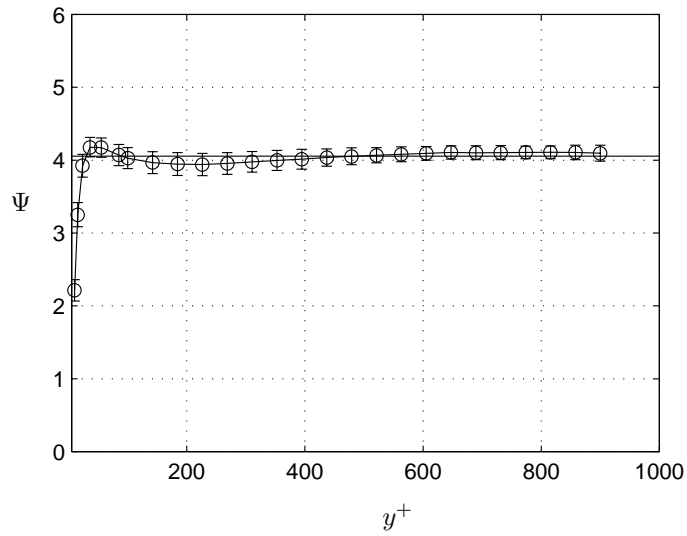FIGURE 12. The logarithmic intercept Ψ, using $\kappa = 0.38$. The horizontal line corresponds to $B = 4.1$, and the data were evaluated using only the part of the profiles in which $\eta < 0.15$.
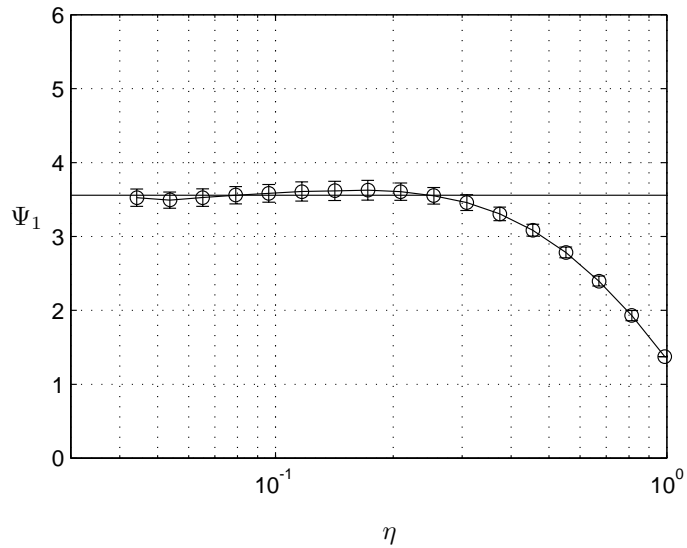

FIGURE 13. The logarithmic intercept Ψ_1, using $\kappa = 0.38$. The horizontal line corresponds to $B_1 = 3.6$, and the data were evaluated using only the part of the profiles in which $y^+ > 200$.
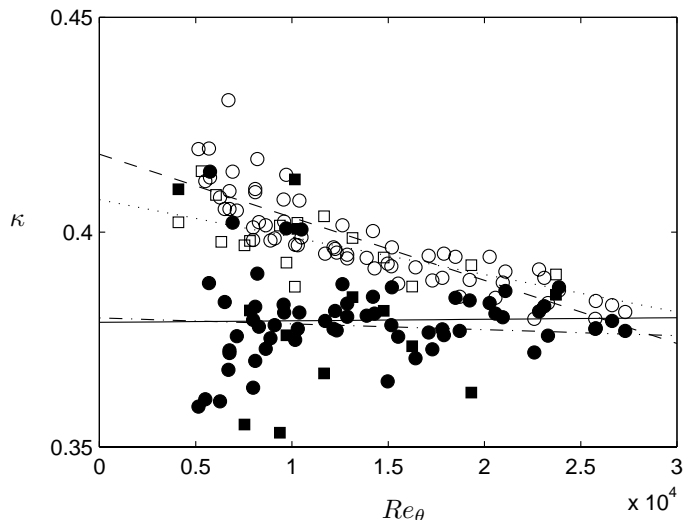
FIGURE 14. The von Kármán constant determined by a least-squares fit, with the outer limit fixed at $\eta = 0.15$ and the inner limit at M_i; ∘: KTH, $M_i = 50$. •: KTH, $M_i = 200$. Dashed line: KTH, linear fit, $M_i = 50$. Solid line: KTH, linear fit, $M_i = 200$. □: IIT, $M_i = 50$. ■: IIT, $M_i = 200$. Dotted line: IIT, linear fit, $M_i = 50$. Dash dotted line: IIT, linear fit, $M_i = 200$.

traditional limits of the fit: $M_i = 50$ and $M_o = 0.15$. The process was also repeated with the newly established limits of $M_i = 200$ and $M_o = 0.15$. The value of κ obtained when using the traditional limits varies with Reynolds number and gives about the commonly used value of 0.41 at low Reynolds numbers. This is then followed by a decreasing trend with increasing Reynolds number. Using the new limits, that are more representative of the logarithmic law, again yields a value of $\kappa \approx 0.38$ independent of Reynolds number.

To investigate the existence of a power-law as proposed recently by several authors Barenblatt (1993); George *et al.* (1997), the following diagnostic function is plotted in Figure 15.

$$\Gamma = \frac{y^+}{\overline{U}^+} \frac{d\overline{U}^+}{dy^+} \tag{11}$$

The function Γ should be a constant in a region governed by a power-law. However, no region of constant Γ is evident in Figure 6, in particular when compared to Figures 10 and 11. This clearly indicates that a power-law relation is less representative of the entire region of overlap between M_i and M_o.
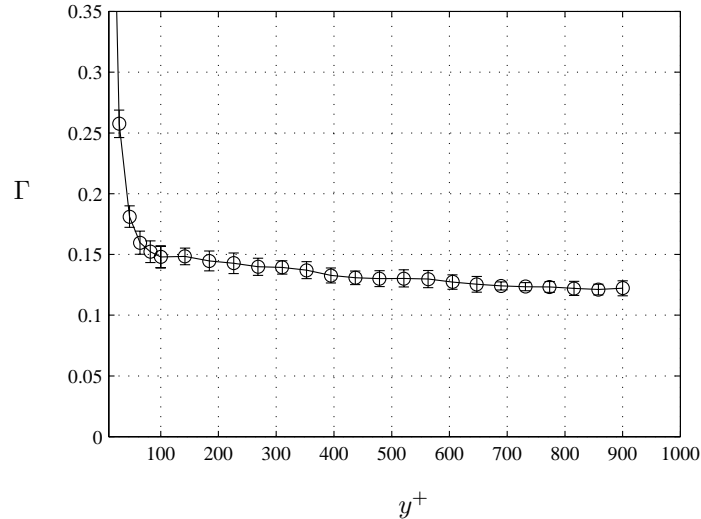
FIGURE 15. The power-law diagnostic function Γ, evaluated using only the part of the profiles in which $\eta < 0.15$.

7. Concluding Remarks

Based on analysis of data from two recent experimental investigations it can be concluded that a logarithmic overlap region, between the inner and outer parts of the mean velocity profiles, exists for $Re_\theta > 6,000$. Establishing, based on the analysis of the data, an inner limit of the region at about $y^+ = 200$ and an outer limit at $\eta = 0.15$ demonstrated the validity of the logarithmic relation. This logarithmic overlap region found differs from that found by Zagarola & Smits (1998a) based on measurements in the Superpipe facility. Where they found the values $\kappa = 0.436$ and $B = 6.15$. This may suggest that the matching of the inner layer with the outer flow results in a slightly different overlap region in the two flow cases; namely, the zero pressure gradient boundary layer and the pressure-gradient driven pipe flow. This is perhaps not totally surprising since the overlap region depends on both the inner and the outer layers and the outer flow is different in the pipe flow from that for the boundary layer. The found value of the von Kármán constant is slightly less than the commonly accepted value of 0.41. Evaluation of the recent high Reynolds number experiment in the German-Dutch wind-tunnel by Fernholz *et al.* (1995) also yields a significantly lower value of the von Kármán constant. Re-evaluation of a carefully selected set of existing experiments would be of great importance for this issue, but out of scope for this article.

8. Acknowledgments

References

BARENBLATT, G. I. 1993 Scaling laws for fully developed turbulent shear flows. part 1. basic hypotheses and analysis. *J. Fluid Mech.* **248**, 513–520.

BARENBLATT, G. I. & CHORIN, A. J. 1999 Self-similar intermediate structures in turbulent boundary layers at large reynolds numbers. PAM 755. Center for Pure and Applied Mathematics, University of California at Berkeley.

COLES, D. E. 1962 The turbulent boundary layer in a compressible fluid. R 403-PR. The RAND Corporation, Santa Monica, CA.

FERNHOLZ, H. H. & FINLEY, P. J. 1996 The incompressible zero-pressure-gradient turbulent boundary layer: An assessment of the data. *Prog. Aerospace Sci.* **32**, 245–311.

FERNHOLZ, H. H., JANKE, G., SCHOBER, M., WAGNER, P. M. & WARNACK, D. 1996 New developments and applications of skin-friction measuring techniques. *Meas. Sci. Technol.* **7**, 1396–1409.

FERNHOLZ, H. H., KRAUSE, E., NOCKEMANN, M. & SCHOBER, M. 1995 Comparative measurements in the canonical boundary layer at $re_{\delta_2} < 6 \cdot 10^4$ on the wall of the german-dutch windtunnel. *Phys. Fluids* **7** (6), 1275–1281.

GEORGE, W. K., CASTILIO, L. & KNECHT, P. 1996 The zero pressure gradient turbulent boundary layer. *Tech. Rep.* TRL-153. Turbulence Research Laboratory, SUNY at Buffalo.

GEORGE, W. K., CASTILIO, L. & WOSNIK, M. 1997 Zero-pressure-gradient turbulent boundary layer. *Applied Mech. Reviews* **50**, 689–729.

HITES, M. H. 1997 Scaling of high-reynolds number turbulent boundary layers in the national diagnostic facility. PhD thesis, Illinois Institute of Technology.

JOHANSSON, A. V. 1992 A low speed wind-tunnel with extreme flow quality - design and tests. In *Prog. ICAS congress 1992*, pp. 1603–1611. ICAS-92-3.8.1.

KOMMINAHO, J., LUNDBLADH, A. & JOHANSSON, A. V. 1996 Very large structures in plane turbulent couette flow. *J. Fluid Mech.* **320**, 259–285.

MILLIKAN, C. B. 1938 A critical discussion of turbulent flows in channels and circular tubes. In *Proceedings of the Fifth International Congress of applied Mechanics*.

NAGIB, H., HITES, M., WON, J. & GRAVANTE, S. 1994 Flow quality documentation of the national diagnostic facility. In *18th AIAA Aerospace Ground Testing Conference, Colorado Springs, CO*. AIAA paper 94-2499.

ORNT, W. 1999 Measurements of wall-shear stress in turbulent channel and boundary layer flows. Master's thesis, Illinois Institute of Technology.

ROTTA, J. C. 1950 Über die Theorie der Turbulenten Grenzschichten. Mitt. M.P.I. Ström. Forschung Nr 1, also available as NACA TM 1344.

SKOTE, M., HENKES, R. & HENNINGSON, D. 1998 Direct numerical simulation of self-similar turbulent boundary layers in adverse pressure gradients. In *Flow, Turbulence and Combustion*, , vol. 60, pp. 47–85. Kluwer Academic Publishers.

SPALART, P. R. 1988 Direct simulation of a turbulent boundary layer up to $Re_\theta = 1410$. *J. Fluid Mech.* **187**, 61–98.

ZAGAROLA, M. V. & SMITS, A. J. 1998*a* Mean-flow scaling of turbulent pipe flow. *J. Fluid Mech.* **373**, 33–79.

ZAGAROLA, M. V. & SMITS, A. J. 1998*b* A new mean velocity scaling for turbulent boundary layers. In *Proceedings of FEDSM'98*.

Paper 3

Turbulence Statistics of Zero Pressure Gradient Turbulent Boundary Layers

By Jens M. Österlund & Arne V. Johansson

Dept. of Mechanics, KTH, SE-100 44 Stockholm, Sweden

Single-point turbulence statistics are here reported for zero pressure-gradient boundary layers at Reynolds numbers based on the momentum thickness in the range $2530 < Re_\theta < 27300$. The experiments were performed in the MTL wind-tunnel at the Department of Mechanics at KTH in Stockholm. A seven m long flat plate was mounted in the test section and the experiments were performed at 5 different streamwise positions. The velocity was measured using hot-wire techniques and the mean wall shear stress was determined using oil-film interferometry. Reynolds number dependence of the statistical quantities and probe size effects are discussed.

1. Introduction

This paper presents an experimental study of the structure single-point turbulence statistics in zero-pressure-gradient turbulent boundary layers and Reynolds number effects. The Reynolds number in typical applications with boundary layer flow are often several orders of magnitude larger than what is possible to achieve in direct numerical simulations or even compared to what is achievable in most wind-tunnels. Therefore, there is a gap in Reynolds number between practical applications and the experiments which form the basis for our knowledge of turbulence and turbulence modeling. Experiments at high Reynolds number is therefore of primary importance to reveal Reynolds number trends that might have a large influence in many fluid dynamic applications. Recent reviews of Reynolds number effects in wall-bounded shear flows was made by Gad-el-Hak & Bandyopadhyay (1994) and more specifically on zero pressure-gradient boundary layer flow by Fernholz & Finley (1996). Since the publication of the reviews two more experimental studies was published by Smith (1994) and Hites (1997). For low Reynolds numbers results from direct numerical simulations have become available starting with the simulation by Spalart (1988) followed by *e.g.* Skote *et al.* (1998).

The quest for high Reynolds number data is restrained by the availability of large size wind-tunnels but also by the demand for miniaturized flow sensors imposed by the small scales at high Reynolds numbers. In the present experiment a large effort has been put into the design and manufacturing of miniaturized hot-wire sensors, as well as their accurate positioning in the boundary layer.

2. Experimental Set-up

The experiments were performed in the MTL wind-tunnel at KTH. A seven meter long flat plate was mounted in the test section. The plate is a sandwich construction of aluminum sheet metal and square tubes in seven sections plus one flap and one nose part. The flap is 1.5 m long and is mounted in the first diffuser. This arrangement makes it possible to use the first 5.5 m of the plate for the experiment. The plate rests on two longitudinal beams running along the whole test section. The beams can be adjusted to make the plate flat to within ± 0.5 mm. The upper and lower walls of the test section can be moved to adjust the pressure distribution along the plate. The maximum variation in mean velocity distribution along the boundary layer plate was $\pm 0.15\%$. The boundary layer was tripped at the beginning of the plate and the two dimensionality of the boundary layer was checked by measuring the spanwise variation of the wall shear stress τ_w. The maximum spanwise variation in shear velocity $u_\tau = \sqrt{\tau_w/\rho}$ was found to be less than $\pm 0.7\%$. The MTL wind tunnel was designed with low disturbance level as the primary design goal and the extreme flow quality of the MTL wind-tunnel was demonstrated by Johansson (1992). For instance, the streamwise turbulence intensity was found to be 0.02%. The air temperature can be controlled to within ± 0.05 °C, which was very important for this study since the primary measurement technique was hot-wire anemometry.

One of the plate sections was equipped with two circular inserts, one for a plexiglass plug where the measurements took place, and one for the traversing system. The traversing system was fixed to the plate to minimize any vibrations and possible deflections. The positioning of the probes needs to be extremely accurate since at high Reynolds numbers the viscous (wall) scale is less than 10 μm. The distance to the wall from the probe was determined by a high magnification microscope. In addition the wall distance was measured using a laser distance meter placed under the plate looking at the probe through the plexiglass plug. The accuracy of the laser distance meter was $\pm 1\mu$m. This system made it possible to monitor the probe also with the tunnel running. It was also possible to detect probe vibrations since the frequency response of the system was 10 kHz. The absolute error in the determination of the wall distance was within $\pm 5\mu$m.

The ambient conditions were monitored by the measurement computer during the experiments using an electronic barometer and thermometer (FCO 510 from Furness Ltd., UK). The reference conditions used in the calibration of the

probes were determined using a Prandtl tube in the free-stream directly above the measurement station. The pressure and temperature were again monitored at all times during the experiments using a differential pressure transducer and a thermometer connected directly to the measurement computer. The accuracy of the pressure measurement was 0.25 % and the accuracy of the temperature measurement was 0.02 °C.

Constant temperature hot-wire anemometry was used in all velocity measurements. All hot-wire probes were designed and built at the lab. Three sizes of single-wire probes were used in the experiments with wire diameters of: 2.5, 1.27 and 0.63 μm. Two other types of probes were also used: X- and V-wires. The wire diameter for the X- and V-wire probes was 1.27 μm. The wire-separation for the X-wire probe was 220 μm and the wire length about 300 μm. The wires were placed at an angle of about $\pm 45°$ to the mean flow angle. The V-wire probe had two wires placed at $\pm 45°$ to the mean flow lying in the same horizontal plane. The wire length was 300 μm and the maximum spanwise extent was about 500 μm. The anemometer system (AN1003 from AA lab systems, Israel) had a built-in signal conditioner and the signals from the anemometer were digitized using an A/D converter board (A2000 from National Instruments, USA) in the measurement computer. The A/D converter has 12 bit resolution and four channels which could be sampled simultaneously at rates up to 1 MHz divided by the number of channels used.

The complete experiment was run from a program on the measurement computer which controlled the tunnel velocity, the positioning of probes, digitization of the anemometer signals, monitoring of the pressures and the temperature. This made it possible to design experiments which could be performed relatively quickly since monotonous work with moving probes and registering the parameters involved was done rapidly by the computer. For the double wire measurements the time to perform an measurement was also reduced by streaming the data directly to the hard disk and evaluating only a small amount of the data, for monitoring purpose, during the measurement. This made the time to carry out an experiment very close to the total sampling time plus the traversing time. The main reason for all the effort put into this was to minimize the effect of drift which is always present in any anemometer system. Furthermore, the lifetime of probes with 0.63 μm wire diameter was only a couple of hours at the higher tunnel speeds and to manage both calibration and the measurement before the wire breaks one has to avoid any unnecessary delays. To further reduce drift all instruments were always on and the tunnel was kept running for at least three hours before the experiment was performed. For a detailed description of the experiment, see paper 8.

3. Skin Friction Measurements

Accurate determination of the skin friction in the zero pressure gradient boundary layer is a very difficult task. Only a few independent methods are available:

the floating element *i.e.* measurement of the tangential force of a part of the wall and using the definition of the stress $\tau_w = F/A$, where F is the force on the floating element and A is the area of the floating element, measurement of the velocity gradient at the wall and using $\tau_w = \mu \partial \overline{U}/\partial y$, where μ is the dynamic viscosity of the air, and oil-film interferometry. In oil-film interferometry the deformation of a thin film of oil is registered in time using optical interferometry. It is an independent method since it does not need to be calibrated. Only properties of the oil must be known.

Oil-film interferometry was used to determine the skin friction in this experiment and the adapted method is described by Fernholz *et al.* (1996). Results and comparisons with other experiments and other methods can be found in paper 2 and Österlund *et al.* (1999).

A fit to c_f by a variant of the logarithmic skin friction law (Equation (6)), namely

$$c_f = 2 \left[\frac{1}{\kappa} \ln(Re_\theta) + C \right]^{-2},$$ (1)

was made for each of the data sets and the friction velocity used in scaling the data was then calculated as $u_\tau = U_\infty (c_f/2)^{1/2}$. The value of the von Kármán constant determined in this way was $\kappa = 0.384$ and the additive constant was found to be $C = 4.08$, see Österlund *et al.* (1999).

4. Mean Flow Characteristics

The mean flow characteristics of the turbulent boundary layer, with a focus on the properties of the overlap region, were carefully investigated and are reported in paper 2. The behavior of the boundary layer confirms the traditional two-layer theory with a logarithmic mean velocity profile in the overlap region.

The outer and inner length scales are chosen as δ, the boundary layer thickness and the viscous length $l^* = \nu/u_\tau$, where $u_\tau = \sqrt{\tau_w/\rho}$ is the friction velocity, τ_w is the skin friction and ρ is the density of the air. Dimensional analysis gives the scaling of the velocity in the inner part of the boundary layer, the law-of-the-wall

$$\overline{U}^+ = \frac{\overline{U}}{u_\tau} = f\left(y^+\right); \quad \overline{y}^+ = \frac{y u_\tau}{\nu}$$ (2)

and the scaling in the outer part of the boundary layer, the defect law

$$\frac{U_\infty - \overline{U}}{u_\tau} = F\left(\eta\right) \quad \eta = \frac{y}{\delta}.$$ (3)

At high Reynolds numbers there is a region of overlap, $\nu/u_\tau \ll y \ll \delta$, between the two scalings where both are simultaneously valid. Matching (Millikan 1938) the law-of-the-wall (2) and the defect law (3) in the traditional manner gives

the logarithmic overlap region: in inner variables,

$$\overline{U}^+ = \frac{1}{\kappa} \ln\left(y^+\right) + B \tag{4}$$

and in outer variables

$$\frac{U_\infty - \overline{U}}{u_\tau} = -\frac{1}{\kappa} \ln\left(\eta\right) + B_1. \tag{5}$$

Equations (4) and (5) also relate the skin friction with the Reynolds number and can be combined to give the logarithmic skin friction law

$$\frac{U_\infty}{u_\tau} = \frac{1}{\kappa} \ln\left(\frac{\delta u_\tau}{\nu}\right) + B + B_1. \tag{6}$$

A simplified variant of the logarithmic skin friction law, see equation 1, was fitted to the oil-film experiments and later used in the scaling of the experiments.

In figures 1 and 2 the mean velocity profiles from single-wire measurements in the Reynolds number range $2500 < Re_\theta < 27700$ are shown in inner and outer scaling. Excellent agreement with the above theoretical result is seen also over this wide Reynolds number range. Also shown in the figures are the logarithmic laws with the newly determined values of the log-law constants $\kappa = 0.38$, $B = 4.1$ and $B_1 = 3.6$. The value of the constant B_1 depends on the choice of outer scale. In this paper we use the Rotta-Clauser lengthscale $\Delta = \delta^* U_\infty / u_\tau$, Rotta (1950). As described in paper 2 the Rotta-Clauser length scale is preferred, compared to the other available and equivalent scalings, because it is experimentally more well defined. One should keep in mind, though, that Δ is substantially larger than the boundary layer thickness. $\Delta/\delta_{95} \approx 5.68$. The value of B_1 was determined in paper 2 using δ_{95} but can easily be transformed to the Δ-scaling by

$$B_1^\Delta = B_1^{\delta_{95}} - \frac{1}{\kappa} \log\left(\frac{\Delta}{\delta_{95}}\right), \tag{7}$$

giving the value $B_1^\Delta = 1.62$ used in figure 2.

5. Streamwise turbulence intensity and spatial resolution effects

In any investigation of turbulence statistics spatial averaging due to finite probe size must be carefully addressed. Johansson & Alfredsson (1983) made a detailed experimental investigation of spatial resolution effects for near-wall turbulence measurements and compiled data from the literature to elucidate such effects, see also *e.g.* Comte-Bellot (1976)

The measured velocity from a hot-wire probe is a weighted average over the wire length. That is, the probe will average out variations in the velocity field that are smaller than the length of the wire. Several attempts to address the
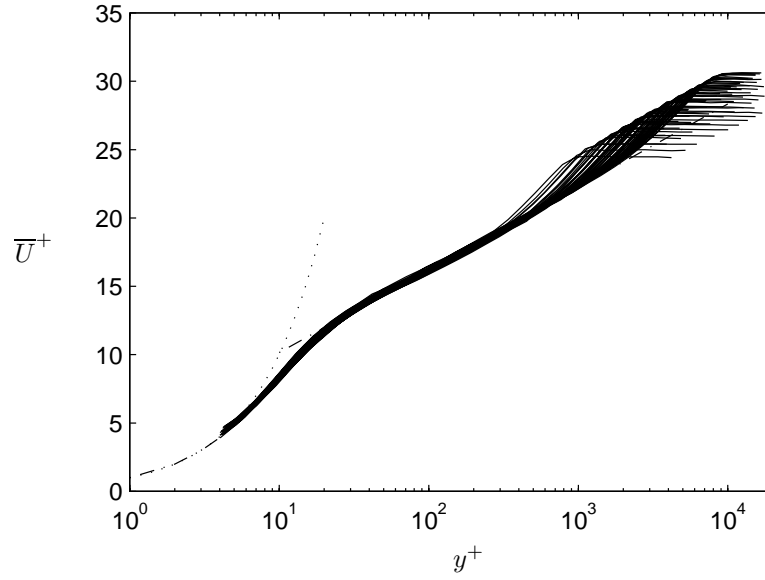
FIGURE 1. Profiles of the mean velocity in inner-law scaling. $2530 < Re_\theta < 27300$. Dash-dotted line: $\frac{1}{0.38} \ln y^+ + 4.1$.
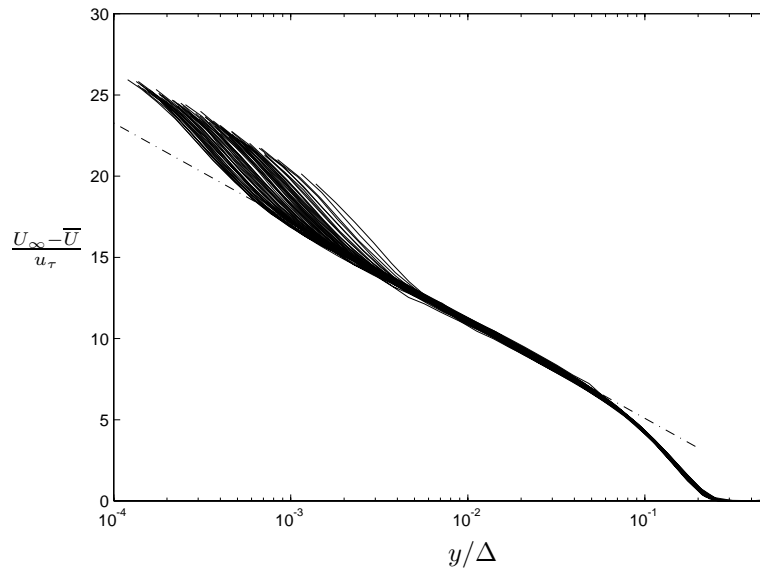

FIGURE 2. Profiles of the mean velocity in outer-law scaling. Log-law constants $\kappa = 0.38$ and $B_1^\Delta = 1.62$. $2530 < Re_\theta < 27300$

problem of spatial averaging have been reported, see *e.g.* Ligrani & Bradshaw (1987) and Willmarth & Bogar (1977).

For double wire probes Österlund (1995) showed that there is a physical limit where further minimization results in thermal crosstalk between the sensing wires that destroys the velocity signal regardless of the spatial resolution. This effect limits the size of double-wire probes to a Péclet number, based on the separation between the wires, to be larger than about 50. The Péclet number is defined as $Pe = RePr = \overline{U}\Delta_w/\chi$, where $\overline{U}$ is the mean velocity, Δ_w is the wire separation and χ the thermometric conductivity [1]. This makes it particularly difficult to design experiments in air because of the low Prandtl number (≈ 0.7). The two contradicting limits: $L^+ < 10$ and $Pe > 50$ result in the discouraging approximate limit $U^+ > 7$ or $y^+ > 10$ for double-wire probes. Considering also the very high turbulence level in the near-wall region the inner limit for accurate double-wire probes probably is larger than $50\nu/u_\tau$ for measurements in air. Note that the only solution, for double-wire probes where the thermal interaction must be negligible is to use another medium like water or oil, with Prandtl numbers of 7 and about 100, respectively. The other route for accurate measurements in the near wall region in air is instead to exploit the thermal interaction, *e.g.* by two parallel wires very close together, as done by Gresko (1988) and Österlund (1995) (see appendix). The latter showed that the Péclet number based on the separation between the wires must be smaller than about 10. The manufacturing of this type of probes where the wires must be placed less than 10 μm from each other is a severe problem, but the rapid development in micro-machining technology may solve this problem in a not too distant future.

In figures 3 and 4 the turbulence intensity $\sqrt{\overline{u^2}}/u_\tau$ is shown in inner and outer scaling for all the measurements. Clearly, it is hard to separate Reynolds number trends from effects of spatial resolution without sorting the data. The lack of scaling can largely be attributed to spatial averaging, but also Reynolds number effects are hidden in the data. We are interested in investigating Reynolds number trends and a subset of the data where $L^+ < 10$ is shown in figure 5. This of course reduces the Reynolds number span but is necessary to remove significant effects of spatial resolution. In the top diagram of figure 5 the turbulence intensities are scaled with the friction velocity and in the bottom diagram with the mean velocity. The latter represents the relative turbulence intensity, the limiting value ($y^+ \to 0$) of which is equal to the relative wall-shear-stress fluctuation intensity. The collapse is about equally good in the viscous sub-layer and the buffer region, $y^+ < 100$ for both scalings. The peak values of the absolute and relative intensities are shown in figure 6. Also shown in figure 6 are corresponding values obtained from direct numerical simulations

---

[1]$\chi = \kappa/\rho c_p$, where κ is the thermal conductivity, ρ the density and c_p the specific heat at constant pressure

J. M. Österlund & A. V. Johansson
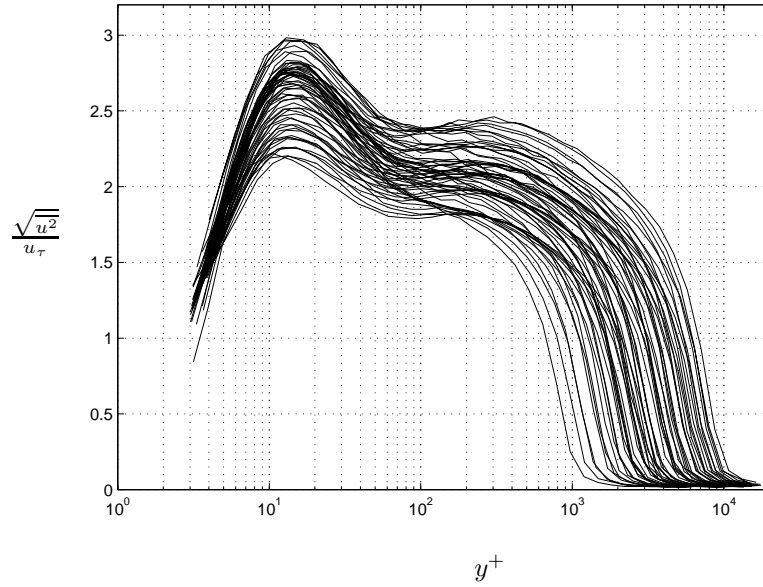
Figure 3. Distributions of streamwise turbulence intensity in inner-law scaling. $2530 < Re_\theta < 27300$ and $6 < L^+ < 60$.

Figure 4. Distributions of streamwise turbulence intensity in outer-law scaling. $2530 < Re_\theta < 27300$ and $6 < L^+ < 60$.

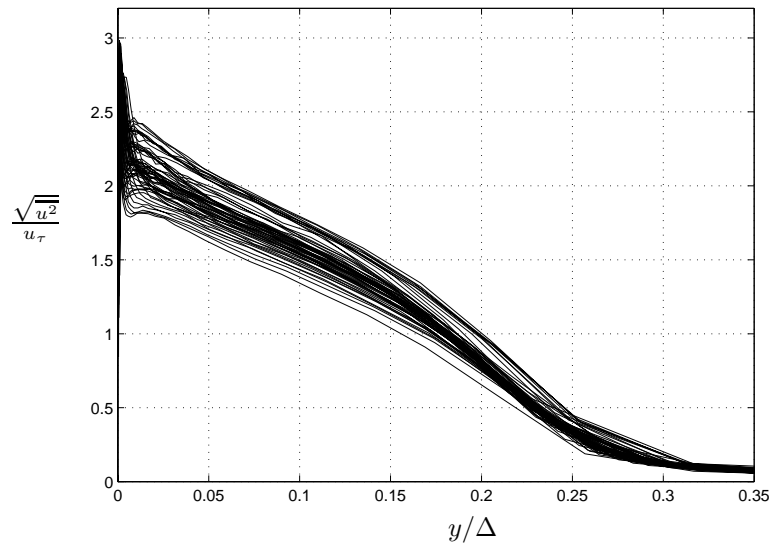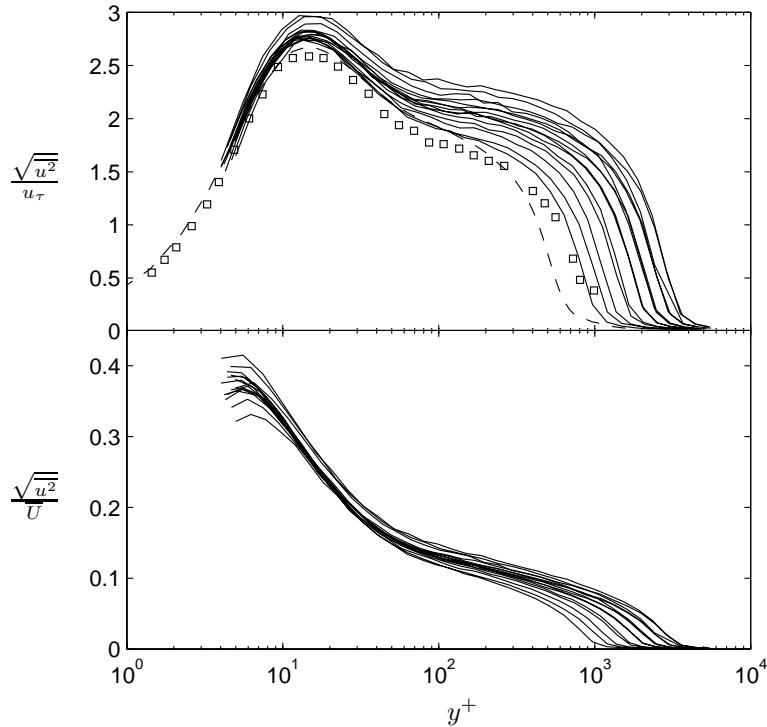FIGURE 5. Streamwise turbulence intensity distributions using only data where $6.5 < L^+ < 10$. Inner-law scaling. $2530 < Re_\theta < 9700$. $--$: Boundary layer simulation at $Re_\theta = 1410$ by Spalart (1988). $\square$: LDV Measurements in boundary layer flow at $Re_\theta = 2420$ by Karlsson & Johansson (1988).

by Spalart (1988), Moser *et al.* (1999) and Alvelius (1999), where the first is a boundary layer simulation and the last two are channel flow simulations. One should keep in mind in the comparisons with the DNS-data that the channel flow has a somewhat different character, where Reynolds number effects on turbulence production etc. can be related to the relative influence of the pressure gradient. This can partly be seen from the integrated form of the mean flow equation. An increasing trend is visible in figure 6 for both scalings. The increase in $\sqrt{\overline{u^2}}/u_\tau$ is about 7% for the present data in this Reynolds number range but the increase in $\sqrt{\overline{u^2}}/\overline{U}$ is only about half of that. For $\sqrt{\overline{u^2}}/u_\tau$ one can observe a significant difference between the channel flow and boundary layer DNS data. The present set of experimental data smoothly extends the boundary layer DNS-results to substantially higher Reynolds numbers, with a continued increase of the maximum intensity. One could expect a levelling off

to occur at high Reynolds numbers. From the results in figure 6 it is not really possible to determine an asymptotic level of $(\sqrt{\overline{u^2}}/u_\tau)_{\max}$ but it can be judged to be at least 2.9.

The limiting value of the relative intensity at the wall is a more difficult quantity of measure. The symbols in figure 6 (lower diagram) represent evaluations at $y^+ \approx 6$. By comparisons with DNS-data we may conclude that these are approximately 10% lower than the limiting values at the wall. Hence, to enable a comparison with the DNS-data, and to give an estimation of the trend of the true limiting intensity value, a line 10% above the measured points is included in figure 6. This line is seen to represent a smooth extension from the DNS-data. At high Reynolds numbers the limiting relative intensity is estimated to be around 0.43. The effects of spatial averaging should be expected only to have marginal influence in figure 6.

The extrapolated (+10%) values in figure 6 are consistent also with measurements of the fluctuating wall shear stress by the hot-wire-on-the-wall technique (paper 5). With that technique a value of about 0.41 was found for $(\sqrt{\overline{\tau_w^2}}/\overline{\tau_w})_{\max}$ at $Re_\theta \approx 10000$. In that work also measurements with a MEMS-sensor of hot-film type are reported. The results were encouraging for this type of technique although further refinements of the sensor design can be foreseen in the near future.

6. Reynolds Stress Components

6.1. *Reynolds normal-stress*

Reynolds normal-stress distributions are presented for inner scaling in figure 7 and for outer scaling of the wall-distance in figure 8. The Reynolds number Re_θ varies from 6930 to 22500. The results for the streamwise component are taken from single-wire measurements, where the wire lengths are in the range $6.6 < L^+ < 24$. For comparison the streamwise component obtained with a X-wire probe at the highest and the lowest Reynolds number are shown as circles in figure 7, and the agreement is excellent in the outer part of the boundary layer but since the X-wire probe has a significant extension in the wall normal direction, it is not possible to measure as close to the wall as with the single wire probe.

Results for the wall-normal $\overline{v^2}$, and the spanwise component $\overline{w^2}$, are obtained with X- and V-wire probes, respectively. A behavior with constant Reynolds stresses is to be expected in the overlap region of the boundary layer. In the present data a plateau becomes visible for the higher Reynolds numbers, at least for $\overline{u^2}$ and $\overline{w^2}$. The decrease of $\overline{v^2}$ for $y^+ < 100$ for the highest Reynolds numbers can probably be ascribed to spatial resolution effects. The probe size for the four highest Reynolds numbers lies in the range $19 < L^+ < 30$. The increase in $\overline{v^2}$ near the wall is most probably an artifact caused by experimental
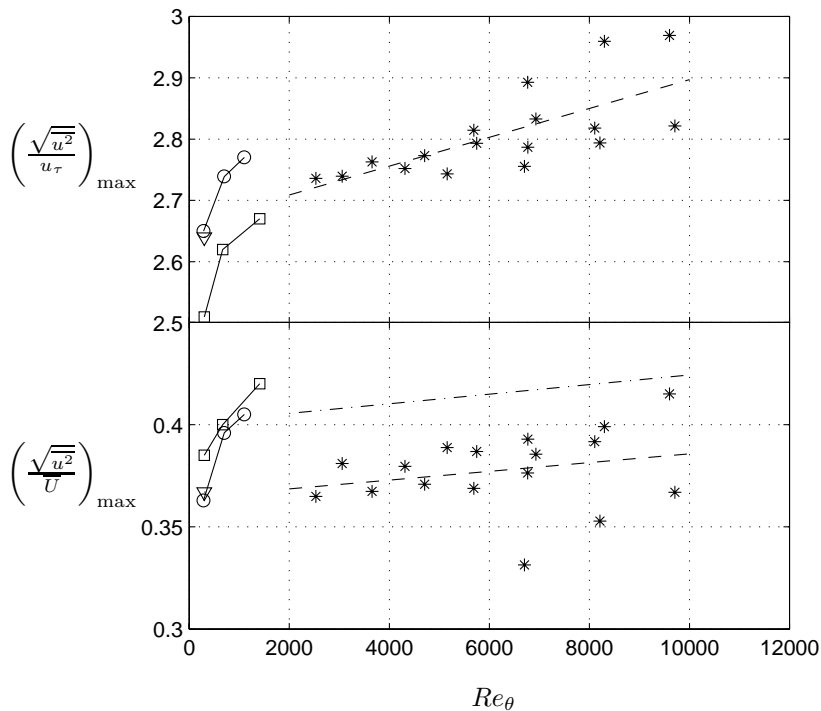
$\left(\dfrac{\sqrt{\overline{u^2}}}{u_\tau}\right)_{\max}$

$\left(\dfrac{\sqrt{\overline{u^2}}}{U}\right)_{\max}$

Re_θ

FIGURE 6. Maximum streamwise turbulence intensity. ∗: Present experiment, $6.5 < L^+ < 10$. Dashed line: linear regression to the present experiment. ○: DNS of channel flow by Moser *et al.* (1999). □: DNS of zero pressure gradient boundary layer by Spalart (1988). ∇: DNS of channel flow by Alvelius (1999).

errors. Also shown are results from measurements with a parallel-wire probe (Österlund 1995) at Reynolds number $Re_\theta = 14500$. It does not have the same problems in the near-wall region but possibly gives a too low value in the outer part of the boundary layer.

The strong increase in $\overline{w^2}$ near the wall is most probably an artifact due to experimental errors. One may speculate that effects of $\partial u/\partial z$ and $\partial v/\partial z$ fluctuations become of significant influence near the wall. The spanwise wire-separation of the V-probe ranges from 29 to 90 viscous length scales in figures 7 and 8.

The fact that the plateau in the Reynolds stresses only is seen for the highest Reynolds numbers is somewhat analogous to the behavior in free shear
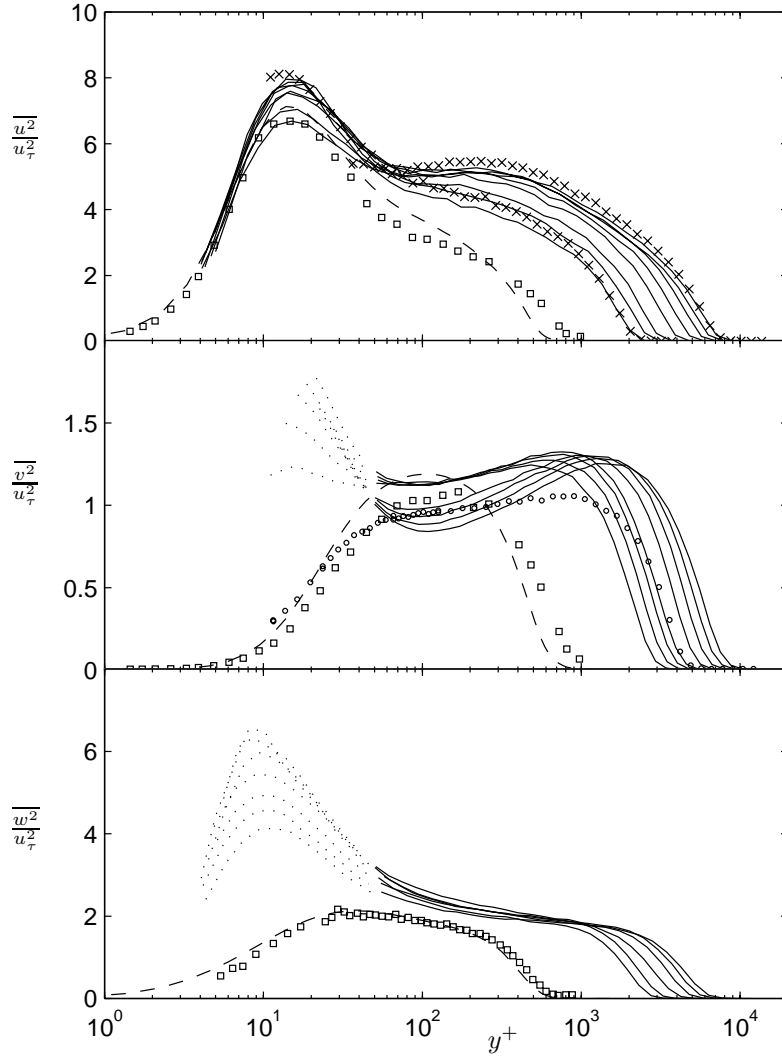
FIGURE 7. Distributions of the Reynolds normal-stress components in inner-law scaling of the wall-distance. $6930 < Re_\theta < 22500$. $\overline{u^2}$ data from a single-wire probe, $\overline{v^2}$ from a X-wire probe and $\overline{w^2}$ from a V-wire probe. $\times$: X-wire probe at Re_θ 6930 and 22500. $\circ$: Parallel-wire probe, $Re_\theta = 14500$. $--$: Boundary layer simulation at $Re_\theta = 1410$ by Spalart (1988). $\square$: LDV Measurements in boundary layer flow at $Re_\theta = 2420$ by Karlsson & Johansson (1988). Dotted parts of curves represent measured data with significant effects of wire-separation etc.
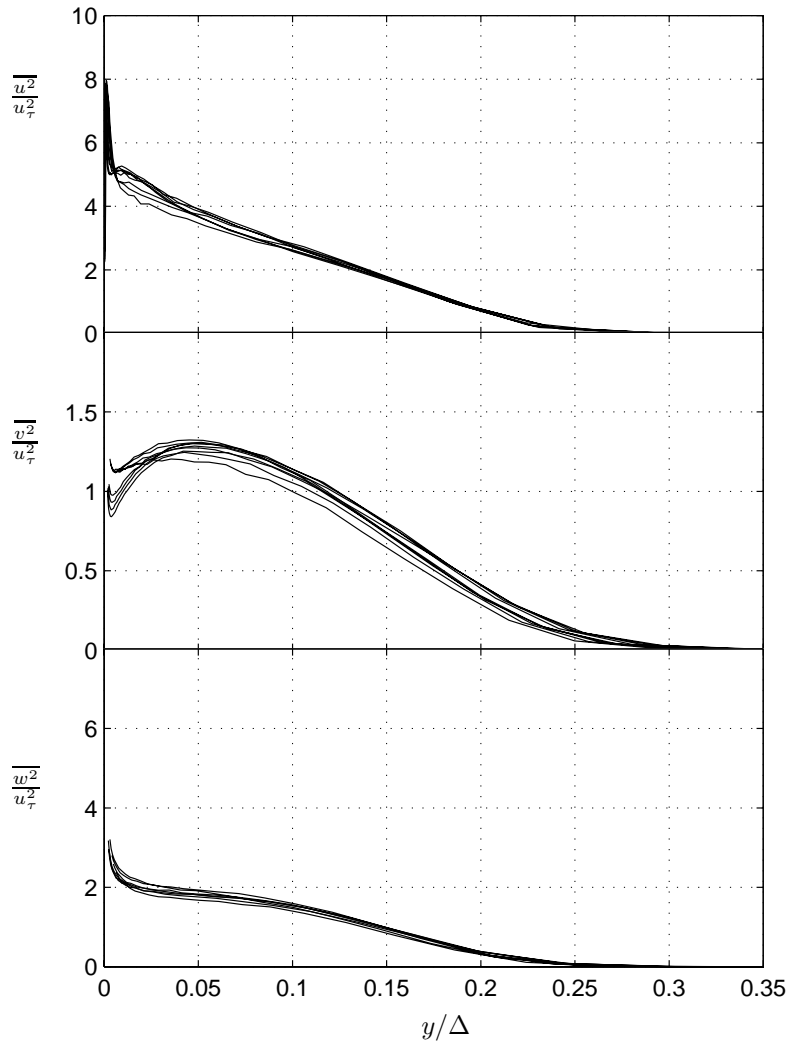
FIGURE 8. Distributions of the Reynolds normal-stress components in outer-law scaling. $6930 < Re_\theta < 22500$. Only data where $y^+ > 50$ are shown for the transverse components.

flows where a self-similar behavior of Reynolds stresses requires a substantially longer development than for the mean velocity.
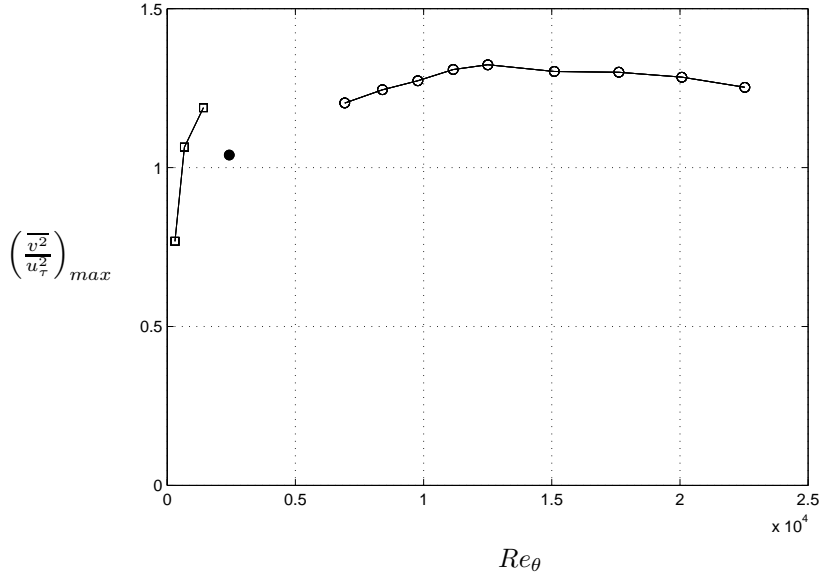
FIGURE 9. Maximum wall-normal turbulence intensity, $\left(\overline{v^2}/u_\tau^2\right)_{max}$. ∘: Present data. Wire separation is $L^+ = 6$ for the low Reynolds number increasing to $L^+ = 18$ for the highest Reynolds number. □: DNS of zero pressure gradient boundary layer by Spalart (1988). ●: LDV measurement by Karlsson & Johansson (1988).

The peak value of $\overline{v^2}$ is seen in figure 9 to increase with the Reynolds number in a manner similar to the variation in the peak value for $\overline{u^2}$. At the high Reynolds number end a decreasing trend is seen that is probably due to spatial averaging effects. The increase in $(\overline{v^2}/u_\tau)_{max}$ for $Re_\theta < 13000$ seems consistent with the low Reynolds number DNS-results. Fernholz & Finley (1996) reported max-values of about 1.4 for $Re_\theta = 20920$ obtained with a probe size of about 26 in wall-units. This is in reasonable agreement with the results in figure 9.

6.2. Reynolds shear-stress

Distributions of the Reynolds shear-stress $\overline{uv}$ are shown in figures 10 and 11 in inner and outer scaling, respectively. Experimental errors due to the large probe size at the high Reynolds numbers gives large uncertainties of the measurements in the near-wall region, $y^+ < 200$. The Reynolds number variation of the shear-stress peak value is shown in figure 12. The peak values show an increasing trend with Reynolds number that flattens out very close to unity for Reynolds numbers above about 15000. The increasing trend at low Reynolds numbers
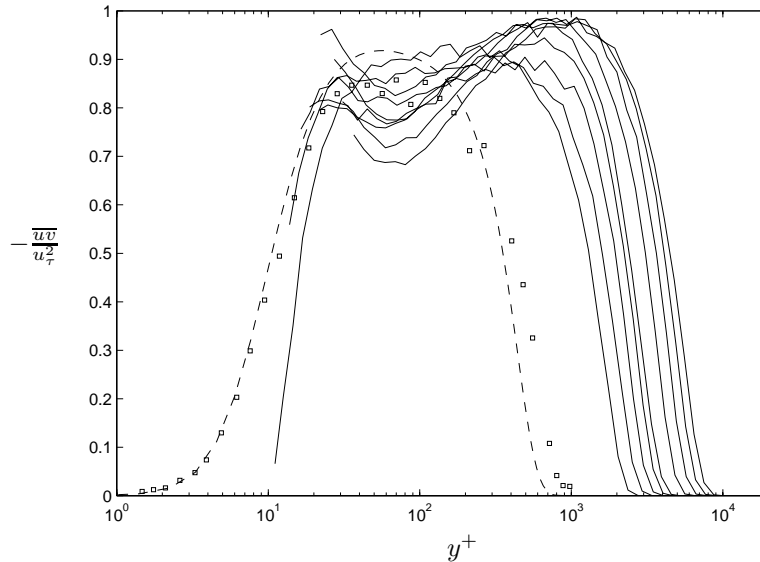
FIGURE 10. Reynolds shear stress in inner-law scaling of
the wall-distance. —:Present data, from a X-wire probe,
$6930 < Re_\theta < 22500$. $--$: Boundary layer simulation at
$Re_\theta = 1410$ by Spalart (1988). $\square$: LDV Measurements in
boundary layer flow at $Re_\theta = 2420$ by Karlsson & Johansson
(1988).

also here seems consistent with the DNS-results. The shear-stress correlation
coefficient is shown in figures 13 and 14. A wide region with a value of about
0.4 is observed and agrees well with earlier reported results for the correlation
coefficient.

The ratio of the Reynolds shear stress to $\overline{q^2}$ (twice the kinetic energy)
is sometimes referred to as the structure parameter. In eddy viscosity-based
two equation models of turbulence one normally assumes this parameter to
be equal to 0.15 to give the standard C_μ-value of 0.09 ($\nu_T = C_\mu k^2/\epsilon$). The
0.15-value is assumed to be valid in general for thin shear layers with produc-
tion approximately balancing the dissipation (the Bradshaw assumption). The
values in figure 15 are significantly higher than what would be expected from
the Bradshaw assumption, especially for the highest Reynolds numbers.

The ratio of the wall-normal to streamwise turbulence intensities is shown
in figure 16, and may be compared with $\sqrt{\overline{w^2}/\overline{u^2}}$ in figure 17. In the log-layer
(below $y/\Delta \approx 0.03$, see figure 2) these two anisotropy parameters are roughly
equal.

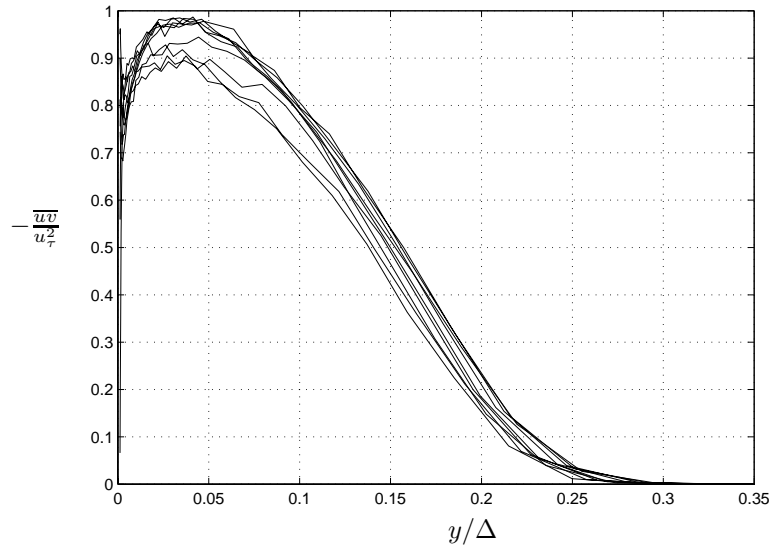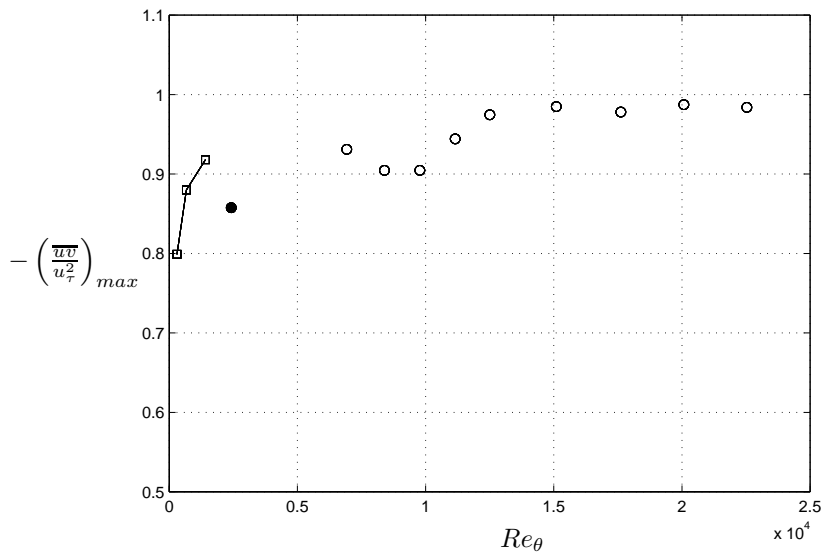FIGURE 11. Reynolds shear stress in outer-law scaling.

FIGURE 12. Maximum value of the shear-stress component.
∘: Present data. □: DNS of zero pressure gradient boundary
layer by Spalart (1988). •: LDV Measurement by Karlsson &
Johansson (1988).
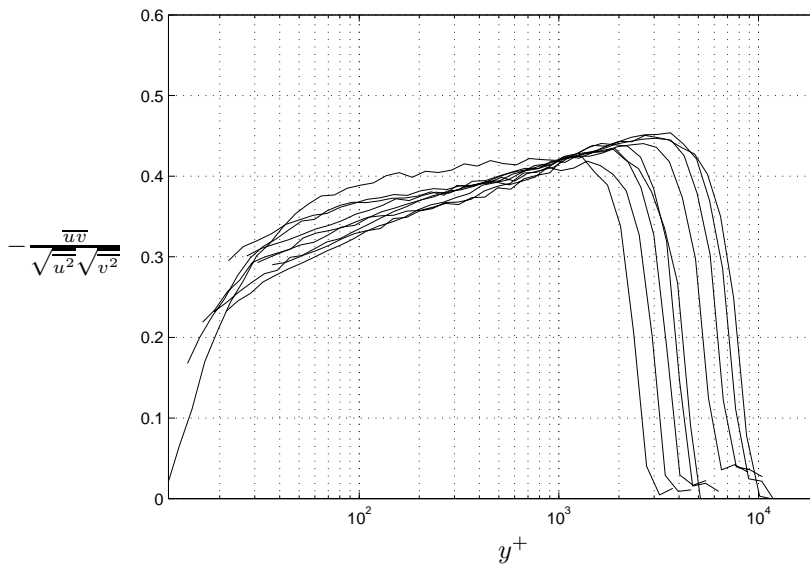
FIGURE 13. Reynolds shear stress correlation coefficient in inner-law scaling.
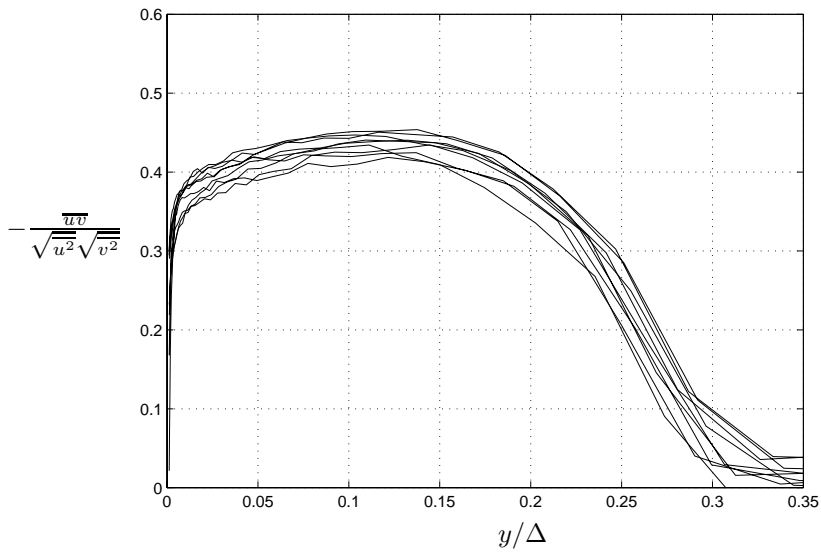
FIGURE 14. Reynolds shear stress correlation coefficient in outer-law scaling.
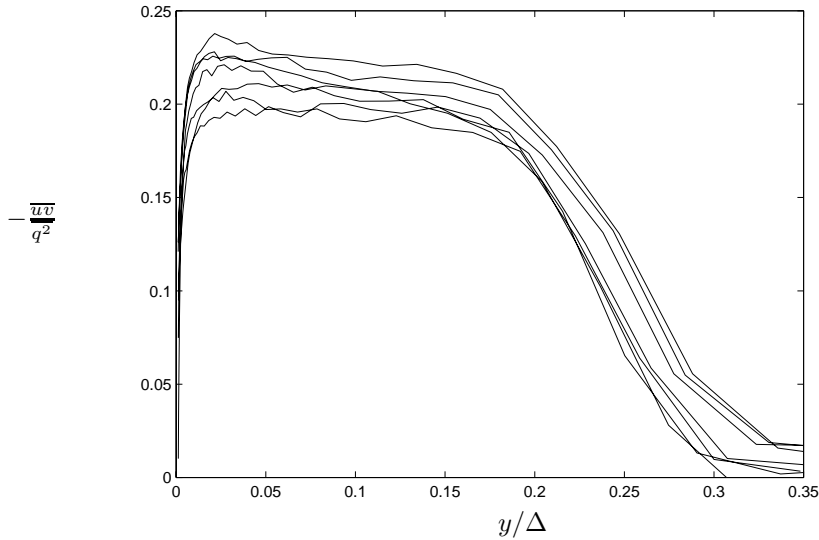
FIGURE 15. Structure parameter in outer-law scaling.

Twice the kinetic energy is shown with inner and outer y-scaling in figures 18 and 19. Also here we may observe a plateau that develops for high Reynolds numbers in the log-layer (figure 18).

The third order moment of the probability density function describes the asymmetry or skewness of the signal. Figures 20 and 21 show the skewness and flatness factors

$$S_u = \frac{\overline{u^3}}{\overline{u^2}^{3/2}} \tag{8}$$

$$F_u = \frac{\overline{u^4}}{\overline{u^2}^2}, \tag{9}$$

of the streamwise velocity component. In inner scaling an approximate collapse of the skewness and flatness profiles are observed in the whole inner layer. Correspondingly, we see a collapse with Δ-scaling in the outer part. The high values near the boundary layer edge are caused by the intermittent character of the turbulence there. One can observe that the minimum flatness value is found at the same location as that for the zero-crossing of the skewness. This position is close to that for the maximum turbulence intensity. This observation is accordance with earlier findings, see *e.g.* Johansson & Alfredsson (1982). The high flatness closer to the wall is associated with the intermittent character of strong sweep type of motions.
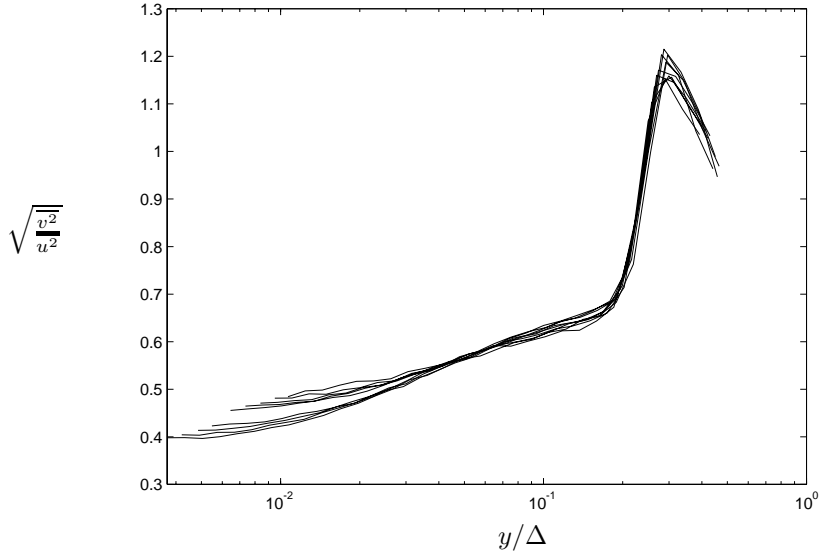
FIGURE 16. Anisotropy parameter in outer scaling.

7. Probability Density Functions

In figure 22 the probability density distributions are shown for different regions in the boundary layer. The high positive skewness value near the wall is associated with a highly asymmetric probability density distribution at *e.g.* $y^+ = 5$. The long positive tail at this position can be interpreted as being caused by sweep type of motions originating from positions far from the wall. A successive change to a negative skewness and corresponding asymmetry of the probability density distribution is seen in figure 22. To illustrate the variation of the width of the probability density distribution, an example of a mean velocity profile is shown in figure 23 together with the limits enclosing 95% of the samples.

7.1. *Joint probability densities*

The joint probability density distributions of u and v are shown in figure 24 for various distances from the wall. The direction of the main axis of the ellipse-like curves is directly related to the correlation coefficient, which in figure 24 was seen to be roughly constant over a wide region of y-values.

$$\sqrt{\dfrac{\overline{w^2}}{\overline{u^2}}}$$
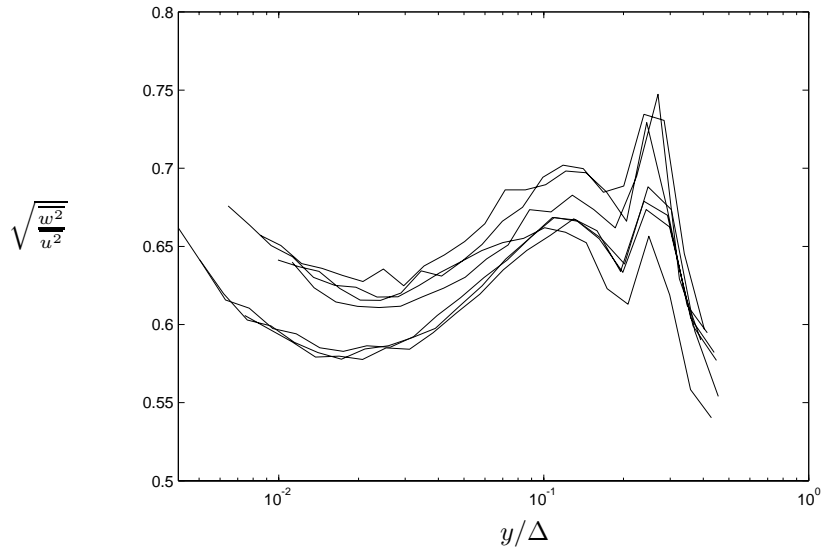
FIGURE 17. Anisotropy parameter in outer scaling.
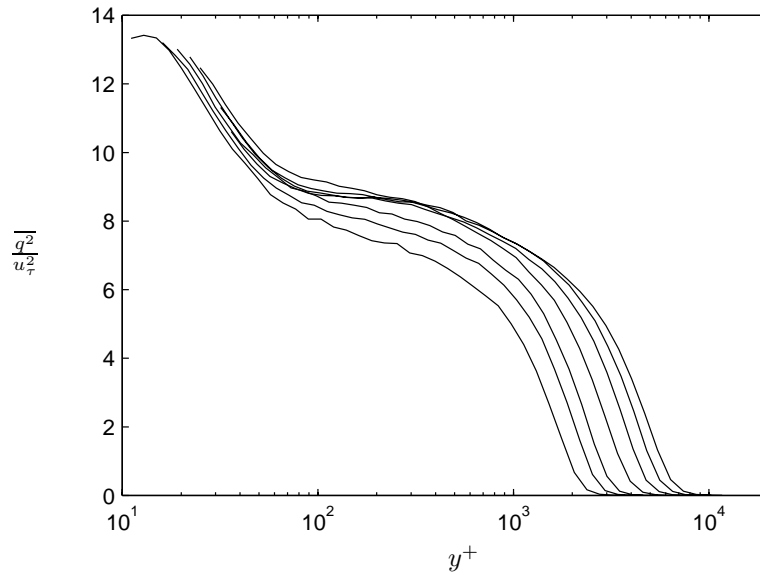
$$\dfrac{\overline{q^2}}{u_\tau^2}$$

FIGURE 18. Turbulent kinetic energy, $\overline{q^2} = \overline{u^2} + \overline{v^2} + \overline{w^2}$, in inner-law scaling.
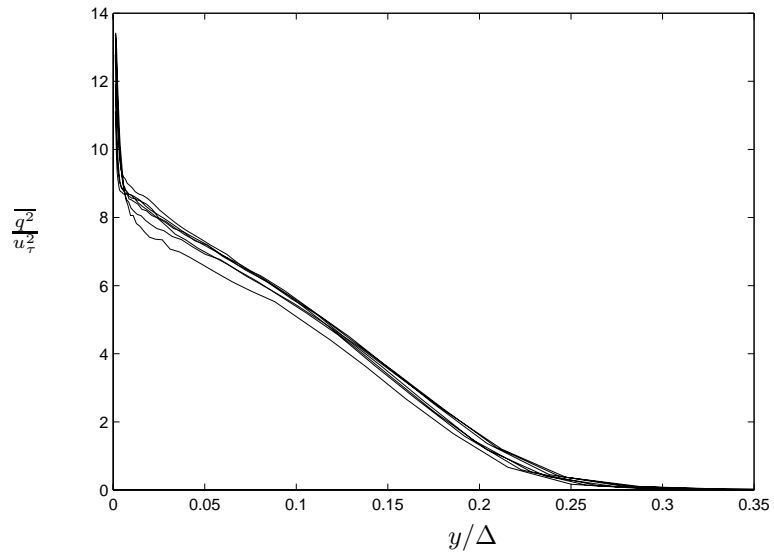
FIGURE 19. Turbulent kinetic energy, $\overline{q^2} = \overline{u^2} + \overline{v^2} + \overline{w^2}$, in outer-law scaling.
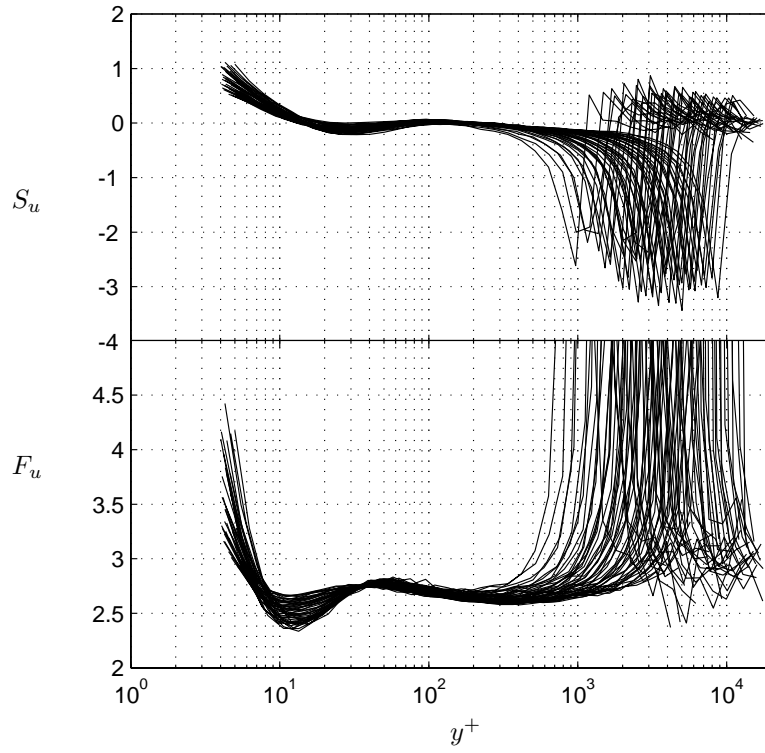
FIGURE 20. Profiles of skewness S_u and flatness F_u in inner-law scaling.
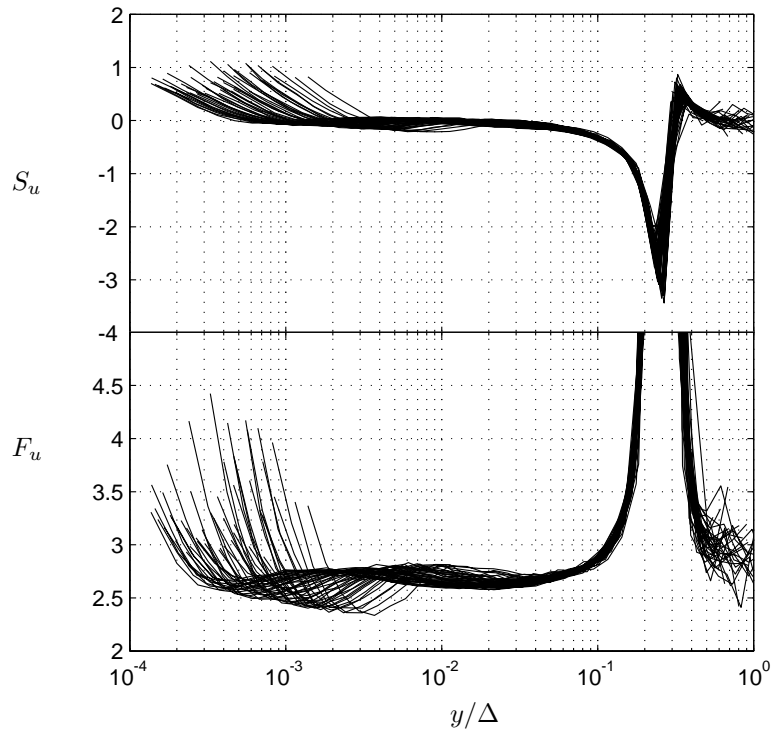
FIGURE 21. Profiles of skewness S_u and flatness F_u in outer-law scaling.
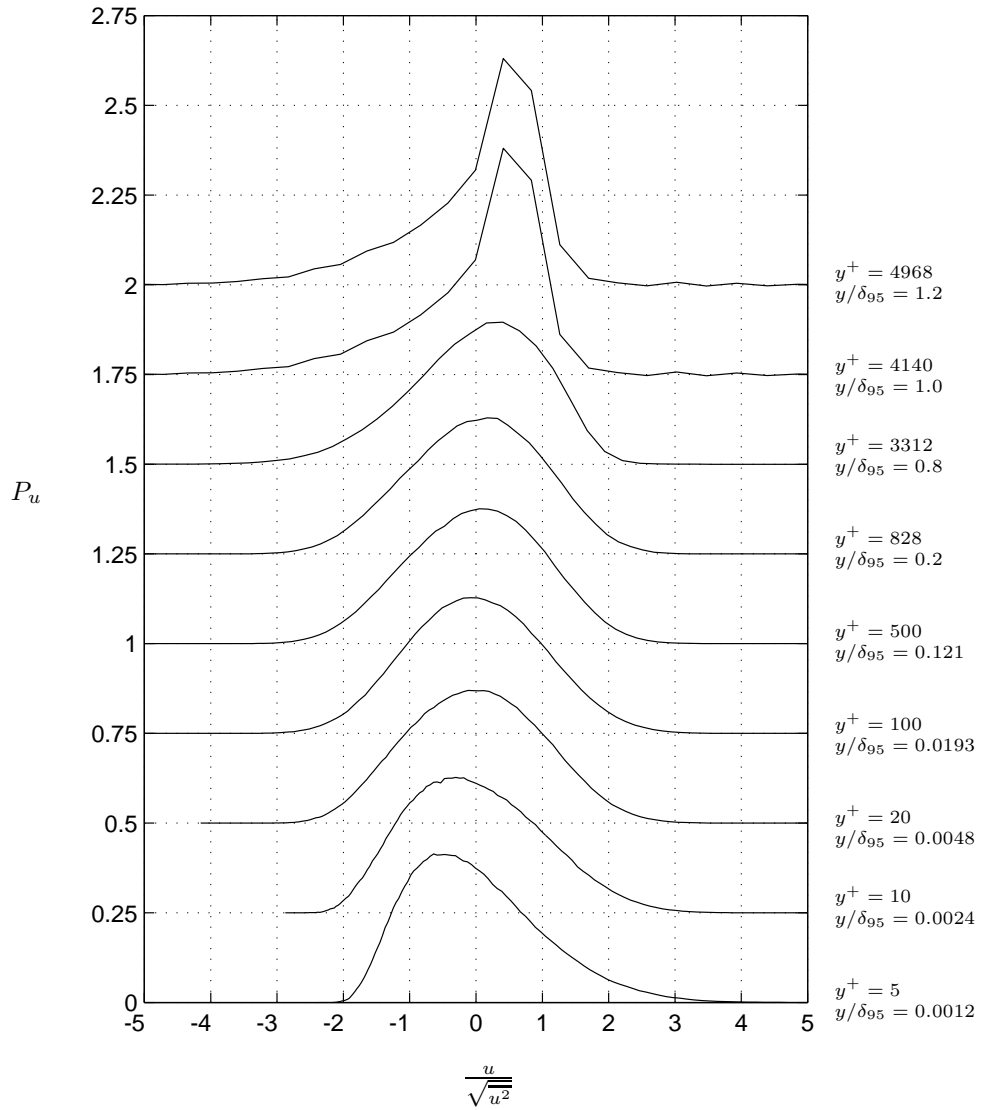
FIGURE 22. Probability density functions for the streamwise velocity at different distances from the wall. $Re_\theta = 17800$.
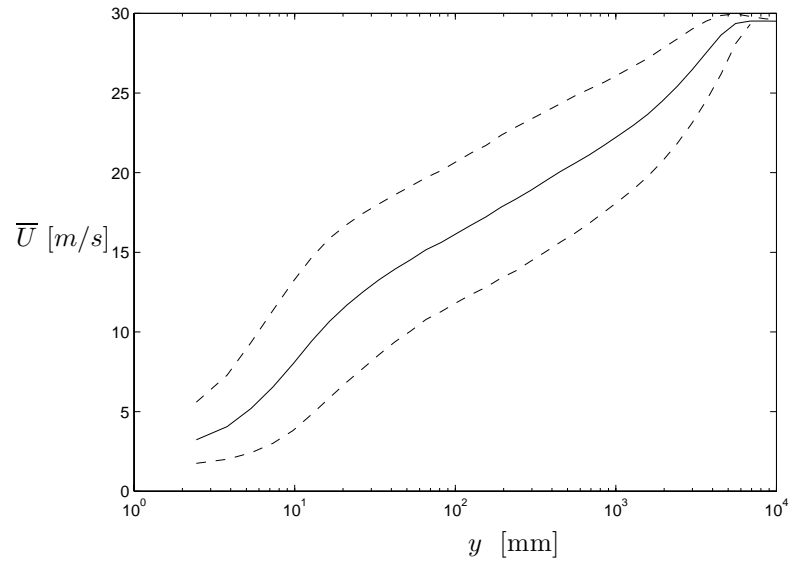
FIGURE 23. Example mean velocity profile. $Re_\theta = 17800$. Dashed line enclose 95% of the samples.
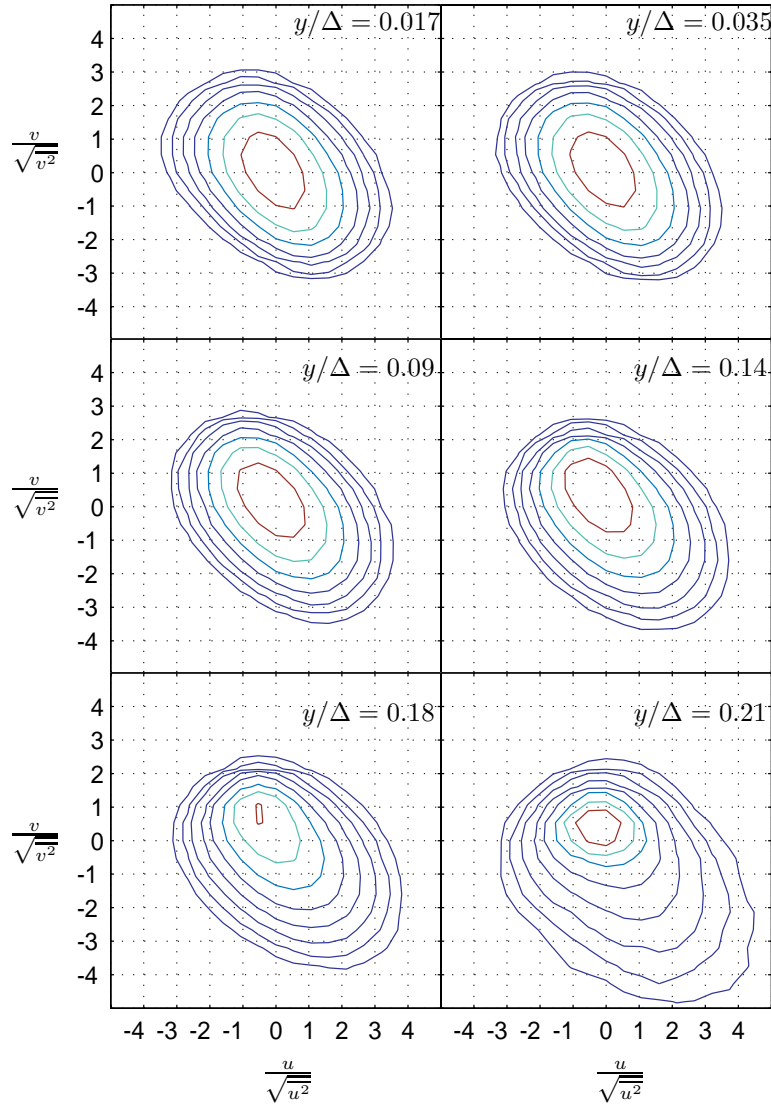
FIGURE 24. Joint-probability density functions P_{uv}, for the streamwise and wall-normal velocities at different outer-scaled distances from the wall. $Re_\theta = 26600$. Contours at ten levels with logarithmic spacing, *i.e.* $10^{\{-3, -2.66, -2.33, ..., 0\}}$.

8. Appendix: Measurements with a Parallel-Wire Probe

8.1. *Motivation*

The use of parallel-wire probes was initiated by the need for near-wall turbulence data at high Reynolds numbers where the turbulent scales are small and the gradients are large. A conventional X-wire probe have severe problems problems in the near wall region mainly due to its large wall-normal dimension compared to the mean and fluctuating velocity gradients. Efforts have been made to miniaturize X-wire probes by several investigators, *e.g.* Willmarth & Bogar (1977). Österlund (1995) found that thermal interaction between the heated wires in X-wire probes deteriorates the signal for Peclet numbers less than 50. The idea of parallel wires is instead to utilize the thermal interaction between the wires and calibrate the probe against the velocity and angle similarly to the procedure for X-wire probes. For this to work the parallel-wire probe must always be operated in the under critical region of its transfer function, as opposed to X-wire probes who must not have any thermal interaction. The result of this is that the wires have to be placed very closely together in order to achieve a reasonably high sensitivity and a flat response to high enough frequencies. The wall normal extent of the parallel-wire probe geometry is therefore only about 1/50 or less than that of an X-wire probe. The influence from high velocity gradients at the wall is therefore much smaller.

8.2. *Probe design and calibration*

The body of the probe was built of a ceramic tube, designed for use in thermo elements, with 4 holes. The prong material was spring steel. The conical shape of the prong tips was obtained in an etching process using a bath of nitric acid (60%) applying a small voltage to speed up the etching. The delicate positioning of the prongs was done under a microscope (80x) with micro manipulating equipment gearing down the hand movement. When the prongs are fixed in position a low viscosity epoxy resin is applied. The capillary force pulls the resin into the probe body and fixes the prongs in position after hardening. To fix the prongs together outside of the ceramic body a mixture of epoxy resin and colloidal silicon was applied. Before gluing the probe together the prongs were covered by a thin layer of solder to protect it from corrosion, also the solder is used later when the platinum wires are soldered onto the prong tips. The soldering is done by putting the etched piece of the Wollastone wire in position, by use of a micromanipulator, and then heating the prong with the soldering iron a few mm away until the solder melts. The diameter of the prong edge was about 20–30 μm. The wires were soldered on the inside of the prongs to make the distance between the wires as small as possible, see figure 25. Extreme care has to be taken when positioning the prongs to assure that the wires are parallel.
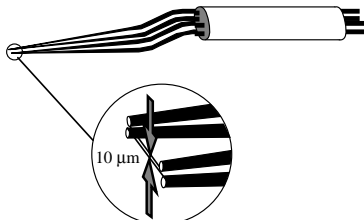
FIGURE 25. Schematic of a parallel-wire probe.

The probes were calibrated in the freestream outside of the boundary layer. The calibration of the parallel-wires was done by the same procedure used for the X-wire probes (see Paper 8). The voltages from the anemometers, the angle of attack and the speed in the freestream, measured by a pitot tube, were registered at typically 8 angles, between $-30°$ to $30°$, and 8 velocities, between 2–25 m/s.

8.3. *Parallel-wire results*

Results from measurements with the parallel-wire probes are shown in figures 26 to 29. The experimental parameters are summarized in table 1. The results for the moments of the streamwise velocity component u show good agreement with results from single wire measurements and are not reported here.

For the wall-normal Reynolds stress component $\overline{v^2}$ a reasonably good agreement with X-wire data and also DNS data by Spalart (1988) and LDV data by Karlsson & Johansson (1988) are shown in figure 26. When compared to the X-wire results it is clear that the parallel-wire probe gives accurate data much closer to the wall. In contrast to the positive results obtained for $\overline{v^2}$ the results for the Reynolds shear-stress component $\overline{uv}$ are less encouraging, as shown in figure 27. This behavior was explained by Österlund (1995) as a result of the phase shift between the u and v signals, obtained from the parallel-wire probe, as a result of finite wire separation. The solution to this problem is to reduce the wire separation even further, which is very difficult with conventional probe design techniques. The skewness and flatness factors for the wall normal velocity S_v, F_v are shown in figures 28, 29 and exhibit approximately the same results as obtained with an X-wire.

The severe difficulties with the design and construction of parallel-wires separated only a few μm was the main reason to discontinue the development of the parallel-wire probe in this study. Future MEMS technology may possess capacity to solve this problem.
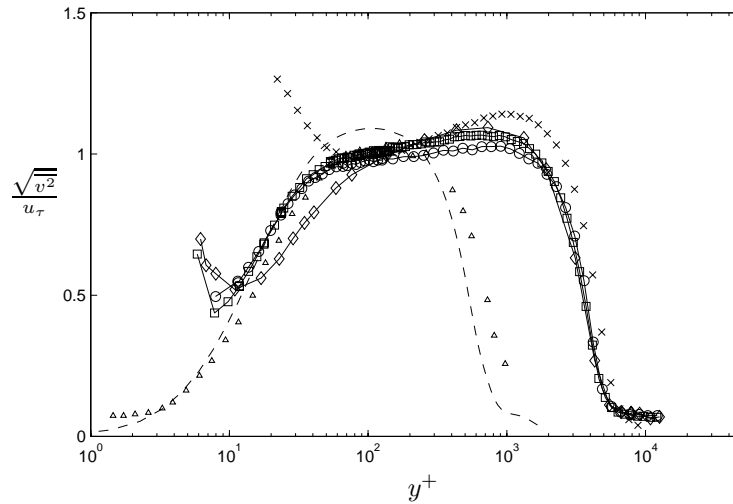
FIGURE 26. Wall normal Reynolds stress, from parallel-wire probe. For symbols, see table 1. $\times$: X-wire measurement, $Re_\theta = 15100$. $\triangle$: LDV Measurements in boundary layer flow at $Re_\theta = 2420$ by Karlsson & Johansson (1988). $--$: Boundary layer simulation at $Re_\theta = 1410$ by Spalart (1988).
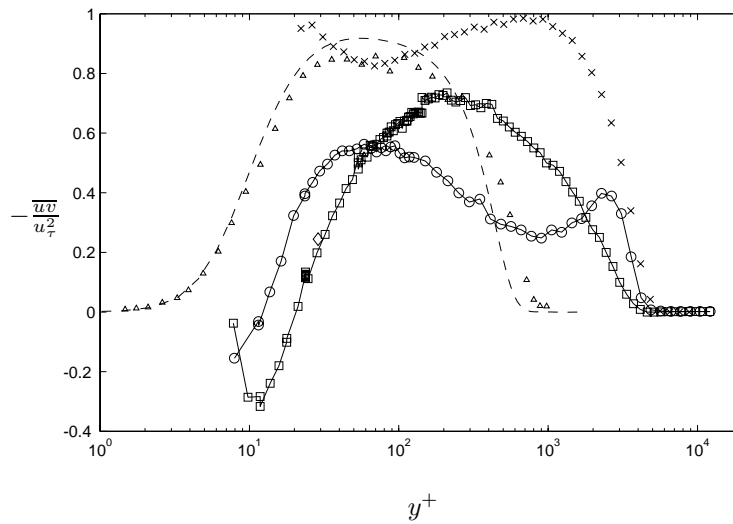
FIGURE 27. Reynolds shear stress from parallel-wire probe. For symbols, see table 1. $--$: Boundary layer simulation at $Re_\theta = 1410$ by Spalart (1988). $\times$: X-wire measurement, $Re_\theta = 15100$. $\triangle$: LDV Measurements in boundary layer flow at $Re_\theta = 2420$ by Karlsson & Johansson (1988).

J. M. Österlund & A. V. Johansson

Symbol		□	○	◇
d	[μm]	1.27	1.27	2.54
Δ_w	[μm]	12	5	20
l_1	[μm]	230	230	280
l_2	[μm]	270	270	360
R_{c_1}	[Ω]	16.4	16.5	5.4
R_{c_2}	[Ω]	20	19.9	6.4
x	[m]	4.5	4.5	4.5
U_∞	[m/s]	25.3	25.6	25.1
u_τ	[m/s]	0.894	0.905	0.892
Re_θ		13800	13900	13800
Δ_w^+		0.7	0.3	1.2
l^+		13.8	13.9	16.7
l/d		181	181	112

TABLE 1. Parallel-wire experiments

9. Acknowledgments
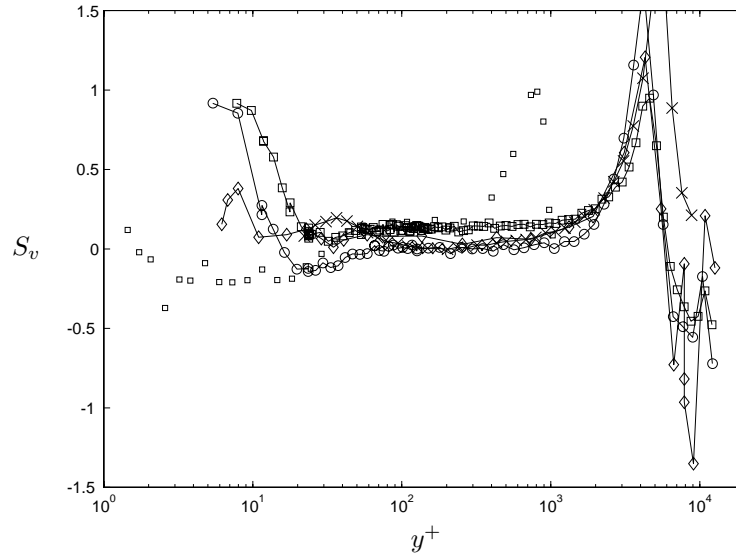
FIGURE 28. Skewness factor of the wall normal velocity, from parallel-wire probe. For symbols, see table 1. $\times$: X-wire measurement, $Re_\theta = 15100$. $\square$: LDV Measurements in boundary layer flow at $Re_\theta = 2420$ by Karlsson & Johansson (1988).

J. M. Österlund & A. V. Johansson
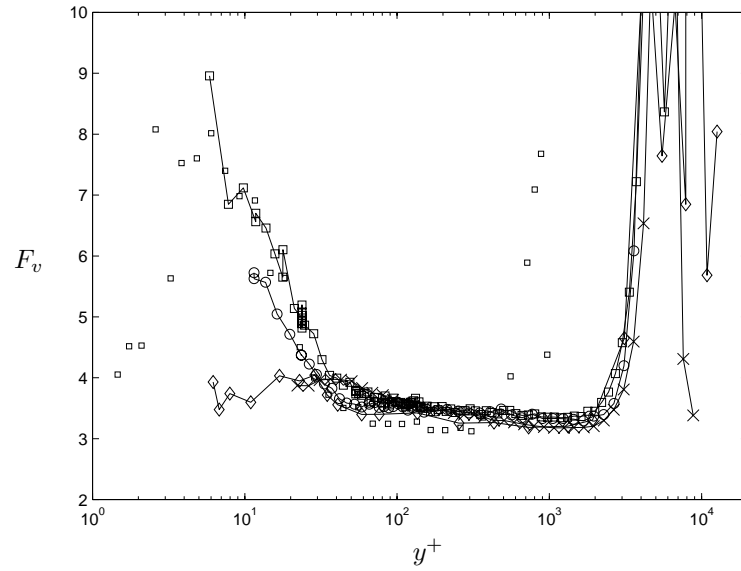
FIGURE 29. Flatness factor of the wall normal velocity, from parallel-wire probe. For symbols, see table 1. $\times$: X-wire measurement, $Re_\theta = 15100$. $\square$: LDV Measurements in boundary layer flow at $Re_\theta = 2420$ by Karlsson & Johansson (1988).

References

ALVELIUS, K. 1999 Studies of turbulence and its modeling through large eddy- and direct numerical simulation. PhD thesis, Department of Mechanics, Royal Institute of Technology, Stockholm.

COMTE-BELLOT, G. 1976 Hot-wire anemometry. *Ann. Rev. Fluid Mech.* **8**, 209–231.

FERNHOLZ, H. H. & FINLEY, P. J. 1996 The incompressible zero-pressure-gradient turbulent boundary layer: An assessment of the data. *Prog. Aerospace Sci.* **32**, 245–311.

FERNHOLZ, H. H., JANKE, G., SCHOBER, M., WAGNER, P. M. & WARNACK, D. 1996 New developments and applications of skin-friction measuring techniques. *Meas. Sci. Technol.* **7**, 1396–1409.

GAD-EL-HAK, M. & BANDYOPADHYAY, P. R. 1994 Reynolds number effects in wall-bounded turbulent flows. *Appl. Mech. Rev.* **47** (8), 307–365.

GRESKO, JR., L. S. 1988 Characteristics of wall pressure and near-wall velocity in a flat plate boundary layer. *Tech. Rep.* 88-2. Fluid Dynamics Research Laboratory Report.

HITES, M. H. 1997 Scaling of high-reynolds number turbulent boundary layers in the national diagnostic facility. PhD thesis, Illinois Institute of Technology.

JOHANSSON, A. V. 1992 A low speed wind-tunnel with extreme flow quality - design and tests. In *Prog. ICAS congress 1992*, pp. 1603–1611. ICAS-92-3.8.1.

JOHANSSON, A. V. & ALFREDSSON, P. H. 1982 On the structure of turbulent channel flow. *J. Fluid Mech.* **122**, 295–314.

JOHANSSON, A. V. & ALFREDSSON, P. H. 1983 Effects of imperfect spatial resolution on measurements of wall-bounded turbulent shear flows. *J. Fluid Mech.* **137**, 409–421.

KARLSSON, R. I. & JOHANSSON, T. G. 1988 Ldv measurements of higher order moments of velocity fluctuations in a turbulent boundary layer. In *Laser Anemometry in Fluid Mechanics*. Ladoan-Instituto Superior Tećnico, 1096 L.C., Portugal.

LIGRANI, P. M. & BRADSHAW, P. 1987 Spatial resolution and measurement of turbulence in the viscous sublayer using subminiature hot-wire probes. *Experiments in Fluids* **5**, 407–417.

MILLIKAN, C. B. 1938 A critical discussion of turbulent flows in channels and circular tubes. In *Proceedings of the Fifth International Congress of applied Mechanics*.

MOSER, R. D., KIM, J. & MANSOUR, N. N. 1999 Direct numerical simulation of turbulent channel flow up to $Re_\theta = 590$. *Phys. Fluids* **11** (4), 943–945.

ÖSTERLUND, J. M. 1995 Dynamic behavior of hot-wire probes in turbulent boundary layers. In *Advances in turbulence V* (ed. R. Benzi, (ed.)), pp. 398–402. Kluwer academic publishers.

ÖSTERLUND, J. M., JOHANSSON, A. V., NAGIB, H. M. & HITES, M. H. 1999 Wall shear stress measurements in high reynolds number boundary layers from two facilities. In *30th AIAA Fluid Dynamics Conference, Norfolk, VA*. AIAA paper 99-3814.

ROTTA, J. C. 1950 Über die Theorie der Turbulenten Grenzschichten. Mitt. M.P.I. Ström. Forschung Nr 1, also available as NACA TM 1344.

SKOTE, M., HENKES, R. & HENNINGSON, D. 1998 Direct numerical simulation of self-similar turbulent boundary layers in adverse pressure gradients. In *Flow, Turbulence and Combustion*, , vol. 60, pp. 47–85. Kluwer Academic Publishers.

SMITH, R. W. 1994 Effect of reynolds number on the structure of turbulent boundary layers. PhD thesis, Department of Mechanical and Aerospace Engineering, Princeton University, USA.

SPALART, P. R. 1988 Direct simulation of a turbulent boundary layer up to $Re_\theta = 1410$. *J. Fluid Mech.* **187**, 61–98.

WILLMARTH, W. W. & BOGAR, T. J. 1977 Survey and new measurements of turbulent structure near the wall. *Phys. Fluids* **20** (10), 9–21.

Paper 4

Measurements of skin-friction fluctuations in turbulent boundary layers with miniaturized wall-hot-wires and hot-films

By Sebastian Bake[1] & Jens M. Österlund[2]

[1]Hermann-Föttinger-Institut für Strömungsmechanik, Technische Universität Berlin, Straße des 17. Juni 135, 106 23 Berlin, Germany
[2]Department of Mechanics, KTH, SE-100 44 Stockholm, Sweden

Measurements of the fluctuating skin-friction are presented for turbulent boundary layers with zero pressure-gradient at high Reynolds numbers, using miniaturized wall-hot-wire and MEMS hot-film techniques. Results for quantities such as the turbulence intensity, skewness factor and flatness factor for the longitudinal skin-friction are presented and compared with findings from existing experiments. The experiments were carried out in the MTL-wind-tunnel at KTH in Stockholm and the LaWiKa wind-tunnel in Berlin at Reynolds numbers, based on momentum thickness θ, in the range $9800 < Re_\theta < 12400$.

1. Introduction

Detailed information about the fluctuating skin-friction is of basic importance for many types of flow and heat transfer problems and also for modeling purposes. A review of existing experiments were given by Alfredsson *et al.* (1988) and more recently on experimental techniques by Fernholz *et al.* (1996). The main difficulty is to design a skin-friction measurement technique with good dynamic response over the whole frequency range of interest and at the same time making the sensor size small enough to resolve the smallest scales in the turbulence. Most techniques such as the flush-mounted hot-film suffer from heat losses to the substrate which attenuates the response for high frequency fluctuations resulting in a difference between the static calibration and the dynamic response, e.g. a too low turbulence intensity

$$T_{\tau_w} = \frac{\sqrt{\overline{\tau_w^2}}}{\overline{\tau_w}} \tag{1}$$

is obtained.

The rapid development in the Micro-Electro-Mechanical-Systems (MEMS) area have resulted in new micro-machined hot-film sensors (Jiang *et al.* 1996)

	MTL	LaWiKa
test facility	flat plate	axisymmetric test section
length	7 m	6 m
width	1.2 m	$d = 0.41$m
temperature variations ΔT	< 0.05 °C	< 0.1 °C
free stream turbulence T_{U_∞}	0.02%	0.04%
max U_∞	69 m/s	34 m/s
probe position X	5.5 m	4.3 m

TABLE 1. Basic characteristics of the MTL and LaWiKa wind-tunnels in Stockholm and Berlin.

where the heat flux to the substrate is being reduced by placing the hot-film on a diaphragm on top of a vacuum cavity. Also the micro-machining technology allows for making very small hot-films to address the problem of spatial averaging.

Instead of using flush-mounted hot-films Alfredsson *et al.* (1988) used a hot-wire on the wall, that is elevated only a few μm from the wall to reduce the heat flux to the wall. This technique has been further developed by Fernholz *et al.* (1996) and a large effort has been put into the design and construction of miniaturized wall-hot-wire sensors for this type of experiment. The main purpose of this investigation is to determine statistical quantities of the skin-friction fluctuations in high Reynolds number turbulent boundary layers using current state-of-the-art hot-films and hot-wire-on-the-wall techniques.

2. The test facilities

Experimental results were obtained using two facilities, the MTL wind-tunnel at KTH and the LaWiKa wind tunnel at HFI. A brief description of the facilities and the experimental procedures are given below.

2.1. *The set-up at KTH*

Part of the experiments were carried out in the MTL-wind tunnel at the department of mechanics, KTH. The MTL-wind tunnel is specially designed to have good flow uniformity and low turbulence level. The temperature is controlled to within ± 0.05 °C. The test section is 7 m long with a cross sectional area of 1 m^2 (1.2×0.8m^2). The top and bottom walls are adjustable in order to control the the streamwise velocity distribution in the test section. Special care have been taken to reduce acoustic noise and most of the walls have acoustic treatment. The velocity can be controlled between 0-69 m/s. For an overview of the basic properties of the MTL wind-tunnel see table 1. For a detailed description of the characteristics of the MTL wind-tunnel see Johansson (1992).

The boundary layer plate is a sandwich construction of aluminum sheet and aluminum square tubes and is divided into 7 sections and an adjustable flap that extends into the first diffuser, giving a total length of the set-up of about 8.7 m. The first section has an elliptical nose ($AR = 5$) fixed at the leading edge. Two pressure taps in the elliptical nose are used to position the stagnation point at the centerline of the plate. The positioning of the stagnation point is done by the flap. The plate is mounted in the tunnel resting on two longitudinal beams. It is positioned in a horizontal plane. By adjusting the position of the top and bottom walls of the tunnel the pressure gradient is minimized. The streamwise variation of the freestream velocity was less than 0.15% of the freestream velocity at the leading edge of the plate. The measurement section of the plate was equipped with two circular inserts, for instrumentation and a traversing system.

The normal transition of the laminar boundary layer occurs at a position several meters from the leading edge. To fix the transition close to the leading edge a trip was introduced. The trip was selected to give transition at the trip in the velocity range used in these experiments, and consisted of 8 rows of Dymo brand embossing tape with the letter "V". The two-dimensionality of the boundary layer was checked by measuring the spanwise variation of the friction velocity u_τ, and it was found to be less than $\pm 0.7\%$.

The mean wall-shear stress was determined by oil-film interferometry, see Fernholz *et al.* (1996) and Paper 8. The oil-film results was used to fit a logarithmic skin-friction-law of the type

$$c_f = 2 \left[\frac{1}{\kappa} \ln(Re_\theta) + C \right]^{-2}, \tag{2}$$

with the resulting constants $\kappa = 0.384$ and $C = 4.08$. The skin friction variation was found to be in good agreement with other methods including the new near-wall method by Österlund and Johansson (Paper 8). The near-wall method utilizes direct measurement of the velocity profiles in the similarity region near the wall (the buffer region) but outside the region where hot-wire measurements in air are subjected to errors due to heat conduction to the wall. The profiles are then fitted to a universal profile obtained from DNS in the interval $6 < y^+ < 20$. Results from the oil-film interferometry are shown in figure 1 together with data from HFI and the skin friction correlation by Fernholz & Finley (1996).

The mean flow characteristics of the boundary layer showed a well defined logarithmic overlap region for Reynolds numbers (Re_θ) above 6000 and were reported in Österlund *et al.* (1999).

2.2. *The set-up at HFI*

The second part of the experiments was performed in the Laminar Wind Tunnel (LaWiKa) of the Hermann-Föttinger-Institute of Berlin Technical University. It is a closed-circuit tunnel with an axisymmetric test section made of Plexiglas
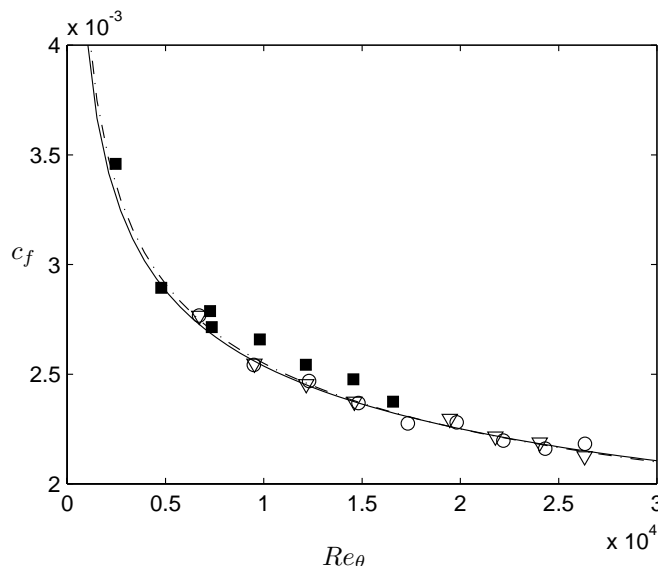
FIGURE 1. Skin-friction coefficient c_f. ∘ and ▽: KTH oil-film interferometry. —·—: best-fit of logarithmic friction law (equation 2) to the oil-film data. —: Skin-friction law from Fernholz & Finley (1996). ■: HFI Prestontube measurements.

tubes of various length with an inner diameter of 0.44 m and a total length of 6 m. It has a centrifugal fan and an additional blower to remove the nozzle boundary layer at the entry of the test section. To reduce the noise level in the wind tunnel the fan is mounted in a casing with sound attenuation. The bends are fitted with quarter circle turning vanes filled with mineral wool between perforated sheets. The test section has a sound muffler (quarter wave resonator) at the end to reduce the influence of fan-generated noise. In the settling chamber a non-woven filter mat and a single, precisely manufactured, perforated metal plate (64 % open area ratio) are used for damping of flow disturbances. The settling chamber is followed by a 2 m long axisymmetric nozzle with a 18:1 contraction ratio. The mean velocity distribution at the entry of the test section was uniform with a deviation from the mean < 1%. The flow temperature can be controlled with a water cooler. For an overview of the basic characteristics of the LaWiKa see table 1. For a further description of the flow quality see Fernholz & Warnack (1998). The boundary-layer under investigation starts at the elliptic leading edge of the test section and develops downstream on its inner wall. It was tripped by means of a Velcro tape with a height of 3 mm situated 0.24 m downstream the leading edge. Because of the axisymmetric shape of the test section no corner-flow effects occur.
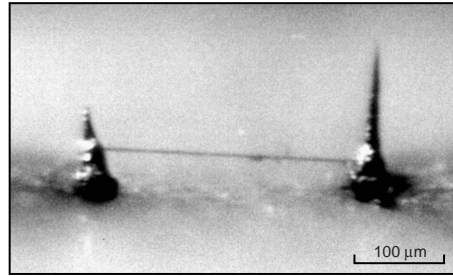
FIGURE 2. Photograph of a type 2 wall-hot-wire. Wire length 280μm, wire diameter 1.27μm and wire height above the wall 35μm.

For the probe insert a streamwise slot of 20 mm width was milled along one pipe section and filled with a series of interchangeable plugs. The Preston tubes, static taps and the wall hot-wires could be inserted in these plugs. For an optimal flush mounting the wall hot-wire probes were inserted under a microscope. The mean skin-friction values to calibrate the wall hot-wires were measured with Preston tubes (diameter between 1 and 2 mm) and are compared with the correlation by Fernholz & Finley (1996) in figure 1.

3. Sensor design

3.1. *Wall-hot-wires*

Three types of wall-hot-wire probe designs were used. The probe body of all types consists of a ceramic cylinder in a steel tube with 3 mm diameter. The ceramic isolates and holds the two prongs with the hot-wire. The first probe design was a wire elevated from the wall soldered onto two prongs with large separation. The wire ends were gold-plated to obtain a length to diameter ratio > 200 for the active part of the wire with a diameter of 2.5 μm.

The second type had prong tips thinned down to 35 μm and polished flush with the surface. The wire ends were fixed in two cones of solder plummet extending the prongs to the desired wire height, the active wire length now being the distance between the solder cones (see figure 2). The wires (diameter 1.27 and 0.64 μm) made of platinum-rhodium were not plated at the ends because of their mechanical infirmity.

The third and last type was designed like type two except that the wire was welded directly onto the prongs polished flush with the surface. This results in a slightly bent wire with an average height above the wall of only a few μm. This type was first used by Alfredsson *et al.* (1988).
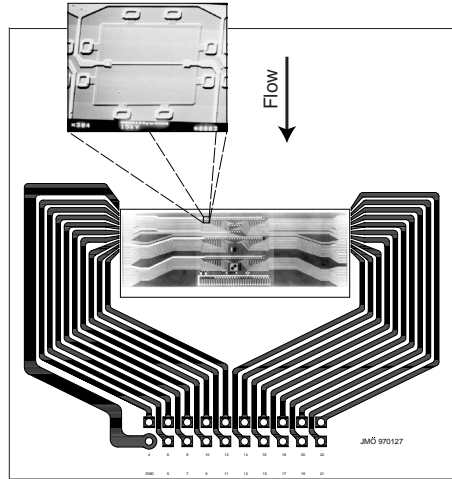
Figure 3. MEMS hot-film sensor chip from UCLA/Caltech
(Jiang *et al.* 1996), mounted in the center of a printed circuit
board providing the electrical connections. A blow-up of one
of the vacuum insulated hot-films is also shown.
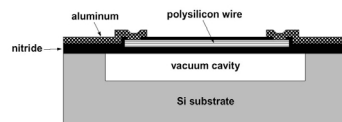
Figure 4. Cross-section, in a spanwise plane, of one hot-film
sensor (Jiang *et al.* 1996).

3.2. *MEMS hot-film*

The MEMS hot-film used in the experiments at KTH was designed by the
MEMS group at UCLA/Caltec (Jiang *et al.* 1996, 1997; Ho & Tai 1998). It
was flush-mounted with a printed circuit board for electrical connections which
in turn was flush-mounted into a Plexiglas plug fitting into the instrumenta-
tion insert of the measurement plate-section, see figure 3. The alignment was
ensured by using a microscope during the mounting of the sensor set-up. The
MEMS sensor chip was consisting of four rows of 25 sensors with a spanwise
separation of 300 μm. The length of the poly silicon hot-film is 150μm and
the width 3μm. It is placed on a 1.2μm thick silicon-nitride diaphragm with
dimensions 200μm $\times$ 200μm. Thermal insulation of the hot-film to the sub-
strate is provided by a 2μm deep vacuum cavity underneath the diaphragm,
see figure 4. In this experiment only one of the hot-films was used.

4. Experimental procedure

The wall-hot-wire and the hot-film was calibrated in the turbulent boundary layer against the mean skin-friction obtained using oil-film interferometry or Preston tubes, here denoted τ_w^*. A Kings law modified for near-wall effects (Fernholz *et al.* 1996) was used to relate the anemometer output voltage E and the skin-friction τ_w,

$$\tau_w = \left(\sqrt{u + \frac{k_1}{4} - k_2} - \frac{k_1}{2} \right)^2 ; \qquad u = (\frac{1}{B}(E^2 - A))^{1/n} \qquad (3)$$

where A, B, n, k_1 and k_2 are constants. The constants in equation 3 were determined minimizing the sum of the mean-square-error, for all calibration points, between the measured mean skin-friction τ_w^* and the mean value $\overline{\tau_w}$ obtained applying relation 3 to the anemometer voltage signal E

$$\min \left(\sum (\tau_w^* - \overline{\tau_w})^2 \right) . \qquad (4)$$

One example calibration is shown in figure 5. In the top half of the figure the measured mean skin-friction τ_w^* is shown against the mean anemometer voltages as circles. The stars represent the mean skin-friction values resulting from the calibration procedure of the wall-hot-wire or hot film. The dotted line is the resulting calibration function (equation 3), note that it does not need to go through the calibration circles since it is the sum of the squared distances between the stars and the circles that is minimized. In the bottom half of the figure the probability density for the anemometer voltage P_E is shown. The long tails of the probability density results in a required calibration interval for the mean skin-friction from 0.3 to 3 times the value of interest, to avoid extrapolation of the calibration function outside of the calibration limits (dashed lines in figure 5). No extrapolation was used.

5. Experimental results

An overview of the skin-friction experiments carried out in the MTL and LaWiKa wind-tunnels are compiled in table 2 where also symbols are introduced. The demand for a large calibration range restricts the investigation to essentially one Reynolds number for each set-up implying that no Reynolds number trends can be extracted from the present data.

In figure 6 results for the skin-friction intensity T_{τ_w} are presented, for all experiments performed in this investigation, against the active sensor length in viscous units. The data show a similar decrease in intensity for increasing probe dimensions as a result of spatial averaging (see *e.g.* Johansson & Alfredsson 1983; Ligrani & Bradshaw 1987). The limiting value of the turbulent intensity for small probe lengths is here found to be about 0.41. For comparison the
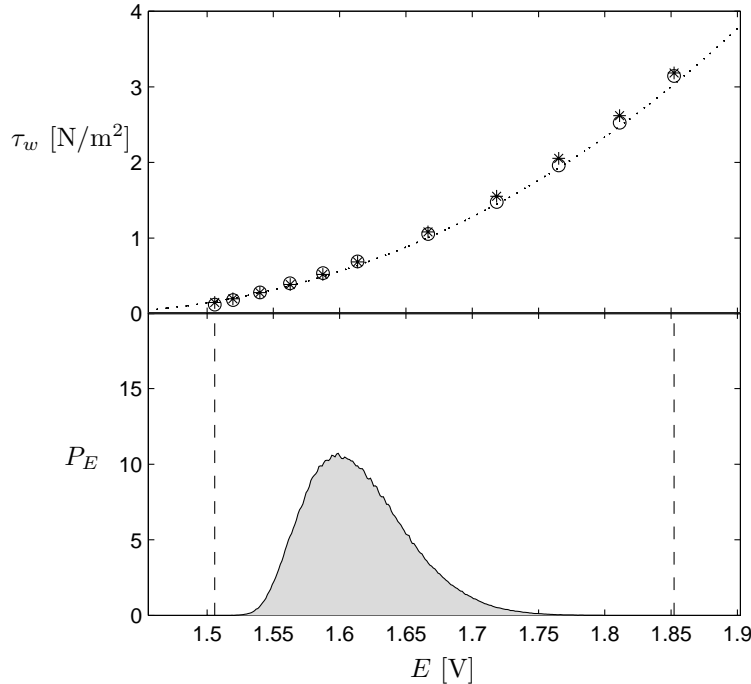
FIGURE 5. Calibration and measurement procedure. ∘: Mean skin-friction from oil-film or Preston tube. ⋯: The fitted relation between anemometer voltage and skin-friction, equation 3. ∗: Mean skin-friction from hot-wire/hot-film calculated from the anemometer voltage signal using relation 3. -: Probability density function for the anemometer voltage signal (at $\overline{E} = 1.61$ V and $\overline{\tau_w} = 0.69$N/m^2).

results from the wall-hot-wire experiments at MIT in a turbulent boundary layer in air flow by Alfredsson *et al.* (1988) are also shown in figure 6 and show good agreement with the present data.The resulting intensity from the MEMS hot-film of 0.35 is more than 10% too low and can probably be attributed to remaining heat losses in the diaphragm that modifies the dynamic response compared to the static one. Still, the result represents a major improvement compared to previous findings using hot-films in air where values of about 0.1 are reported for the relative intensity of the wall shear stress fluctuations. Also, the rapid development in MEMS technology will probably lead towards large improvements in the near future. The wall-hot-wire of type 3, with the wire welded onto prongs flush with the wall, show a behavior similar to the hot-film. The plausible explanation being that heat flux from the wire, which is only a few μm above the wall, is partly absorbed by the wall and transferred

Symbol	Probe type	Re_θ	d [μm]	l [μm]	l/d	h [μm]	l^+	h^+	Facility
○	WW1	12400	2.54	500	200	40	25	2	MTL
+	WW3	12400	1.27	200	160	5	10	0.25	MTL
×	MHF	12400	–	150	–	–	7.5	–	MTL
△	WW2	12400	1.27	200	160	35	12	1.2	MTL
●	WW1	9800	2.54	500	200	40	24	1.9	LaWiKa
▲	WW2	9800	1.27	200	160	40	10	1.9	LaWiKa
■	WW2	9800	1.27	280	220	35	13	1.7	LaWiKa
♦	WW2	9800	0.64	130	200	40	6.2	1.9	LaWiKa
▼	WW2	9800	0.64	140	220	40	6.7	1.9	LaWiKa

TABLE 2. Skin-friction measurements at KTH and HFI. WW: wall-hot-wire (number represents the type, see section 3.1). MHF: MEMS hot-film.
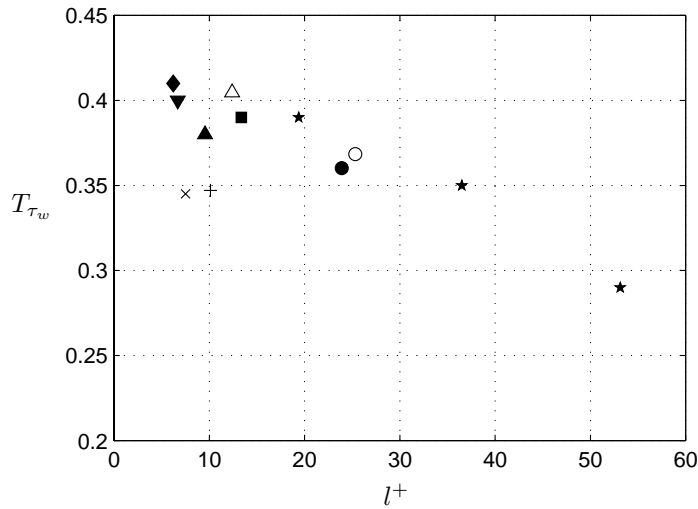
FIGURE 6. Turbulent skin friction intensity T_{τ_w}. For symbols, see table 2. $\star$: experiment by Alfredsson *et al.* (1988).

back to the fluid, in a mechanism similar to that for the hot-film. A connected issue is that the sensitivity of type 3 wall-hot-wires is very low due to damping resulting from the proximity of the wall.

Results for the Skewness and Flatness factors are presented in figure 7. No obvious trend, similar to the one found for the intensity, associated with the wire length is visible in the data and the values for the Skewness factor and
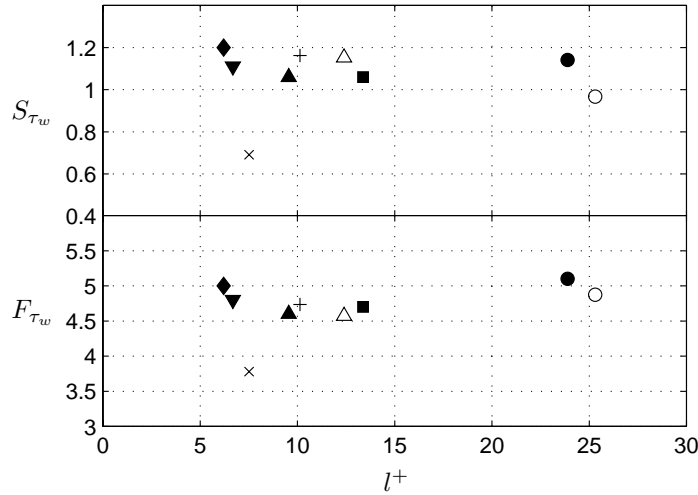
FIGURE 7. Skewness S_{τ_w} and Flatness F_{τ_w} factors for the fluctuating skin-friction. For symbols, see table 2.

for the Flatness factor are estimated as an average to be about 1.1 and 4.9, respectively. This is in good agreement with Alfredsson *et al.* (1988) who found the values 1.0 and 4.8.

6. Concluding Remarks

Based on the set of skin-friction measurements carried out using a variety of probe designs in two facilities it can be concluded that for Reynolds numbers of around 10,000 the streamwise fluctuating skin-friction intensity T_{τ_w} is close to 0.41. And that the values of the Skewness and Flatness factors are about 1.1 and 4.9, respectively.

The resulting skin-friction intensity from the MEMS type hot-film of 0.35 is a major improvement over existing types of hot-films with previously reported values of the fluctuating skin-friction intensity in air of about 0.1.The MEMS type hot-film and the wall-hot-wire of type 3, with the wire very close to the wall, both exhibits similar behavior and roughly 10% too low value for the fluctuating skin-friction intensity, it is believed to be a result of heat flux in the diaphragm, or in the wall-wire case heat flux to the wall, and back to the flow, resulting in a difference between static and dynamic responses.

7. Acknowledgments

References

ALFREDSSON, P. H., JOHANSSON, A. V., HARITONIDIS, J. H. & ECKELMANN, H. 1988 The fluctuation wall-shear stress and the velocity field in the viscous sublayer. *Phys. Fluids A* **31**, 1026–33.

FERNHOLZ, H. & WARNACK, D. 1998 The effect of a favourable pressure gradient and of the Reynolds number on an incompressible axissymmetric turbulent boundary layer. Part 1. The turbulent boundary layer. *J. Fluid Mech.* **359**, 329–356.

FERNHOLZ, H. H. & FINLEY, P. J. 1996 The incompressible zero-pressure-gradient turbulent boundary layer: An assessment of the data. *Prog. Aerospace Sci.* **32**, 245–311.

FERNHOLZ, H. H., JANKE, G., SCHOBER, M., WAGNER, P. M. & WARNACK, D. 1996 New developments and applications of skin-friction measuring techniques. *Meas. Sci. Technol.* **7**, 1396–1409.

HO, C.-M. & TAI, Y.-C. 1998 Micro-electro-mechanical-systems (MEMS) and fluid flows. *Ann. Rev. Fluid Mech.* **30**, 579–612.

JIANG, F., TAI, Y.-C., GUPTA, B., GOODMAN, R., TUNG, S., HUANG, J. B. & HO, C.-M. 1996 A surface-micromachined shear stress imager. In *1996 IEEE Micro Electro Mechanical Systems Workshop (MEMS '96)*, pp. 110–115.

JIANG, F., TAI, Y.-C., WALSH, K., TSAO, T., LEE, G. B. & HO, C.-H. 1997 A flexible mems technology and its first application to shear stress sensor skin. In *1997 IEEE Micro Electro Mechanical Systems Workshop (MEMS '97)*, pp. 465–470.

JOHANSSON, A. V. 1992 A low speed wind-tunnel with extreme flow quality - design and tests. In *Prog. ICAS congress 1992*, pp. 1603–1611. ICAS-92-3.8.1.

JOHANSSON, A. V. & ALFREDSSON, P. H. 1983 Effects of imperfect spatial resolution on measurements of wall-bounded turbulent shear flows. *J. Fluid Mech.* **137**, 409–421.

LIGRANI, P. M. & BRADSHAW, P. 1987 Spatial resolution and measurement of turbulence in the viscous sublayer using subminiature hot-wire probes. *Experiments in Fluids* **5**, 407–417.

ÖSTERLUND, J. M., JOHANSSON, A. V., NAGIB, H. M. & HITES, M. H. 1999 Wall shear stress measurements in high reynolds number boundary layers from two facilities. In *30th AIAA Fluid Dynamics Conference, Norfolk, VA*. AIAA paper 99-3814.

Paper 5

Dynamic behavior of hot-wire probes in turbulent boundary layers

By J.M. Österlund & A.V. Johansson

Department of Mechanics, Royal Institute of Technology 10044 Stockholm, Sweden

Hot-wire measurements in air of $\overline{uw}^+$ in the near wall region of a turbulent boundary layer at high Reynolds numbers indicate a thermal interaction for typical two-wire probes, such as X- and V-probes. In order to determine this interaction two infinitely long parallel wires have been studied numerically by solving the heat transfer equation. Computations give that for X- and V-probes a typical Péclet number based on wire separation should be larger than about 50 to keep thermal interaction at an acceptable level. On the other hand for the Parallel-probe the results indicate that the Péclet number should suitably be less than 10 to ensure good sensitivity and uniform response in the frequency range of interest.

1. Experiments

Experiments in a high Reynolds number turbulent boundary layer were carried out in the MTL-tunnel at KTH. The test section of the MTL-tunnel measures 1.2m × 0.8m × 7m. A 7 m long boundary layer plate has been constructed. It spans the entire width of the test section (1.2 m), has an elliptical leading edge and an adjustable flap. The use of miniaturized hot-wires is necessary for sufficient spatial resolution. We have developed the technique to build extremely small probes with the aid of a high accuracy micro-manipulator. The smallest probes built have wires of 0.6 μm diameter and about 0.1 mm length. A new X-wire probe where the wires are contained within a box of 100 μm side-length has also been built. A new type of probe where two wires are placed extremely close to each other have also been built (see fig. 1). The intention is to measure effects of varying temperature wake interaction from the two wires with varying flow angle. We have built such probes with a wire separation of about 10 μm. The aim is to replace the use of the necessarily rather large X-probes for near-wall measurements of the wall-normal velocity component.
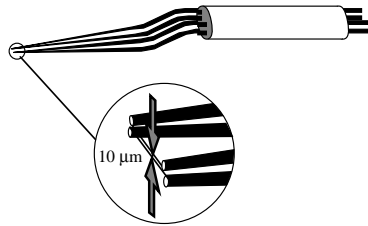
FIGURE 1. Parallel-probe.
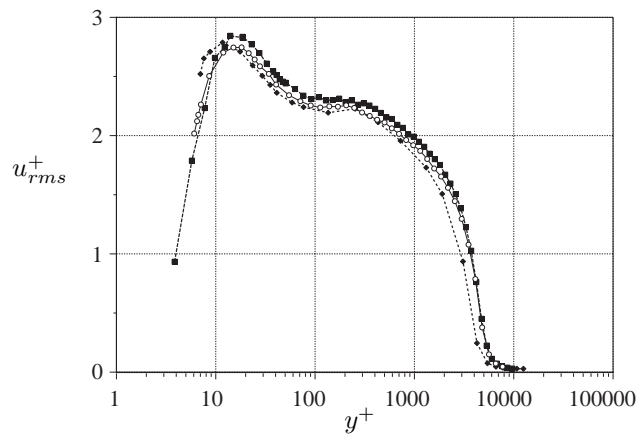
FIGURE 2. u_{rms}^+ profiles from single-probe, parallel-probe and x-probe. ∘: X-wire probe with box size 175μm, $Re_\theta = 14500$. ⋄: Parallel wire probe, $25\ \mu$m division, $Re_\theta = 7000$. □: Single-wire, $Re_\theta = 14500$.

2. Experimental results

A large number of measurement series with a variety of hot-wire probes have been carried out in the MTL tunnel for Reynolds numbers up to Re_θ=14 500. Near-wall measurements in the upper part of this range are unique to the present experiments and constitute a fundamentally very important area of basic turbulence knowledge that so far is lacking. The experiments carried out so far have been successful (using very small probes) in terms of measuring
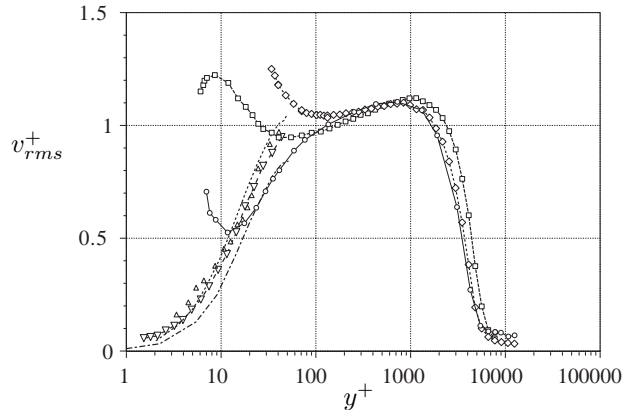
FIGURE 3. v_{rms}^+ profiles from parallel-probe and x-probe compared with data from measurements and simulations of channel and boundary layer flow. ○: Parallel-wire probe 25μm division, $Re_\theta = 7000$. ◇: X-wire probe boxsize 550 μm, $Re_\theta = 7000$. □: X-wire probe boxsize 175 μm, $Re_\theta = 14500$. Dashed line: DNS by Spalart (1988), $Re_\theta = 1410$. Dash-dotted line: DNS for channel flow by Kim *et al.* (1987). △: Measurements in oil channel by Kreplin & Eckelmann (1979). ▽: LDV measurements in boundary layer by Karlsson & Johansson (1988).

mean velocity and u_{rms} profiles and have shown consistency between measurements with single wire, X-wire and the new parallel wire probes (see figure 2). The results for v_{rms} are shown in figure 3 where data from a parallel wire probe and X-probes are compared (in the near wall region) with data from channel flow and boundary layer simulations. It is seen that all probes exhibit problems in the near wall region although the parallel wire probe seems to give the best results. The latter results appear to be reasonably accurate down to $y^+=15$. The large errors in the X-probe data in the near-wall region, motivated us to analyze the response of multi-wire probes in detail. The errors seen in figure 3 arise from interaction of the thermal wakes of the wires and becomes more accentuated with decreasing size of the probes. Also, the error in the Reynolds stress becomes worse for the parallel-wire probe. Corresponding problems were found in measurements with V-probes (for measurement of u and w). The calibration diagram of a V-probe superimposed with 400 data points (see fig 4) indicate an artificial correlation between u and w. Also the wide spread of the data points signifies an effect of the thermal wake interactions rather than truly large flow angles.
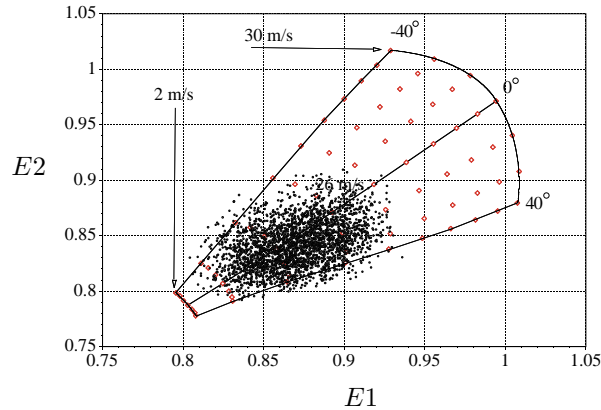
FIGURE 4. Calibration plot for the V-probe, superimposed with 4000 data samples taken at $y^+ = 6$, $U_\infty = 27$ m/s, $X = 5.5$ m, $Re_\theta = 14500$

3. Numerical simulation of Parallel-probe

An implicit algorithm for the two dimensional heat-transport equation has been implemented. An implicit algorithm would avoid most of the stability restrictions of an explicit scheme, but have the problem of achieving an efficient solution algorithm. The use of an operator splitting method (time-splitting) provides a way to get around this problem. By splitting each time-step into two half-steps where at each half step only terms associated with a particular coordinate direction are treated implicitly, only three implicit terms appear grouped on the main diagonal of the linear system. The efficient Thomas algorithm can be used to solve the system. Here a split formulation of the two-dimensional transport equation with a two-level Crank-Nicolson finite difference scheme is used on a rectangular grid. Constant temperature anemometry is simulated by forcing the temperature on the hot-wires to be constant. The fluctuating velocities in the turbulent boundary layer is simulated by a homogeneous velocity field, $\vec{v} = (U\cos\alpha, U\sin\alpha)$, $\alpha = \alpha_{max}\sin 2\pi ft$. The heat flux from the wires is calculated at each time-step. The thermal interaction, if any, gives a difference in heat flux between the two wires.

4. Results from numerical investigation of probe characteristics

Computations were carried out for the case described above with two point sources of heat separated by a distance of δ. This can either be regarded as an idealized model of a V-probe were the two wires have been idealized to point sources or as a more realistic model for a parallel-wire probe. A simple analysis
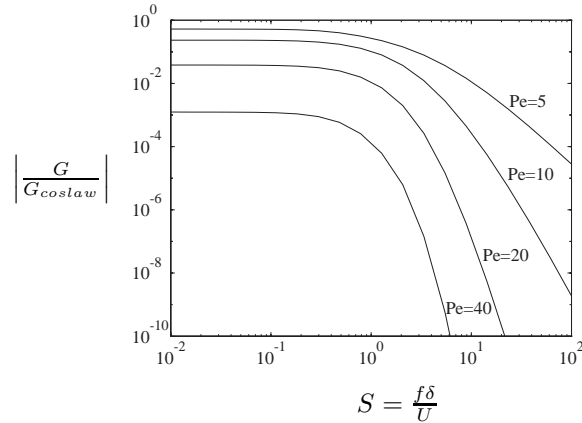
FIGURE 5. Amplitude of the transfer function G for the response in v velocity normalized with the response of an ideal X- or V-probe.

of the situation yields that the results should best be described in terms of Nusselt numbers for the two wires as functions of two parameters, viz. the Péclet number of the probe $Pe = \frac{U\delta}{\kappa}$ and the Strouhal number $S = \frac{f\delta}{U}$. The results of the computations are shown in figure 5 in terms of the maximum difference in Nusselt number between the two wires normalized with the corresponding difference for an ideal V-probe. This means that the curves can be interpreted as the sensitivity obtained with a parallel-wire probe normalized with that of an ideal V- (or X-) probe.

The phase shift of the parallel-probe (see fig 6) occurs at lower frequency than the decrease in magnitude. This indicates that correlations like $\overline{uv}$ may bee more sensitive to errors.

One may illustrate the above mentioned limitations by the situation in an airflow boundary layer at $y^+ = 3$ and a probe length L=0.2 mm. For a free stream velocity of 25 m/s the viscous length scale (at x=5 m) is roughly 0.015 mm (giving $L^+ \approx 13$). The Péclet number at this position becomes about 28. A Strouhal number of 0.1 here corresponds to 1.5 kHz, which indicates that problems are likely to occur in this case.

5. Conclusions

For X- and V-probes the computations indicate that thermal interaction between the wire-wakes deteriorate the results for Péclet numbers below 50. For parallel-wire probes on the other hand the results suggest that the Péclet number should suitably be less than 10. At a Pe of 5 the parallel wire has about 50 % of the sensitivity of an x or v-probe. It is also clearly seen from figure

J.M. Österlund & A.V. Johansson
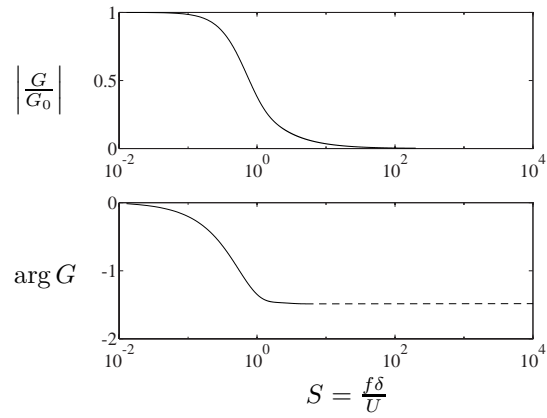
Figure 6. Frequency-response of parallel-probe normalized with response at zero frequency. Pe=10.

5 that a static calibration only is valid up to Strouhal numbers of about 0.1 ($f < 0.1\frac{U}{\delta}$).

References

GRESKO, JR., L. S. 1988 Characteristics of wall pressure and near-wall velocity in a flat plate boundary layer. *Tech. Rep.* 88-2. Fluid Dynamics Research Laboratory Report.

KARLSSON, R. I. & JOHANSSON, T. G. 1988 LDV measurements of higher order moments of velocity fluctuations in a turbulent boundary layer. In *Laser Anemometry in Fluid Mechanics*. Ladoan-Instituto Superior Tećnico, 1096 L.C., Portugal.

KIM, J., MOIN, P. & MOSER, R. 1987 Turbulence statistics in fully developed channel flow. *J. Fluid Mech.* **177**, 133–166.

KREPLIN, H.-P. & ECKELMANN, H. 1979 Behavior of the three fluctuating velocity components in the wall region of a turbulent channel flow. *Phys. Fluids* **22** (7).

SPALART, P. R. 1988 Direct simulation of a turbulent boundary layer up to $Re_\theta = 1410$. *J. Fluid Mech.* **187**, 61–98.

WILLMARTH, W. W. & BOGAR, T. J. 1977 Survey and new measurements of turbulent structure near the wall. *Phys. Fluids* **20** (10), 9–21.

Paper 6

Flow structures in zero pressure-gradient turbulent boundary layers.

By Jens M. Österlund, Björn Lindgren & Arne V. Johansson

Dept. of Mechanics, KTH, SE-100 44 Stockholm, Sweden

An experimental investigation on flow structures was performed in a high Reynolds number zero pressure-gradient turbulent boundary layer. Results are presented for the fluctuating wall-shear stress obtained simultaneously at two spanwise positions using a micro-machined hot-film sensor. Two-point correlations are presented and the mean streak spacing is evaluated from the two-point correlation of high-pass filtered wall-shear-stress signals. The streak spacing was found to be approximately $110\nu/u_\tau$ at the Reynolds number $Re_\theta = 9700$.

Experiments involving the simultaneous measurement of the wall-shear stress and the streamwise velocity component in an array of points in the streamwise-wall normal (x, y)-plane, directly above the hot-film, was also conducted. Results are presented for the conditionally averaged velocity field obtained by detecting turbulence generating events from the wall-shear stress, and two-point correlation measurements between the wall-shear stress and the streamwise velocity. Local propagation velocities and details of shear-layer structures are presented.

The scaling of the occurrence of VITA events in the buffer layer was investigated and a mixed time scale (*i.e.* the geometric mean of the inner and outer timescale) was found to give a satisfactory collapse of the data.

1. Introduction

The statistical, Reynolds averaged, description of turbulent boundary layers hides a wealth of structure-related phenomena and a quite intermittent character of *e.g.* turbulence production. This has been illustrated in flow visualizations, measurements and from DNS-generated data in a large number of papers, see *e.g.* the landmark paper of Kline *et al.* (1967), who showed that a significant part of the turbulence could be described in terms of deterministic events. These studies showed that in the close proximity of the wall the flow is characterized by elongated regions of low and high speed fluid of fairly regular spanwise spacing of about $\lambda^+ = 100$. Sequences of ordered motion occur randomly in space and time where the low-speed streaks begin to oscillate and to

suddenly break-up into a violent motion, a "burst". Kim *et al.* (1971) showed that the intermittent bursting process is closely related to shear-layer like flow structures in the buffer region, and also that roughly 70% of the total turbulence production was associated with the bursting process. The "bursts" were further investigated by Corino & Brodkey (1969) and it was found that two kinds of turbulence producing events are present. The ejection: involving rapid outflow of low speed fluid from the wall and sweeps: large scale motions originating in the outer region flowing down to the wall. Smith & Metzler (1983) investigated the characteristics of low-speed streaks using hydrogen bubble-flow and a high-speed video system. They found that the streak spacing increased with the distance from the wall. Furthermore, they found that the persistence of the streaks was one order of magnitude longer than the the observed bursting times associated with the wall region turbulence production.

To obtain quantitative data to describe the structures a reliable method to identify bursts with velocity or wall-shear stress measurements is needed. Conditional averaging using some triggering signal can be used to study individual events such as bursts or ejections and was first employed by Kovasznay *et al.* (1970). The triggering signal must be intermittent and closely associated with the event under study. Wallace *et al.* (1972) and Willmart & Lu (1972) introduced the *uv* quadrant splitting scheme. Blackwelder & Kaplan (1976) developed the VITA technique to form a localized measure of the turbulent kinetic energy and used it to detect shear-layer events. The detected events were studied using conditional averaging. Chen & Blackwelder (1978) added a slope condition to the VITA technique to detect only events corresponding to rapid acceleration. The behavior of the conditionally averaged streamwise velocity detected on strong accelerating events may be explained by tilted shear-layers that are convected past the sensor. Kreplin & Eckelmann (1979) measured the angle of the shear-layer front from the wall and found that nearest to the wall it was about 5°. At larger distances from the wall Head & Bandyopadhyay (1981) found the angle to be much steeper, about 45°. Gupta *et al.* (1971) investigated the spatial structure in the viscous sub-layer using an array of hot-wires distributed in the spanwise direction. They used a VITA correlation technique to determine the spanwise separations between streaks in the viscous-sub layer. The evolution of shear layers was studied by Johansson *et al.* (1987a) in the Göttingen oil channel by use of two-probe measurements in the buffer region of the turbulent channel flow. The bursting frequency in turbulent boundary layers was first investigated by Rao *et al.* (1971), their experiments indicated that outer scaling gave the best collapse of the data. Later, Blackwelder & Haritonidis (1983) carried out experiments on the bursting frequency in turbulent boundary layers. They found the non-dimensional bursting frequency was independent of Reynolds number when scaled with the inner time scale and found a strong effect of spatial averaging for sensors larger than 20 viscous

length scales. Alfredsson & Johansson (1984) studied the frequency of occurrence for bursts in turbulent channel flow, where they found the governing time scale to be a mixture (the geometric mean) of the inner and outer time scales. Johansson *et al.* (1991) analyzed near-wall flow structures obtained from direct numerical simulation of channel flow (Kim *et al.* 1987) using conditional sampling techniques. They also analyzed the space-time evolution of structures and asymmetry in the spanwise direction was found to be an important characteristic of near-wall structures, and for shear-layers in particular.

There seems to be no consensus on how to define a coherent structure and several definitions exist. In a review article on the subject Robinson (1991) defines a coherent structure as

> ... a three-dimensional region of the flow over which at least one fundamental flow variable (velocity component, density, temperature, etc.) exhibits significant correlation with itself or with another variable over a range of space and/or time that is significantly larger than the smallest local scales of the flow.

Other more restricted definitions are given by *e.g.* Hussain (1986) and Fiedler (1986). Here we will deal mainly with the streaks found in the viscous sublayer and the connected shear-layer type structures that are believed to be major contributors to the turbulence generation.

The majority of the experimental studies on structures in turbulent boundary layers have been conducted at low Reynolds numbers ($Re_\theta < 5000$), where flow visualization and high resolution velocity measurements are relatively easy to obtain. One of the objectives with this study was therefore to extend the knowledge about turbulence structures to high Reynolds numbers.

Three types of investigations were carried out. First, we investigate the mean streak spacing by measurements of the instantaneous wall-shear stress in two points with different spanwise separations. Secondly, the scaling of the "bursting frequency" was investigated by detection of the frequency of VITA events in the buffer region. Thirdly, a single wire probe was traversed in a streamwise wall-normal (x, y)-plane above the hot-film sensor, with the aim to detect and characterize shear-layer type events and to determine their local propagation velocity.

2. Experimental facility

The flow field of a zero pressure-gradient turbulent boundary layer was established on a seven meter long flat plate mounted in the test section of the MTL wind-tunnel at KTH. The MTL wind tunnel is of closed-return type designed with low disturbance level as the primary design goal. A brief description of the experimental set-up is given below. A more detailed description of the boundary layer experimental set-up can be found in paper 7.

After the test section the flow passes through diffusers and two 90° turns before the fan. A large fraction of the wind-tunnel return circuit is equipped with noise-absorbing walls to reduce acoustic noise. The flow quality of the MTL wind-tunnel was reported by Johansson (1992). For instance, the streamwise turbulence intensity was found to be less than 0.02%. The air temperature can be controlled to within ±0.05 °C, which is very important for this study since the primary measurement technique was hot-wire/hot-film anemometry, where a constant air temperature during the measurement is a key issue. The test section has a cross sectional area of 0.8 m × 1.2 m (height × width) and is 7 m long. The upper and lower walls of the test section can be moved to adjust the pressure distribution. The maximum variation in mean velocity distribution along the boundary layer plate was ±0.15%.

The plate is a sandwich construction of aluminum sheet metal and square tubes in seven sections plus one flap and one nose part, with the dimensions 1.2 m wide and 7 m long excluding the flap. The flap is 1.5 m long and is mounted in the following diffuser. This arrangement makes it possible to use the first 5.5 m of the plate for the experiment. One of the plate sections was equipped with two circular inserts, one for a plexiglas plug where the measurements were done, and one for the traversing system. The traversing system was fixed to the plate to minimize any vibrations and possible deflections. The distance to the wall from the probe was determined by a high magnification microscope. The absolute error in the determination of the wall distance was within ±5μm.

The boundary layer was tripped at the beginning of the plate and the two-dimensionality of the boundary layer was checked by measuring the spanwise variation of the wall shear stress τ_w. The maximum spanwise variation in friction velocity $u_\tau = \sqrt{\tau_w/\rho}$ was found to be less than ±0.7%.

The ambient conditions were monitored by the measurement computer during the experiments using an electronic barometer and thermometer (FCO 510 from Furness Ltd., UK). The reference conditions used in the calibration of the probes were determined using a Prandtl tube in the free-stream directly above the measurement station. The pressure and temperature were monitored at all times during the experiments using a differential pressure transducer and a thermometer connected directly to the measurement computer. The accuracy of the pressure measurement was 0.25 % and the accuracy of the temperature measurement was 0.02 °C.

Constant temperature hot-wire anemometry was used in all velocity measurements. All hot-wire probes were designed and built at the lab. Three sizes of single-wire probes were used in the experiments with wire diameters of: 2.5, 1.27 and 0.63 μm and a length to diameter ratio always larger than 200.

The MEMS hot-film (figure 1) used in the wall-shear stress measurements was designed by the MEMS group at UCLA/Caltec (Jiang *et al.* 1996, 1997; Ho & Tai 1998). It was flush-mounted with a printed circuit board for electrical
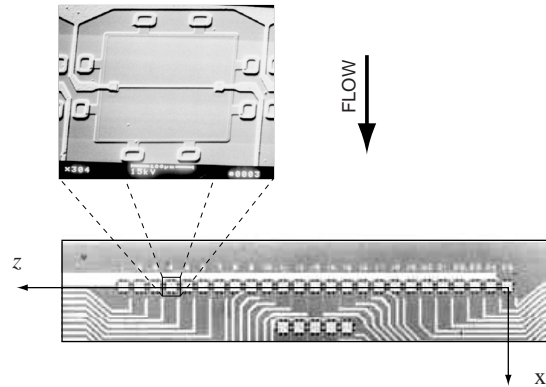
FIGURE 1. Enlargement of the MEMS hot-film sensor chip from UCLA/Caltech (Jiang *et al.* 1996) showing the array of 25 sensors used, seen as the row of white squares on the *z*-axis. A blow-up of one of the hot-films is also shown.

connections which in turn was flush-mounted into a Plexiglas plug fitting into the instrumentation insert of the measurement plate-section. Accurate alignment of the chip surface and the circuit board and the flat plate was achieved using a microscope during the mounting of the sensor set-up. The MEMS sensor chip has four rows of 25 sensors with a spanwise separation of 300 μm, see figure 1. The length of each hot-film is 150μm and the width 3μm. It is placed on a 1.2μm thick silicon-nitride diaphragm with dimensions 200μm $\times$ 200μm. Thermal insulation of the hot-film to the substrate is provided by a 2μm deep vacuum cavity underneath the diaphragm.

The anemometer system (AN1003 from AA lab systems, Israel) has a built-in signal conditioner and the signals from the anemometer were digitized using an A/D converter board (A2000 from National Instruments, USA) in the measurement computer. The A/D converter has 12 bit resolution and four channels which could be sampled simultaneously at rates up to 1 MHz divided by the number of channels used. The complete experiment was run from a program on the measurement computer which controlled the tunnel velocity, the positioning of probes, digitization of the anemometer signals, monitoring of the pressures and the temperature.

3. Experimental procedure

3.1. *Hot-wire calibration*

The hot-wires were calibrated in the free-stream against the velocity obtained from a Prandtl tube. First, the hot-wire probe was traversed well out of the

boundary layer, then the tunnel was run at ten different velocities ranging from about 5% to 100% of the free-stream velocity and the anemometer's voltage signal and the pressure from the Prandtl tube were recorded. A least-squares fit of the anemometer voltage versus the velocity was formed using Kings law. The calibration procedure was fully automated and the time required was about 15 min. due to the time required to allow the temperature to stabilize after changing the tunnel speed.

3.2. *Hot-film calibration*

The hot-films were calibrated *in-situ* in the turbulent boundary layer against the mean skin-friction obtained from oil-film interferometry, here denoted τ_w^*.

The principle of oil-film interferometry is to register the temporal deformation of a thin film of oil, due to the shear stress, from the flow, on its upper surface. From the deformation velocity the shear stress can be determined accurately, knowing the viscosity of the oil. The oil-film deformation velocity was determined by measuring the thickness of the oil-film by interferometry, see Fernholz *et al.* (1996). A least-squares fit of a variant of the logarithmic skin-friction law of the type

$$c_f = 2 \left[\frac{1}{\kappa} \ln(Re_\theta) + C \right]^{-2} \tag{1}$$

was made to the obtained wall-shear stress, with the resulting values of the constants $\kappa = 0.384$ and $C = 4.08$, see figure 2. Comparisons with other methods and also other experiments are made in Österlund *et al.* (1999), (see also papers 2 and 4). A detailed description of the method adapted is available in paper 7.

After the mean wall-shear stress relation was determined the anemometer voltage signals, from the two wall-shear stress sensors to be calibrated, were recorded for eight different mean wall-shear stress values in the range $0.3 < \tau_w^* < 3$ times the mean value of interest. This large range was necessary, due to the long tails of the probability density function for τ_w, to avoid extrapolation of the calibration function (2). Kings law was used to relate the anemometer output voltage E to the instantaneous skin-friction τ_w,

$$\tau_w = \left[\frac{1}{B}(E^2 - A) \right]^{1/n}, \tag{2}$$

where A, B and n are constants. The constants in equation 2 were determined minimizing the sum of the mean-square-error, for all calibration points, between the measured mean skin-friction, τ_w^*, and the mean value, $\overline{\tau_w}$, obtained applying relation 2 to the anemometer voltage signal E:

$$\min \left(\sum (\tau_w^* - \overline{\tau_w})^2 \right). \tag{3}$$

The MEMS hot-film was in Bake & Österlund (1999) (paper 4) found to give
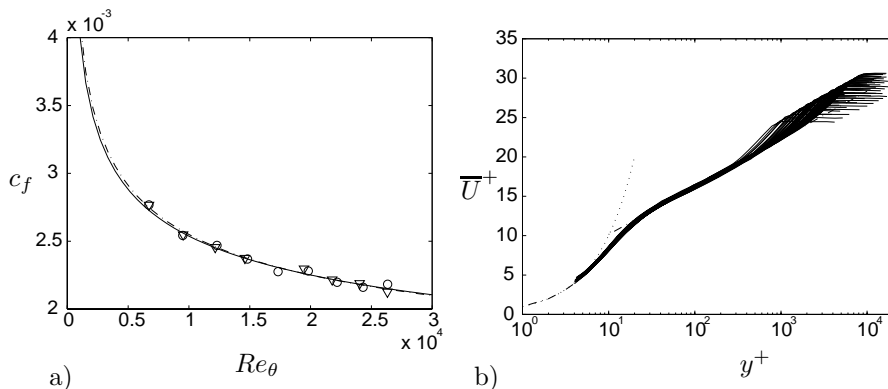
FIGURE 2. Mean flow characteristics of the boundary layer. $2530 < Re_\theta < 27300$. a) Skin-friction coefficient. $\circ$ and $\triangledown$: oil-film interferometry. $-\cdot-$: best-fit of logarithmic friction law (equation 1) to the oil-film data. $—$: Skin-friction law from Fernholz & Finley (1996). b) Mean velocity profiles shown in inner law scaling of the wall distance. Dashed curves represent $U^+ = y^+$ and $U^+ = \frac{1}{0.38} \ln y^+ + 4.1$

a relative fluctuation intensity of 0.35 (at $Re_\theta \approx 12400$), *i.e.* somewhat lower than the correct value of 0.41 (see Bake & Österlund 1999). This should not be of significant influence for the present correlation measurements.

3.3. *Mean Flow Characteristics*

Velocity profiles at five different streamwise positions ($x = 1.5, 2.5, \ldots 5.5$m) were taken over a large span in Reynolds number ($2530 < Re_\theta < 27300$), see figure 2. The behavior of the boundary layer was found to confirm the traditional two layer theory with a logarithmic overlap region for $200\nu/u_\tau < y < 0.15\delta_{95}$ existing for $Re_\theta > 6000$. The values of the von Kármán constant and the additive constants were found to be $\kappa = 0.38$, $B = 4.1$ and $B_1 = 3.6$ ($\delta = \delta_{95}$), see Österlund *et al.* (1999) and paper 2.

3.4. *Detection of events*

In the detection of shear layer structures the variable-interval time average (VITA) was used. The VITA of a fluctuating quantity $Q(x_i, t)$ is defined by

$$\widehat{Q}(x_i, t, T) = \frac{1}{T} \int_{t-\frac{1}{2}T}^{t+\frac{1}{2}T} Q(s)ds, \tag{4}$$

where T is the averaging time. The conventional time average results when T becomes large, *i.e.*

$$\overline{Q}(x_i) = \lim_{T \to \infty} \widehat{Q}(x_i, t, T).\tag{5}$$

Blackwelder & Kaplan (1976) used the VITA technique to form a localized measure of the turbulent energy

$$var(x_i, t, T) = \frac{1}{T} \int_{t-\frac{1}{2}T}^{t+\frac{1}{2}T} u^2(s)ds - \left(\frac{1}{T} \int_{t-\frac{1}{2}T}^{t+\frac{1}{2}T} u(s)ds \right)^2.\tag{6}$$

This quantity is also known as the short-time variance of the signal. The VITA variance can be used to detect shear-layer type events. An event is considered to occur when the amplitude of the VITA variance exceeds a certain threshold level. The correspondence between shear-layers and VITA events was substantiated by *e.g.* Johansson & Alfredsson (1982) and Johansson *et al.* (1987*b*). A detection function is defined as

$$D_u(t, T) = \begin{cases} 1 & var > k\overline{u^2} \\ 0 & \text{otherwise} \end{cases},\tag{7}$$

where k is the detection threshold level. A set of events $E_u = \{t_1, t_2, \ldots, t_N\}$ was formed from the midpoints of the peaks in the detection function D_u (N is the total number of detected events). Conditional averages of a quantity Q can then be constructed as

$$\langle Q(\tau) \rangle = \frac{1}{N} \sum_{j=1}^{N} Q(t_j + \tau),\tag{8}$$

where τ is the time relative to the detection time.

In addition to detecting events using the VITA variance technique, events were detected on the amplitude of the fluctuating quantity itself, *e.g.* detection of peaks of the fluctuating wall-shear stress,

$$D_{\tau_w}(t, T) = \begin{cases} 1 & \tau_w > k\sqrt{\overline{\tau_w^2}} \\ 0 & \text{otherwise} \end{cases},\tag{9}$$

where k is the threshold level.

4. Results

4.1. *Streak spacing*

The mean spanwise separation between low-speed streaks in the viscous sublayer was investigated using the MEMS array of hot-films, see figure 1. This set-up allowed for 18 different spanwise separations in the range $0 < \Delta z^+ < 210$. The spanwise length of the hot-films was $l^+ = 5.6$, at the Reynolds number $Re_\theta = 9500$ ($Re_\tau \equiv \delta_{95} u_\tau / \nu = 2300$). The spanwise cross correlation coefficient
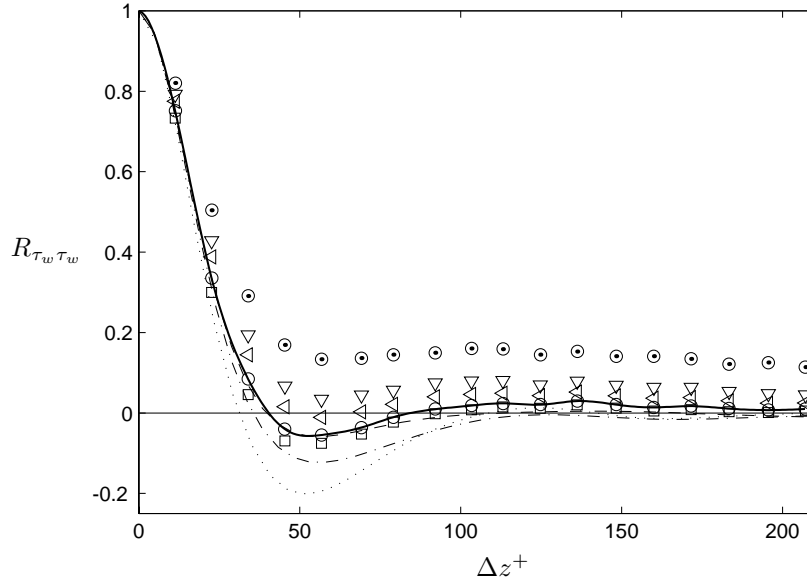
FIGURE 3. Spanwise correlation coefficient $R_{\tau_w \tau_w}$ as a function of Δz^+, $Re_\theta = 9500$ ($Re_\tau = 2300$). Present data, $\odot$: unfiltered, $\triangledown$: $f_c^+ = 1.3 \times 10^{-3}$, $\triangleleft$: $f_c^+ = 2.6 \times 10^{-3}$, $\circ$: $f_c^+ = 5.3 \times 10^{-3}$, $\square$: $f_c^+ = 7.9 \times 10^{-3}$, —: spline fit to $\circ$. DNS of channel flow, correlations of u at $y^+ = 5$, $--$: $Re_\tau = 590$, $-\cdot-$: $Re_\tau = 395$, $\cdots$: $Re_\tau = 180$ (Kim *et al.* 1987; Moser *et al.* 1999).

between the wall-shear stress signals obtained from two hot-films separated a distance Δz^+ in the spanwise direction is defined by

$$R_{\tau_w \tau_w}(\Delta z) = \frac{\overline{\tau_w(z)\tau_w(z + \Delta z)}}{\tau_w'^2}. \tag{10}$$

The prime denotes r.m.s value. The cross-correlation coefficient was used to estimate the mean streak spacing. At high Reynolds numbers contributions to the spanwise correlation coefficient from low frequency structures originating in the outer region conceals the contributions from the streaks and no clear (negative) minimum is visible in figure 3 for the measured correlation coefficient (shown as $\odot$). This behavior has also been found by others, see *e.g.* Gupta *et al.* (1971). A trend is clearly visible in the relatively low Reynolds number simulations by Kim *et al.* (1987) and Moser *et al.* (1999) where at their highest Reynolds number the minimum is less pronounced. In an attempt to reveal and possibly obtain the streak spacing also from the high Reynolds number data in

the present experiment we applied a high-pass (Chebyshev phase-preserving) digital filter to the wall-shear stress signals before calculating the correlation coefficient. This procedure emphasizes the contribution from the streaks and enhances the variation in the correlation coefficient. A variation of the cut-off frequency revealed no significant dependence of the position of the minimum on the cut-off. The cut-off frequency was chosen to damp out contributions from structures larger than about 2500 viscous length scales, or equivalently, larger than the boundary layer thickness. The filtered correlation is shown for different cut-off frequencies in figure 3. The correlation decreases rapidly and a broad minimum is found at $\Delta z^+ \approx 55$ indicating a mean streak spacing of $\lambda^+ \approx 110$. The correlation coefficient is close to zero for separations $\Delta z^+ > 100$. This result agrees well with other experiments and simulations at low Reynolds numbers, see *e.g.* Kline *et al.* (1967), Kreplin & Eckelmann (1979), Smith & Metzler (1983), Kim *et al.* (1987) and Moser *et al.* (1999). Gupta *et al.* (1971) also used a filtering technique to extract information about streak spacing from two-point correlations. They based their filtering on the VITA technique *i.e.* using short time averages. It is interesting to note that they found that the maximum averaging time for the VITA correlation to give consistent values of the streak spacing was $0.5\delta/U_\infty$. This corresponds well to the present findings regarding high-pass filtering cut-off frequencies.

4.2. *Propagation velocities*

The wall-normal space-time correlations of the wall-shear stress and the streamwise velocity were measured using one hot-film sensor and one hot-wire traversed in the (x, y)-plane. The time-shift of the peaks of the correlation coefficient,

$$R_{\tau_w u}(\Delta x, \Delta y, \Delta t) = \frac{\overline{\tau_w(x, y, t)u(x + \Delta x, y + \Delta y, t + \Delta t)}}{\tau_w' u'}, \tag{11}$$

for different Δx and Δy separations are shown in figure 4. The peak in the correlation moves to negative time-shifts for increasing wall distances, *i.e.* the structures are seen earlier away from the wall. This indicates a forward leaning structure. The propagation velocity of the structure at different distances from the wall is defined by the slopes

$$C_p^+ = \frac{\Delta x^+}{\Delta t^+} \tag{12}$$

of lines fitted to the time-shifts at constant wall-distance in figure 4. The resulting propagation velocity is plotted in figure 5 and was found to be constant ($C_p^+ \approx 13$) up to about $y^+ = 30$. Further out it was found to be close to the local mean velocity. This means that the structure becomes stretched by the mean shear above $y^+ = 30$. This can be seen also from the variation of the shear layer angle with wall distance, see figure 11.
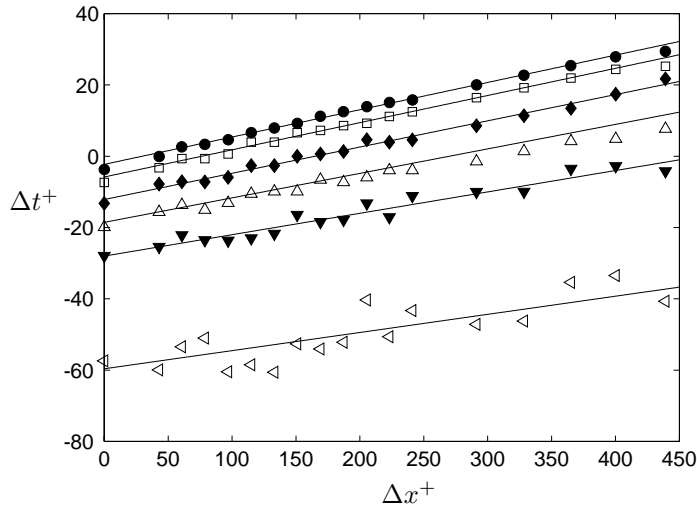
FIGURE 4. Time-shift of maximum correlation, $\max(R_{u\tau_w})$, at different wall distance. $\bullet$: $y^+ = 5$. $\square$: $y^+ = 10$. $\blacklozenge$: $y^+ = 20$. $\triangle$: $y^+ = 50$. $\blacktriangledown$: $y^+ = 100$. $\triangleleft$: $y^+ = 300$.
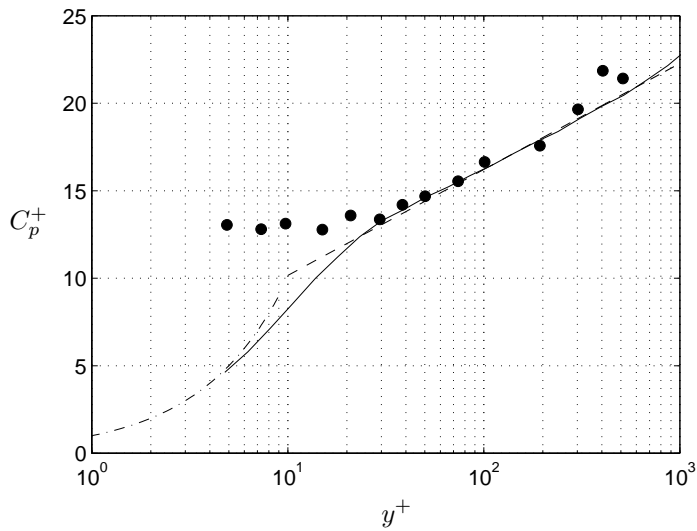
FIGURE 5. Propagation velocity C_p^+, $\bullet$. $--$: log-law, $\kappa = 0.38$ and $B = 4.1$. $-\cdot-$: linear profile. $—$: mean velocity profile. $Re_\theta = 9500$.

Symbol	Re_θ	l^+	y^+
$\triangle$	6700	6.6	14.3
∇	8200	8.2	13.8
$*$	9700	9.7	14.5
$+$	12600	12.8	14.8
$\circ$	15200	15.8	15.2

TABLE 1. Hot-wire experiments used for VITA detection in the buffer layer.

4.3. *Shear-layer events*

Shear-layer events were detected from peaks in the short time variance as described in section 3.4 using the velocity signal from a hot-wire in the buffer layer. In table 1 an overview is given of the hot-wire measurements used for VITA detection. An example of the fluctuating velocity signal (top), the corresponding short time variance (center), and the detection function (bottom) are shown in figure 6. The detection times are taken as the midpoints of the peaks of the detection function. The events are further sorted on the derivative of the velocity signal into accelerating and decelerating events, and an ensemble average is formed for each type according to equation 8. The accelerating events dominate in number over the decelerating events, and correspond to a forward leaning shear layer structure. In figure 7 the conditionally averaged streamwise velocity signal in the buffer region ($y^+ \approx 15$) is shown and strong accelerated and decelerated shear-layer events can be clearly seen.

Alfredsson & Johansson (1984) investigated the scaling laws for turbulent channel flows and found that the governing timescale for the near-wall region was a mixture of the inner and outer time scales

$$t_{\mathrm{m}} = \sqrt{t_* t_o}. \tag{13}$$

The frequency of occurrence of the VITA events is shown in figure 8 against the averaging time for outer, mixed and inner scaling. The mixed scaling appears relatively satisfactory also for the boundary layer flow. For very small averaging times one should keep in mind the non-negligible influence of finite probe size for the highest Reynolds numbers, see table 1. Blackwelder & Haritonidis (1983) reported inner scaling for the 'bursting frequency' obtained by the VITA technique. However, their values for the friction velocities (obtained from the near-wall linear profile) deviate substantially from the present correlation for c_f and their mean velocity profiles for different Reynolds numbers show a wide spread in the log-region.
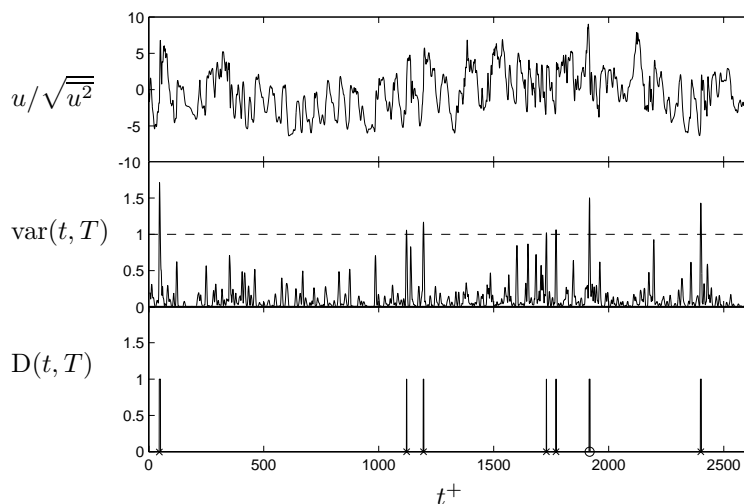
FIGURE 6. a) Time series for the streamwise fluctuating velocity component u. $y^+ = 14.5$ and $Re_\theta = 9700$. b) Short time variance of u with integrating window $T^+ = 10$. c) Detection function for $k = 1.0$. $\times$: Represents accelerating events and $\circ$: represents decelerating events.

4.4. *Wall-shear stress events*

The wall shear stress signal is highly intermittent (flatness factor ≈ 4.9) and peaks in the wall-shear stress was used to detect events. In figure 9 the conditionally averaged wall-shear stress events are shown sorted into positive and negative peaks using different detection threshold levels $k = \{-1, -0.75, -0.5, 1, 2, 3\}$. Broad peaks are seen that are largely symmetric. The negative events are slightly wider and less pointed as compared to the positive events.

Detection on peaks in the wall-shear stress was used to form conditional averages for the streamwise velocity obtained at a wall-normal separation Δy^+. Conditional averages for the streamwise velocity are shown in figure 10 for different wall-normal separations above the hot-film used as detector. For increasing wall-distance the conditionally averaged velocity is shifted towards negative times indicating a forward leaning structure. In figure 11 the data in figure 10 are replotted into lines of constant disturbance velocity (normalized with the local r.m.s.-level) in the (x, y)-plane using the measured propagation velocities (figure 5) to transform the time to an x-coordinate. An elongated and forward leaning high-velocity structure is visible above the high wall-shear event detected at $x = 0$. The peaks of the conditionally averaged velocity in
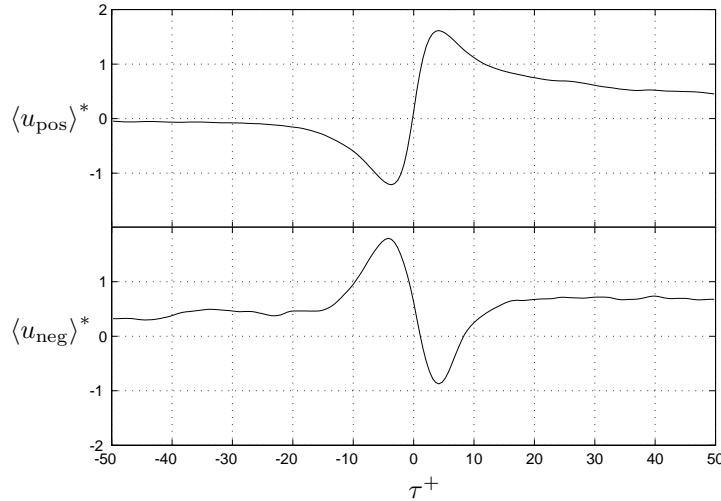
FIGURE 7. Conditional average of u for events with positive slope (top) and negative slope (bottom). $T^+ = 10$, $k = 1.0$ and $Re_\theta = 9700$

figure 10 are shown as black circles and agree well with a shear layer angle of about $20°$ found in many investigations, see *e.g.* Johansson *et al.* (1987*a*).

5. Conclusions

A micro machined hot-film sensor array was used together with a hot-wire probe in series of measurements of coherent structures in turbulent boundary layers. The small dimensions of the hot-films was a necessity for these measurements and the spatial resolution satisfactorily high to determine *e.g* the streak spacing.

A new high-pass correlation technique was used to determine the mean streak spacing for a high Reynolds number turbulent boundary layer. The mean streak spacing was found to be $\lambda^+ \approx 110$ which is very close to previous findings in low Reynolds number flow.

The propagation velocity of disturbances in the boundary layer is constant to $13u_\tau$ up to $y^+ = 30$, further out it was found to be close to the local mean velocity.

It was found that the frequency of occurrence of VITA events in the buffer region approximately conforms, to a mixed scaling behavior.
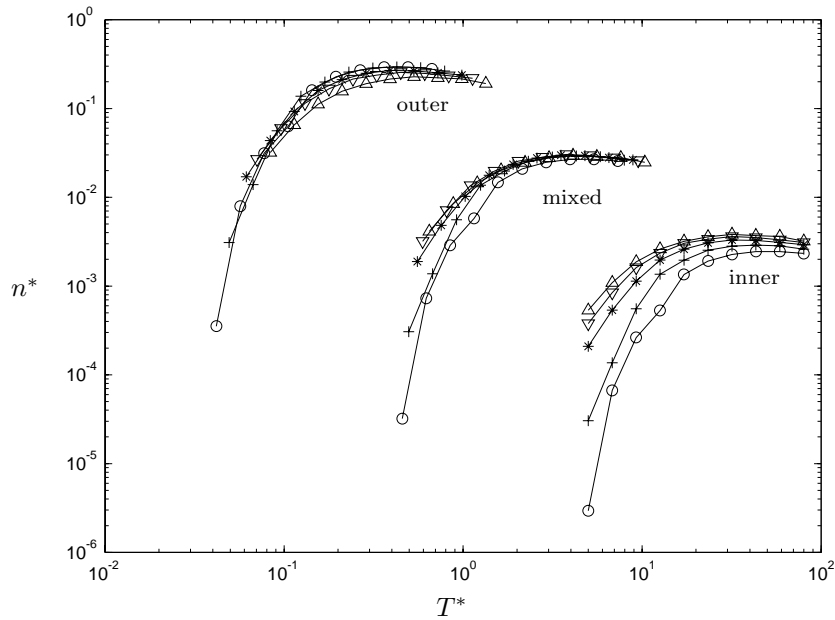
FIGURE 8. Frequency of occurrence of VITA events (k=1) as a function of the averaging time with outer, mixed and inner scaling (* denotes nondimensional quantities). $y^+ = 15$, $k = 1.0$. For symbols see table 1.

6. Acknowledgments
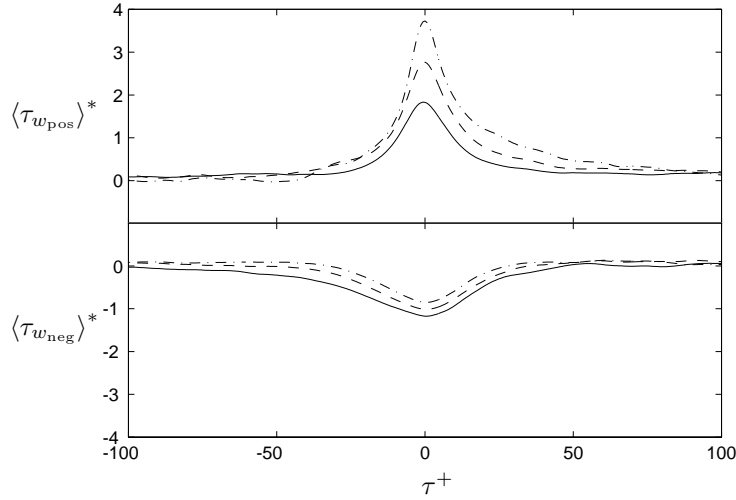
FIGURE 9. Conditional average of τ_w detecting on positive peaks (top) and detecting on negative peaks (bottom). Positive peaks, detection levels, $- \cdot -$: $k = 3$, $--$: $k = 2$, $-$: $k = 1$. Negative peaks, detection levels, $- \cdot -$: $k = -0.5$, $--$: $k = -0.75$, $-$: $k = -1$. $Re_\theta = 9700$.
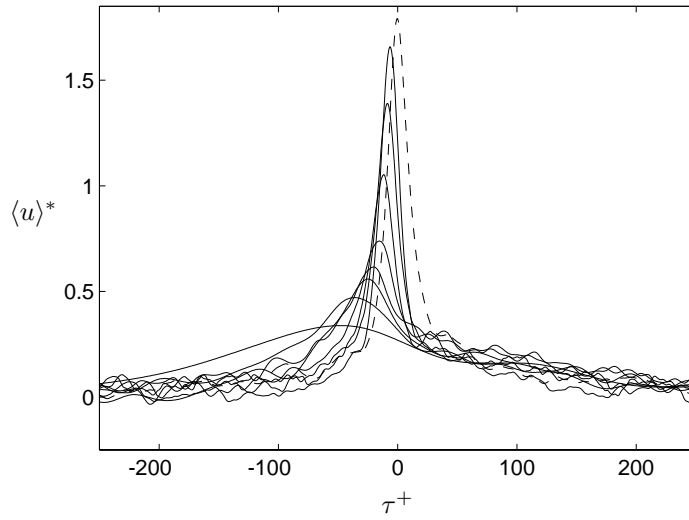
FIGURE 10. Conditionally averaged streamwise velocity. Detection of events where $\tau_w > k\tau_{w_{r.m.s.}}$. $\Delta x = 0$. $y^+ = \{5.7, 9.6, 16.6, 29.2, 51.7, 92.1, 164, 294\}$. Dashed line is the detection signal $\langle \tau_w \rangle^*$ $(k = 1)$.
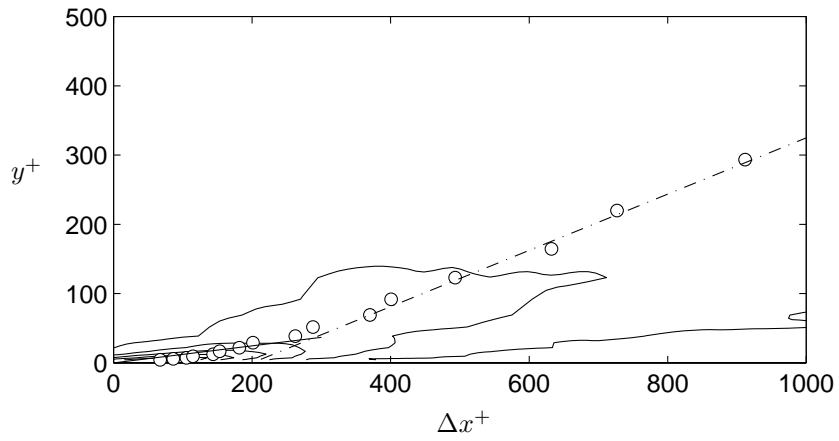
FIGURE 11. Conditionally averaged streamwise velocity. Detection of events where $\tau_w > k\tau_{w_{r.m.s.}}$. $k = 1$. ○: locations of maximum correlation. $-$: slope $7°$. $-\cdot-$: slope $18°$.

References

ALFREDSSON, P. H. & JOHANSSON 1984 Time scales in turbulent channel flow. *Phys. Fluids A* **27** (8), 1974–81.

BAKE, S. & ÖSTERLUND, J. M. 1999 Measurements of skin-friction fluctuations in turbulent boundary layers with miniaturized wall-hot-wires and hot-films. Submitted for publication in *Phys. of Fluids.*

BLACKWELDER, R. F. & HARITONIDIS, J. H. 1983 The bursting frequency in turbulent boundary layers. *J. Fluid Mech.* **132**, 87–103.

BLACKWELDER, R. F. & KAPLAN, R. E. 1976 On the wall structure of the turbulent boundary layer. *J. Fluid Mech.* **76**, 89–112.

CHEN, K. K. & BLACKWELDER, R. F. 1978 Large-scale motion in a turbulent boundary layer. *J. Fluid Mech.* **89**, 1–31.

CORINO, E. R. & BRODKEY, R. S. 1969 A visual investigation of the wall region turbulent flow. *J. Fluid Mech.* **37**, 1–30.

FERNHOLZ, H. H. & FINLEY, P. J. 1996 The incompressible zero-pressure-gradient turbulent boundary layer: An assessment of the data. *Prog. Aerospace Sci.* **32**, 245–311.

FERNHOLZ, H. H., JANKE, G., SCHOBER, M., WAGNER, P. M. & WARNACK, D. 1996 New developments and applications of skin-friction measuring techniques. *Meas. Sci. Technol.* **7**, 1396–1409.

FIEDLER, H. E. 1986 Coherent structures. In *Advances in turbulence*, , vol. 32, pp. 320–336. Berlin: Springer-Verlag.

GUPTA, A. K., LAUFER, J. & KAPLAN, R. E. 1971 Spatial structure in the viscous sublayer. *J. Fluid Mech.* **50**, 493–512.

HEAD, M. R. & BANDYOPADHYAY, P. 1981 New aspects of turbulent boundary layer structure. *J. Fluid Mech.* **107**, 297–338.

HO, C.-M. & TAI, Y.-C. 1998 Micro-electro-mechanical-systems (MEMS) and fluid flows. *Ann. Rev. Fluid Mech.* **30**, 579–612.

HUSSAIN, A. K. M. F. 1986 Coherent structures and turbulence. *J. Fluid Mech.* **173**, 303–56.

JIANG, F., TAI, Y.-C., GUPTA, B., GOODMAN, R., TUNG, S., HUANG, J. B. & HO, C.-M. 1996 A surface-micromachined shear stress imager. In *1996 IEEE Micro Electro Mechanical Systems Workshop (MEMS '96)*, pp. 110–115.

Jiang, F., Tai, Y.-C., Walsh, K., Tsao, T., Lee, G. B. & Ho, C.-H. 1997 A flexible mems technology and its first application to shear stress sensor skin. In *1997 IEEE Micro Electro Mechanical Systems Workshop (MEMS '97)*, pp. 465–470.

Johansson, A. V. 1992 A low speed wind-tunnel with extreme flow quality - design and tests. In *Prog. ICAS congress 1992*, pp. 1603–1611. ICAS-92-3.8.1.

Johansson, A. V. & Alfredsson, P. H. 1982 On the structure of turbulent channel flow. *J. Fluid Mech.* **122**, 295–314.

Johansson, A. V., Alfredsson, P. H. & Eckelmann, H. 1987*a* On the evolution of shear layer structures in near wall turbulence. In *Advances in Turbulence* (ed. G. Compte-Bellot & J. Mathieu), pp. 383–390. Springer-Verlag.

Johansson, A. V., Alfredsson, P. H. & Kim, J. 1991 Evolution and dynamics of shear-layer structures in near-wall turbulence. *J. Fluid Mech.* **224**, 579–599.

Johansson, A. V., Her, J.-Y. & Haritonidis, J. H. 1987*b* On the generation of high-amplitude wall-pressure peaks in turbulent boundary layers and spots. *J. Fluid Mech.* **175**, 119–142.

Kim, H. T., Kline, S. J. & Reynolds, W. C. 1971 The production of turbulence near a smooth wall in a turbulent boundary layer. *J. Fluid Mech.* **50**, 133–160.

Kim, J., Moin, P. & Moser, R. 1987 Turbulence statistics in fully developed channel flow. *J. Fluid Mech.* **177**, 133–166.

Kline, S. J., Reynolds, W. C., Schraub, F. A. & Runstadler, P. W. 1967 The structure of turbulent boundary layers. *J. Fluid Mech.* **30**, 741.

Kovasznay, L. G., Kibens, V. & Blackwelder, R. S. 1970 Large-scale motion in the intermittent region of a turbulent boundary layer. *J. Fluid Mech.* **41**, 283–325.

Kreplin, H.-P. & Eckelmann, H. 1979 Propagation of perturbations in the viscous sublayer and adjacent wall region. *J. Fluid Mech.* **95**, 305–322.

Moser, R. D., Kim, J. & Mansour, N. N. 1999 Direct numerical simulation of turbulent channel flow up to $Re_\theta = 590$. *Phys. Fluids* **11** (4), 943–945.

Österlund, J. M., Johansson, A. V., Nagib, H. M. & Hites, M. H. 1999 Wall shear stress measurements in high reynolds number boundary layers from two facilities. In *30th AIAA Fluid Dynamics Conference, Norfolk, VA*. AIAA paper 99-3814.

Rao, K. N., Narasima, R. & Badri Narayanan, M. 1971 The "bursting" phenomenon in a turbulent boundary layer. *J. Fluid Mech.* **48**, 339–352.

Robinson, S. K. 1991 Coherent motions in the turbulent boundary layer. *Ann. Rev. Fluid Mech.* **23**, 601–639.

Smith, C. R. & Metzler, S. P. 1983 The characteristics of low-speed streaks in the near-wall region of a turbulent boundary layer. *J. Fluid Mech.* **129**, 27–54.

Wallace, J. M., Eckelmann, H. & Brodkey, R. 1972 The wall region in turbulent shear flow. *J. Fluid Mech.* **54**, 39–48.

Willmart, W. W. & Lu, S. S. 1972 Structure of the Reynolds stress near the wall. *J. Fluid Mech.* **55**, 65–92.

Paper 7

Turbulent Boundary Layer Experiments in the MTL Wind-Tunnel

By Jens M. Österlund and Arne V. Johansson

Dept. of Mechanics, KTH, SE-100 44 Stockholm, Sweden

1. Introduction

The erection of the MTL wind-tunnel at KTH with its high flow quality and large Reynolds number range presented a possibility to design an experiment for the investigation of high Reynolds number turbulent boundary layers. The MTL tunnel was partly designed with this type of experiment in mind. Its design characteristics include: long test section, good flow uniformity, very low turbulence level, very low acoustic level, temperature control and adjustable pressure gradient (walls) along the test section.

In the past a number of experiments on turbulent boundary layers have been performed. Most of them in facilities designed for other purposes and most of them at low to moderate Reynolds numbers. Also most existing experiments have been made on the walls of the wind-tunnel introducing large uncertainties about the starting conditions of the boundary layer. Other troublesome features of existing experiments include low accuracy measurements of probe distance to the wall and the lack of independent skin friction measurements.

This made us decide on a set-up utilizing a flat plate mounted in the test section. This gives good control over the starting conditions. The adjustable walls of the MTL wind tunnel makes it possible to mount a 7 m long flat plate in the test section and still attain a zero pressure gradient, to a high accuracy, along the the growing boundary layer by adjusting the position of the opposite wall. The set-up included a highly accurate traversing mechanism fixed to the boundary layer plate and close to the measurement station to minimize any vibrations or deflection problems. The measurements were mainly done with hot-wire techniques and were greatly facilitated by use of the wind-tunnel temperature control system. The distance to the wall was measured by a laser distance meter aimed directly at the hot-wire probe. The wall distance measurement system was possible to use also when the tunnel was running. Finally, the skin friction was independently measured by use of oil-film interferometry.

This paper reports on the background and basics of extensive high Reynolds number experiments that form the basis of the present doctoral thesis.
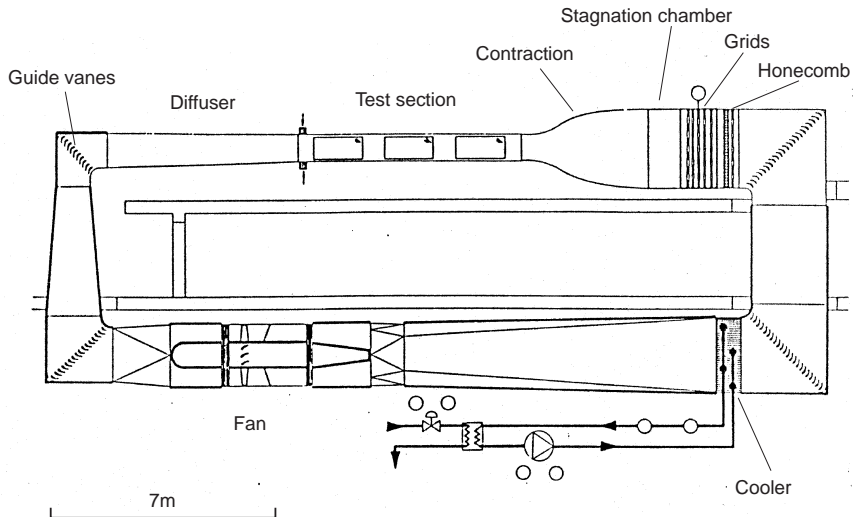
FIGURE 1. Schematic of the MTL wind tunnel facility at KTH

2. The MTL Wind Tunnel

All experiments were carried out in the MTL-wind tunnel at the department of mechanics, KTH. The MTL tunnel is specially designed for turbulence and transition experiments and the flow quality was reported in Johansson (1992). The tunnel was primarily designed at KTH and built by the French company Sessia. It was finished in 1990. The tunnel is a closed return facility, and is shown in figure 1. The test section is 7 m long with a cross sectional area of 1 m^2 (1.2 m × 0.8 m). The top and the bottom walls are adjustable in order to be able to control the streamwise velocity distribution in the test section. The circuit is ventilated to the surrounding atmosphere at the end of the test section giving atmospheric pressure in the test section. All corners utilize specially designed turning vanes to reduce the losses in the tunnel circuit, see Sahlin & Johansson (1991) and Lindgren *et al.* (1998). The tunnel is driven by a 86 kW fan located in the return leg between corners 2 and 3. It is equipped with a heat exchanger after the fan, and the temperature can be kept constant and uniform within ±0.05 °C. After the fourth corner the flow passes through a honeycomb flow-straightener and 5 screens before entering the settling chamber and the contraction, with a contraction ratio of 9, to the test section. Special care has been taken to reduce acoustic noise and a large part of the return circuit is equipped with noise-absorbing walls. The velocity can be controlled between 0-69 m/s.

total length	25 m
test section length	7 m
test section width	1.2 m
test section height	0.8 m
contraction ratio	9
mean velocity uniformity	$< 0.1\%$
mean velocity angularity	$< 0.1°$
temperature variations (in time)	$< \pm 0.05$ °C
temperature uniformity	$< \pm 0.2$ °C
streamwise turb. intensity	
in total 'central region'	$< 0.03\%$
near tunnel centerline	$< 0.015\%$
lateral turb. intensity (at 25 m/s)	
in total 'central region'	$< 0.06\%$
near tunnel centerline	$< 0.02\%$
noise (sound level, $f > 60$ Hz)	
at 35 m/s	69 dB
at 60 m/s	83 dB

TABLE 1. Basic characteristics of the MTL wind-tunnel at KTH.

3. Experimental set-up

3.1. *The boundary layer plate*

A 7 m long flat plate was mounted in the test section, see figure 2. The plate is a sandwich construction of aluminum sheet and aluminum square tubes made in 1 m long sections for ease of handling, see figure 3 for a detailed view of one plate section. The alignment of the edges between the plate sections was ensured by the use of 4 cylindric control pins at every connection. The step height was measured to be always less than 5 μm. The plate sections are resting on two horizontal beams running along the test section. The beams are adjusted strait and horizontal in the test section by use of adjustable supports, see figure 4. This system made it possible to adjust the large scale flatness of the plate to within ± 0.5 mm from the horizontal plane.

The leading edge shape is elliptical with an aspect ratio of 5, see figure 5. It was milled from a solid block of aluminum by use of a CNC machine. The surface was then polished to the final finish. Two pressure taps in the elliptical nose are used to position the stagnation point at the centerline of the plate. The taps are situated close to the point where the difference in pressure have maximum sensitivity to the angle of attack. The positioning of the stagnation point is done by a 1.5 m long flap mounted at the trailing edge on a hinge, see figures 6 and 7. The flap was adjustable with the tunnel running, which made
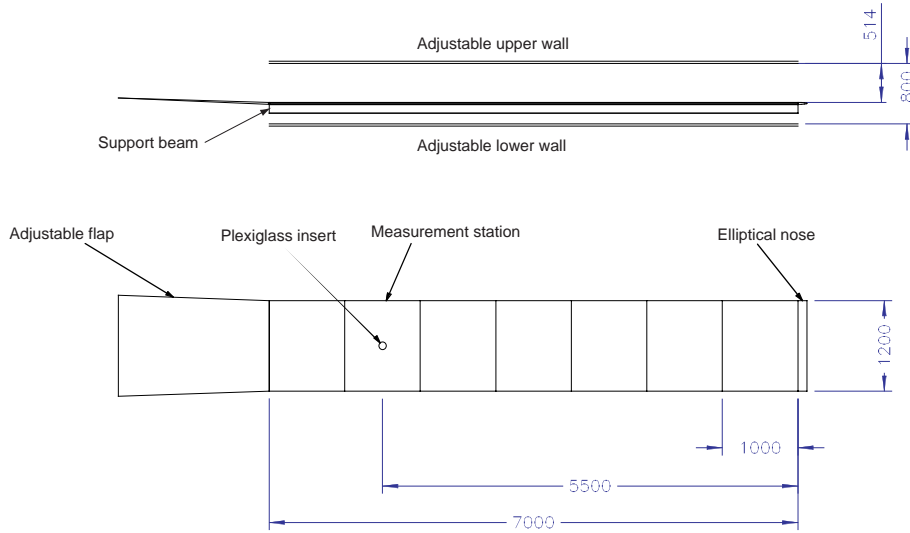
FIGURE 2. The boundary layer plate set-up.

it possible to accurately position the stagnation point at the leading edge to avoid any separation.

3.2. *Instrumentation*

3.2.1. *Ambient conditions.* Atmospheric pressure, p_{atm}, was measured using a barometer (from Furness control systems) located by the tunnel. The same equipment also registered the temperature, T, in the test section, with an accuracy of $0.1°$C. The instrument was connected to the measurement computer and was monitored during all measurements.

The atmospheric pressure and the temperature were used to calculate the density, ρ, and the kinematic viscosity using the perfect gas law,

$$\rho = \frac{p_{atm}}{\mathcal{R}T} \tag{1}$$

where $\mathcal{R} = 279.1$ J/kgK is the gas constant for air, and Sutherlands correlation,

$$\nu = 1.458 \cdot 10^{-6} \frac{T^{3/2}}{\rho(T + 110.4)}. \tag{2}$$

3.2.2. *Reference conditions and pressure measurement.* A reference Prandtl tube was positioned above the measurement position and used to monitor reference free stream dynamic and static pressure. The freestream velocity was
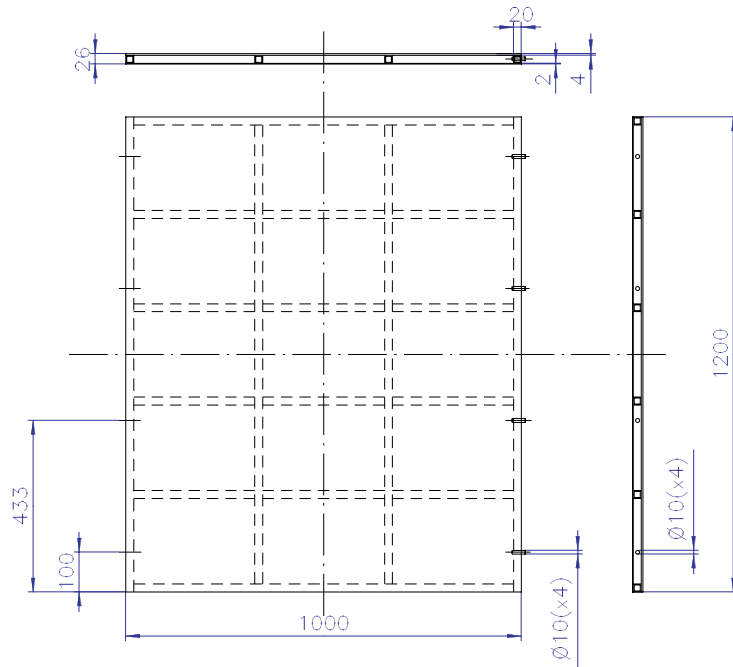
FIGURE 3. One plate section.
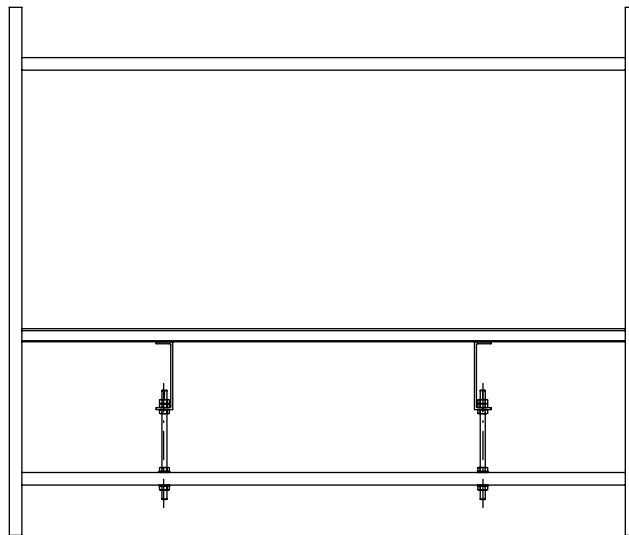
FIGURE 4. Cross section of the measurement section of the MTL wind-tunnel with the boundary layer plate installed.
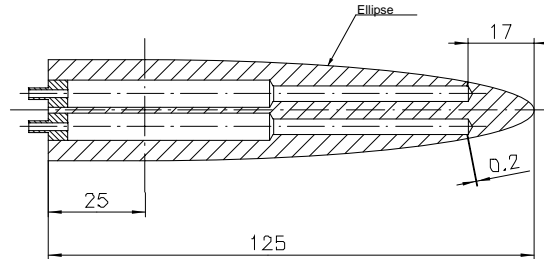
FIGURE 5. Cross section of the elliptical nose of the boundary layer plate. Pressure taps for controlling the stagnation point are seen close to the leading edge.
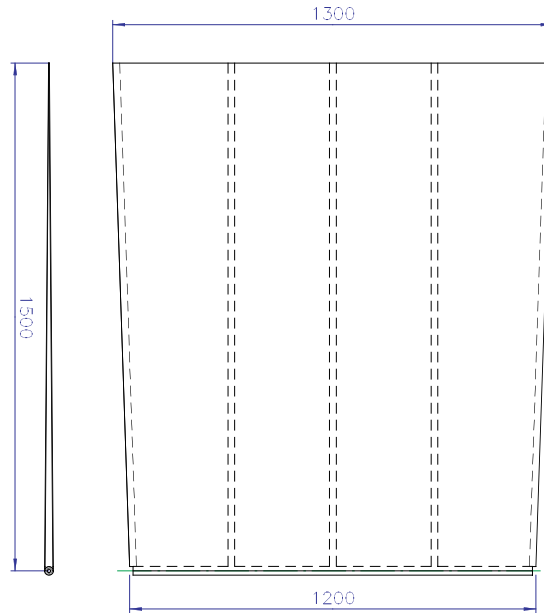
FIGURE 6. The trailing edge flap used to control the stagnation point at the leading edge.

calculated using,

$$U_\infty = \sqrt{\frac{2(p_{tot} - p)}{\rho}}.$$ (3)

The pressure measurements were done using a FCO510 electronic manometer (from Furness control Ltd), the accuracy being 0.25% of the full scale reading.
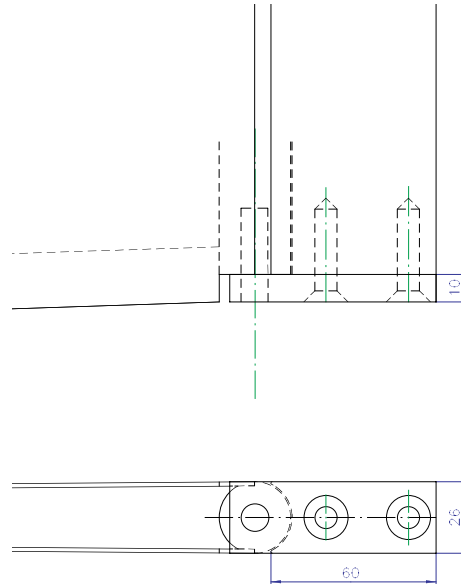
FIGURE 7. Detail of the flap attachment to the plate.

The RS232 output of the instrument was connected to the serial port of the measurement computer and was monitored during the measurements.

3.2.3. *Data acquisition equipment.* The voltage signals from the anemometer was digitized using an A/D-converter (AN-2000) from National instruments. The offset voltages from the signal amplifier, built into the anemometer, was measured using a multimeter connected to the measurement computer (using IEEE 488).

3.2.4. *Probe traversing.* A specially designed traversing system protruding from the plate was used to position the probes. It was mounted immediately behind the measurement station in a circular insert in the measurement station plate section. Under the plate the traversing mechanism was protected from the flow by a streamlined cover fixed to the tunnel floor. This prevented vibrations generated by vortex shedding to go into the traversing system. The vertical range of the system is 150 mm with a relative accuracy of $\pm 1\mu m$. For the two wire probe measurements a yaw angle traversing system was mounted on top for angular calibrations. The accuracy of that system is $\pm 0.01°$. The traversing is done by servo motors with optical encoders and was controlled from the measurement computer. The traversing system was mounted in one of the plate sections behind the Plexi-glass plug where all measurements were
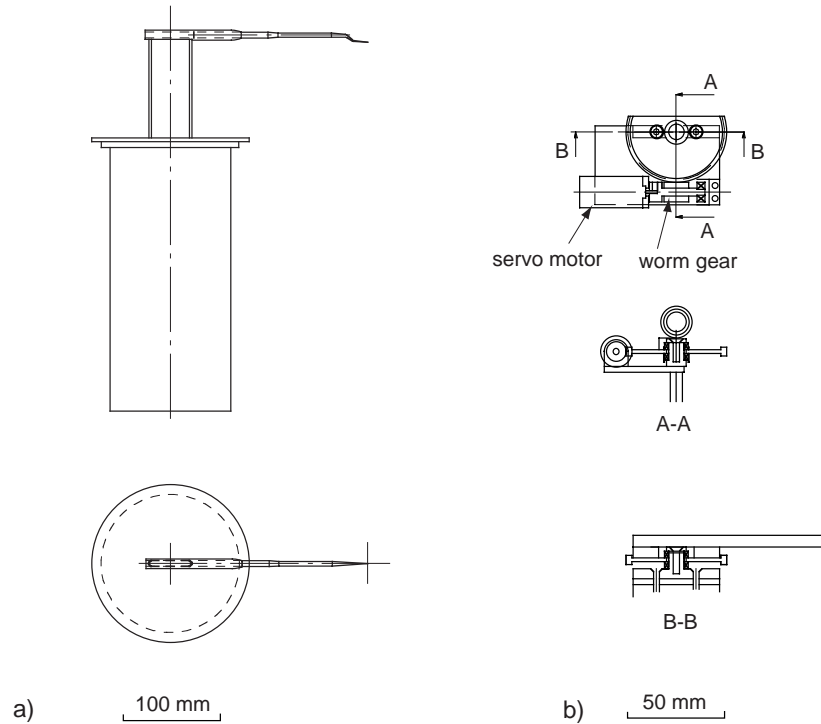
FIGURE 8. a) Schematic of the traversing system with a single wire probe mounted. The vertical range is 150 mm. b) When using two-wire probes the angular traversing unit was mounted at the top of the traversing arm. See also figure 9

.

taken. The position of the measurement plate section within the whole plate can be changed to obtain the following five streamwise measurement positions $x = \{1.5, 2.5, 3.5, 4.5, 5.5\}\,\mathrm{m}$.

3.3. *Tripping the boundary layer*

Normal transition occurs far downstream on the boundary layer plate. This makes it necessary to use a trip at the beginning of the plate. Several trip designs were tested. The selection was made by trial and error determining the transition velocity using a hot-wire 20 cm behind the trip.

The boundary layer was tripped by 8 rows of DYMO brand embossing tape letter "V" (width 8 mm), see figure 10. The height of the trip is 0.7 mm corresponding to less than half of the laminar boundary layer thickness at the
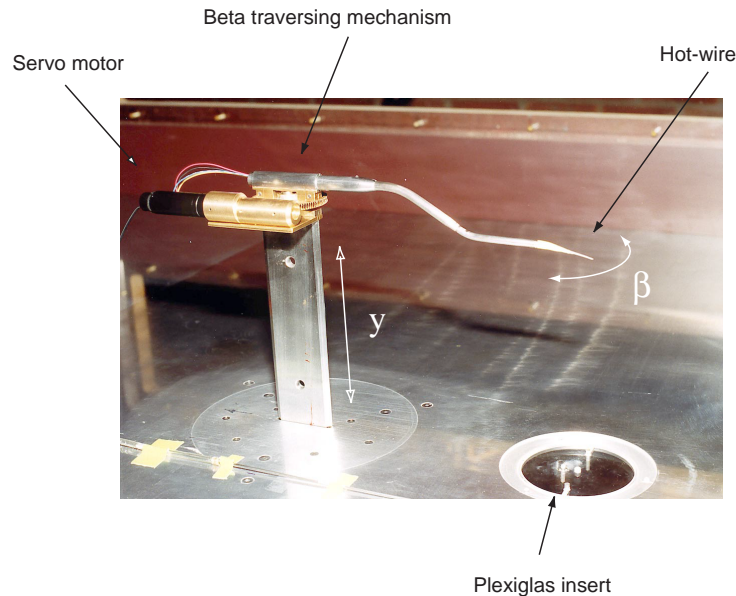
FIGURE 9. Photograph of the traversing arm with the angular traversing system mounted.

trip. This trip made the boundary layer fully turbulent at speeds down to 8 m/s.

3.4. *Zero pressure-gradient*

Zero pressure gradient was achieved by adjusting the upper wall of the tunnel test section. A very accurate but somewhat tedious procedure involving the adjustment of 48 screws on the upper wall of the tunnel was used. The most accurate method to measure the variation of the velocity in the free-stream was to traverse a single hot-wire probe along the test section using the tunnel main traversing system. This method is preferred to using the pressure-taps in the plate because it avoids the difficulty of manufacturing highly accurate pressure-taps. The upper wall was adjusted to give a variation of less than 0.2% along the plate, see figure 11.

3.5. *Two dimensionality of the boundary layer*

To check the two-dimensionality of the boundary layer the spanwise skin friction distribution was measured by traversing a Preston tube in the spanwise direction. The pressure measured from the Preston tube was referenced to a static pressure measured at the centerline of the plate. The skin friction was
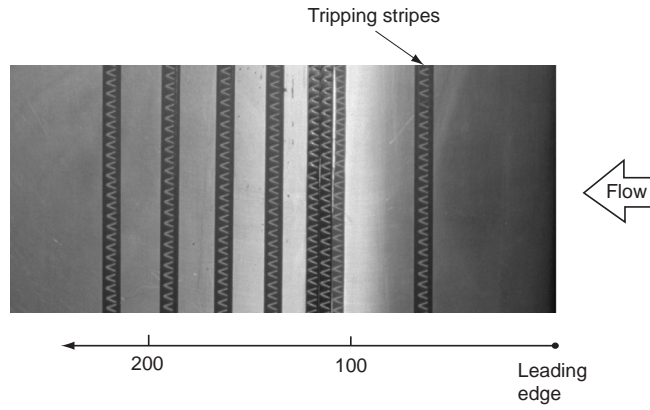
FIGURE 10. Photograph showing the trip device consisting of 8 Dymo brand embossing tapes. The letter V was used pointing downstream.
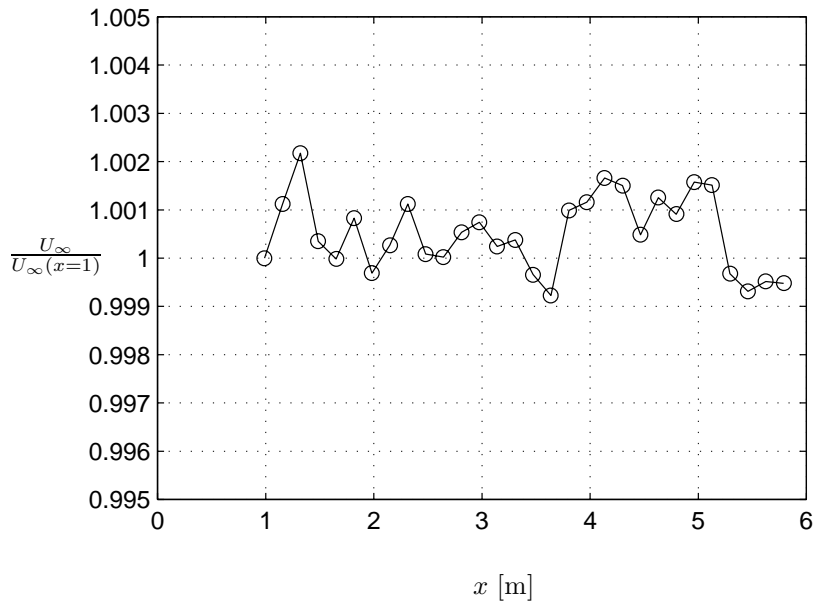
FIGURE 11. The relative streamwise variation of the external velocity, U_∞, along the centerline of the plate.

calculated using the explicit formula of Bechert (1995),

$$\tau^+ = (a\Delta p^{+2} + b\Delta p^{+3.5})^{1/4} \qquad (4)$$
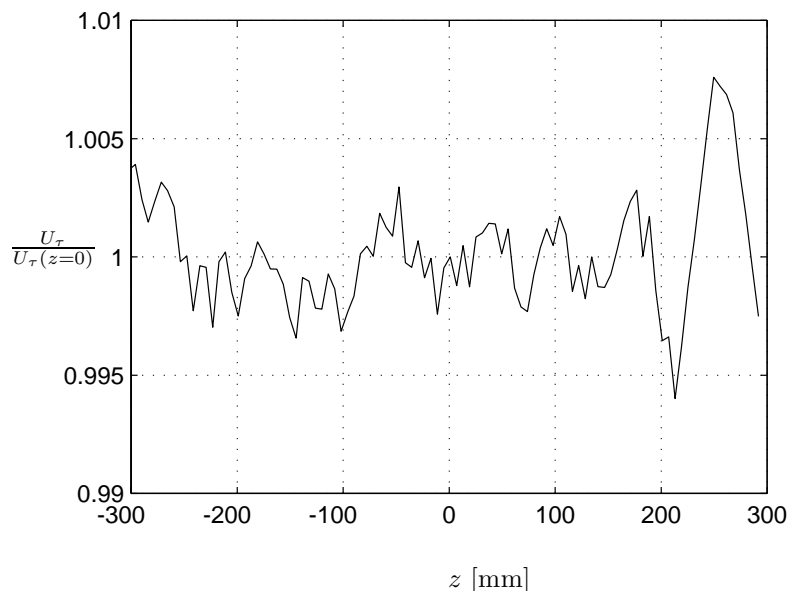
FIGURE 12. The relative spanwise variation of the friction velocity, U_τ, over the middle half of the plate.

where $a = 28.44$, $b = 6.61 \cdot 10^{-6}$, $\Delta p^+ = \Delta p d^2 / \rho \nu^2$ and $\tau = \tau^+ / d^2 \rho \nu^2$.

In figure 12 the spanwise friction velocity is shown. The very small variation across the boundary layer shows the homogeneous character of the flow.

3.6. *Flow quality*

Mean velocity profiles at one low and one high Reynolds number from the boundary layer are shown in figures 13 to 16. Note the large logarithmic region visible in the high Reynolds number measurement. Also shown in the figures are a linear profile $\overline{U}^+ = y^+$, the mean velocity from the DNS of Couette flow by Komminaho *et al.* (1996) and a logarithmic profile $\overline{U}^+ = 1/\kappa \ln y^+ + B$ with the constants $\kappa = 0.38$ and $B = 4.1$. The skin friction coefficient was measured using oil-film interferometry, see section 5.1, and was found to agree well with previous experiments, see figure 33, and also the correlation by Fernholz & Finley (1996). The shape factor is shown in figure 17.

3.7. *Wall-distance*

The distance from the wall to the probe was measured by a microscope with the tunnel shut off. To monitor the distance also when the tunnel was running a laser distance meter was mounted under the Plexiglas plug looking directly at the wire. This made it also possible to detect vibrations since the laser
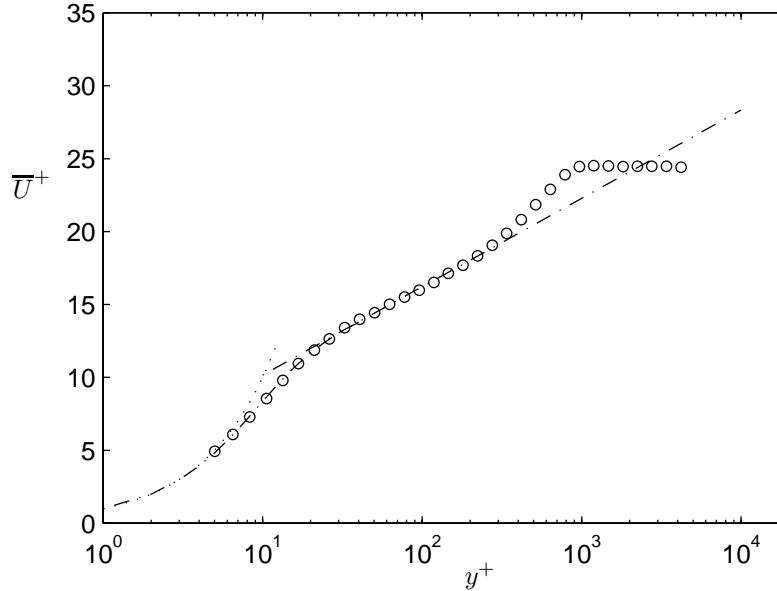
FIGURE 13. Example of a mean velocity profile at $Re_\theta = 2530$ in inner scaling on logarithmic axis. Dotted line: linear profile. Dashed line: DNS of Couette flow by Komminaho Komminaho *et al.* (1996). Dash dotted line: log-profile with constants $\kappa = 0.38$ and $B = 4.1$.

could follow the wire with frequencies up to 10 kHz. The range of the laser distance meter is 2 mm with an accuracy of $\pm 1\mu$m. The laser distance meter was calibrated using the microscope with the tunnel shut off. The error in the absolute wall distance measurements for the single-wire was ± 5 μm and for the X-wire ± 50 μm.

4. Hot-wire anemometry

The velocity was measured using constant temperature anemometry (CTA) in all experiments (system AN–1003 from AA lab systems in Israel). In constant temperature anemometry the hot-wire temperature is held constant by feedback control, while the current through the wire changes in response to fluctuating flow properties. The sensing hot-wire is one of the resistors in the active arm of a Wheatstone bridge. The sensor temperature is set by adjusting R_{adj}. The Wheatstone bridge produces an error voltage across the bridge diagonal when a resistive imbalance occurs. The amplifier serves as an actuator
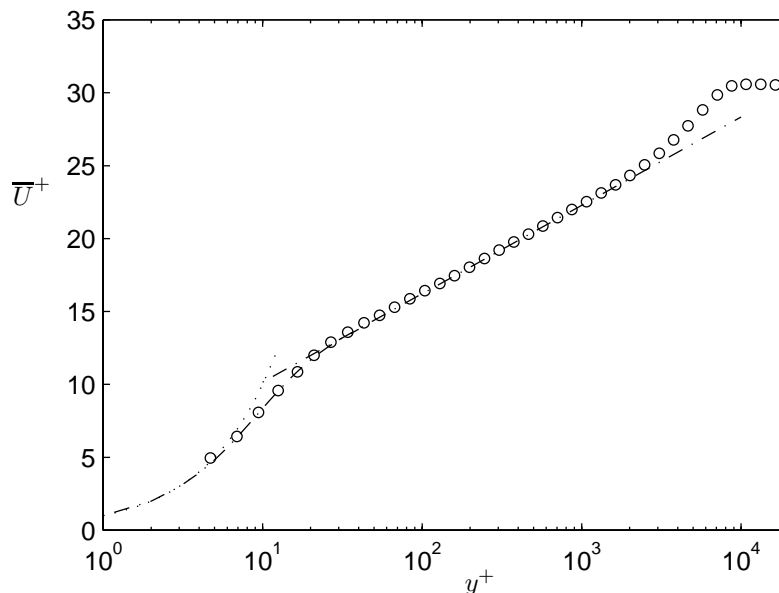
FIGURE 14. Example of a mean velocity profile at $Re_\theta = 26600$ in inner scaling on logarithmic axis. Dotted line: linear profile. Dashed line: DNS of Couette flow by Komminaho Komminaho *et al.* (1996). Dash dotted line: log-profile with constants $\kappa = 0.38$ and $B = 4.1$.

feeding current into the top of the bridge until the desired temperature of the sensor is achieved, thus balancing the bridge.

To first order the resistance of the hot-wire R_{w_H} is

$$R_{w_H} = R_{w_C}[1 + \alpha(T_{w_H} - T_{w_C})] \tag{5}$$

where T_{w_H} is the hot temperature, R_{w_C} and T_{w_C} are the cold resistance and temperature and α is the temperature coefficient of resistivity. The resistance and temperature overheat ratios are defined as

$$a_R = \frac{R_{w_H} - R_{w_C}}{R_{w_C}} \tag{6}$$

$$a_T = \frac{T_{w_H} - T_{w_C}}{T_{w_C}}. \tag{7}$$

The resistance overheat ratio a_R was selected to give the desired temperature overheat ratio $a_T = a_T/\alpha T_{w_C}$.
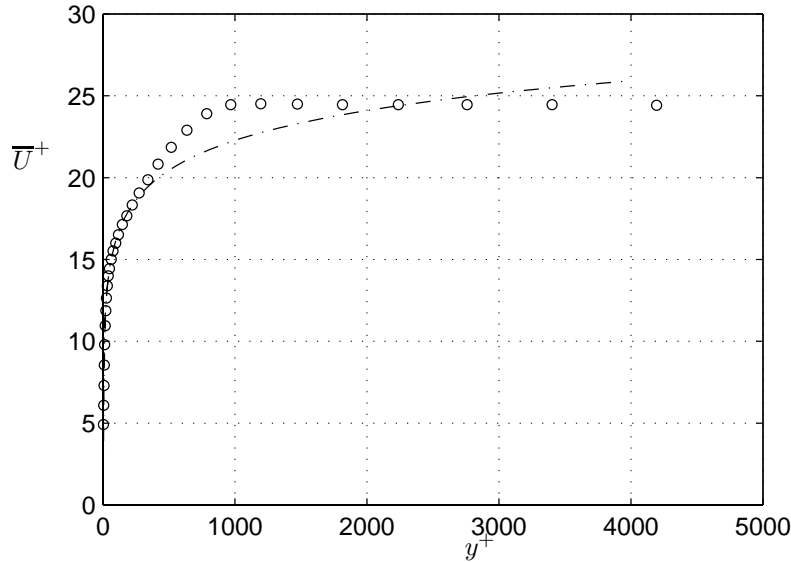
FIGURE 15. Example of a mean velocity profile at $Re_\theta = 2530$ in inner scaling on linear axis. Dotted line: linear profile. Dashed line: DNS of Couette flow by Komminaho Komminaho *et al.* (1996). Dash dotted line: log-profile with constants $\kappa = 0.38$ and $B = 4.1$.

Energy balance for the hot-wire in a cross-flow together with the heat transfer correlation by King results in

$$I^2 R_{w_H} = (A + BU^n)(T_{w_H} - T_{\text{amb}}) \tag{8}$$

where U is the effective velocity, A, B and n are constants characteristic of the heat transfer from the wire. The expression (8) is useful if temperature drift compensation is needed.

4.1. *Probe manufacturing*

The probe-bodies were built using ceramic tubes, designed for use in thermo elements, with 4 holes. The prongs were built from spring wire. The conical shape at the tips was etched in a bath of nitric acid (60%) using a technique where a small voltage was applied to speed up the etching. The delicate positioning of the prongs was done under a microscope (80x) and the positioning was done with a micro manipulating equipment. When the prongs are fixed in position a low viscosity epoxy resin is applied. Capillary forces pulls the resin into the probe body and fixes the prongs in position when hardened. To
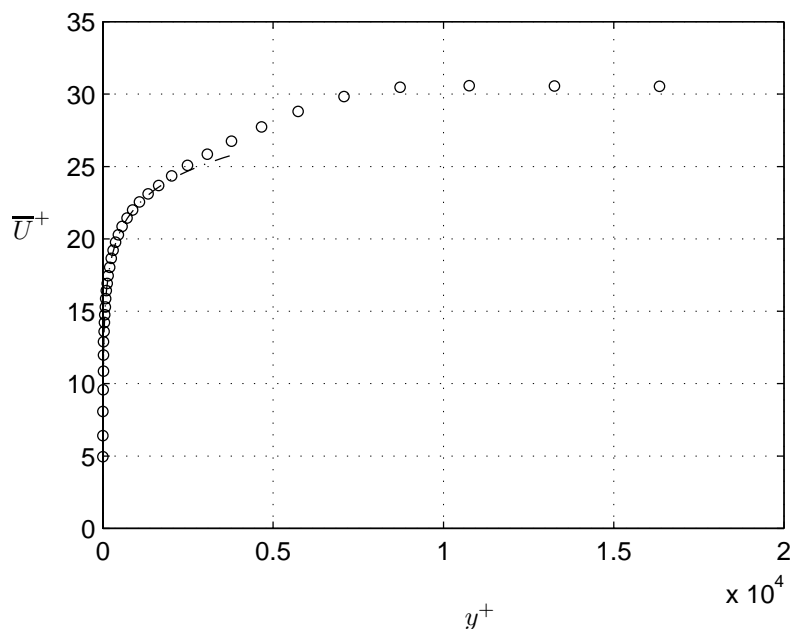
FIGURE 16. Example of a mean velocity profile at $Re_\theta = 26600$ in inner scaling on linear axis. Dotted line: linear profile. Dashed line: DNS of Couette flow by Komminaho Komminaho *et al.* (1996). Dash dotted line: log-profile with constants $\kappa = 0.38$ and $B = 4.1$.

fix the prongs together outside of the ceramic body a mixture of epoxy resin and colloidal silicon was applied. Before gluing the probe together the prongs were covered by a thin layer of solder to protect them from corrosion and to later be used for the soldering of the platinum wires. The soldering is done by putting the etched piece of the Wollastone wire in position, by use of a micro-manipulator, and then heating the prong with the soldering iron a few mm away until the solder melts. The length to diameter ratio was always kept more than 200. The diameter of the prong edge was about $20 - 30\mu m$. The wires were soldered on the inside of the prongs to make the distance between the wires as small as possible see figure Extreme care has to be taken when positioning the prongs to assure that the wires are parallel. The deviation from parallelism was kept smaller than about $5\mu m$.

4.2. *Hot-wire anemometer calibration procedure*

All hot-wires were calibrated in the free stream against a Prandtl-tube immediately before every set of measurements. The probes were never moved
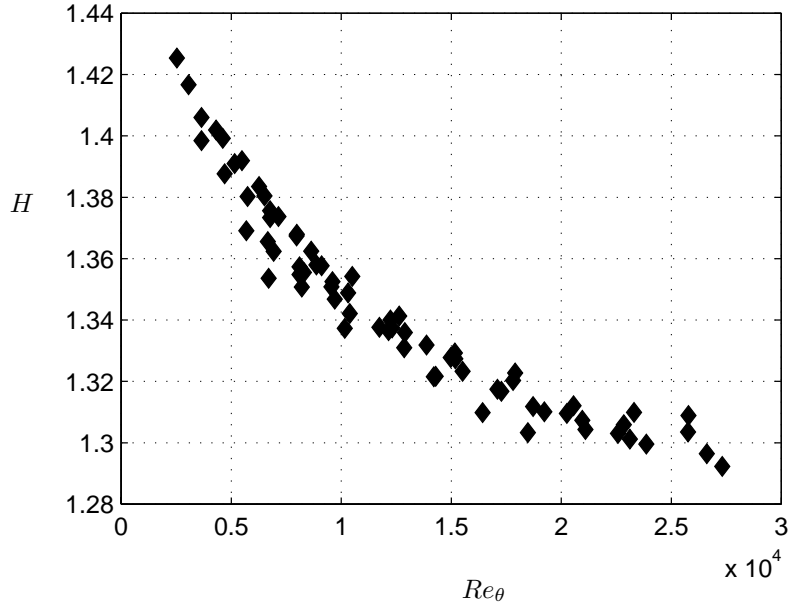
FIGURE 17. Shape factor $H = \delta^*/\theta$, as a function of Reynolds number.

or disconnected between calibration and measurement. The calibration was checked after the measurement and if a significant difference occurred the measurement was discarded and the calibration was redone. This happened a few times during the experiments mostly as an effect of dust particles hitting the probe.

4.2.1. *Single-wire calibration procedure.* The single wire probes were traversed to a position outside of the boundary layer. The velocity of the tunnel was changed and the temperature was allowed to settle at the control point. Therefore no temperature compensation was used. The anemometer voltage signal was recorded together with the Prandtl-tube pressure difference. Repeating this over the range of mean velocities encountered in the experiment allows a calibration table to be determined. The calibration curve used during the evaluation of the experiment was obtained by fitting King's law of the type,

$$\overline{U} = \left(\frac{E^2 - A}{B}\right)^{1/n} \tag{9}$$

using the calibration table.
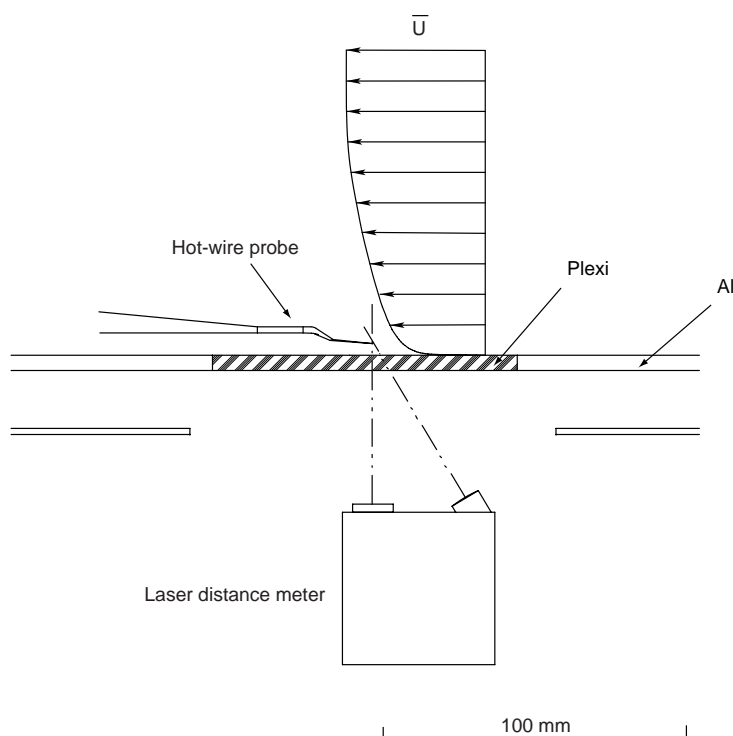
FIGURE 18. Distance measurement set-up with laser sensor.

4.2.2. *Two-wire probes*. Two types of two-wire probes were used: X-wire probes oriented to measure the U and V velocity components, and V-wire probes oriented to measure the U and W velocity components.

Both types of probes were calibrated *in-situ*, in the free stream outside of the boundary layer. An angular traversing mechanism, see figure 8 and 9, was mounted during the double wire measurements. It was capable of rotating the probe around the y-axis and thereby allowing for both angular and velocity calibration of the probes. Before the calibration the X-probe was rotated 90° around the probe centerline to enable calibration. After the calibration the probe was rotated 90° back to its original position. This calibration procedure was fully automated by the computer controlling the angle of attack of the probe and the speed of the wind tunnel.

The two voltages from the anemometer bridges, the angle of attack and the freestream velocity, measured by a Pitot tube, were registered at typically 7 angles, from $-30°$ to $30°$, and 7 velocities in the expected range, see figure 19. The help variables $x = E_1 + E_2$ and $y = E_1 - E_2$ related to U and V are calculated and two 2-dimensional fifth order polynomials,
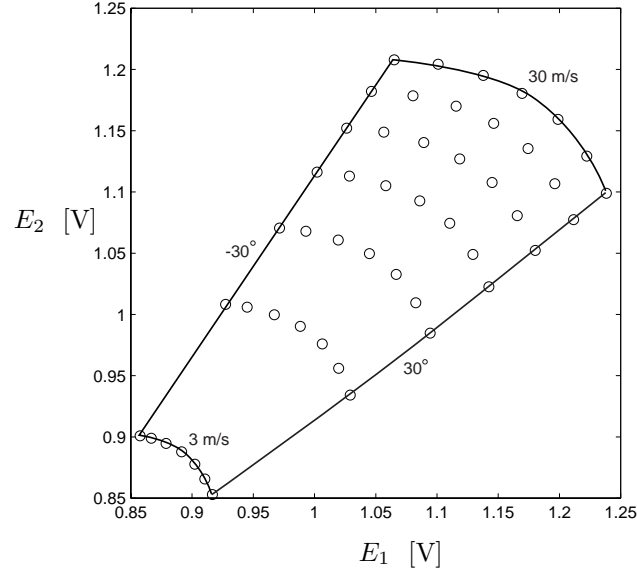
FIGURE 19. Example of a calibration of an X-wire probe.

$$
\begin{aligned}
U =\; & a(0,0) + a(1,0)x + a(2,0)y + a(3,0)x^2 + a(4,0)yx + a(5,0)y^2 \\
& + a(6,0)x^3 + a(7,0)yx^2 + a(8,0)y^2x + a(9,0)y^3 + a(10,0)x^4 \\
& + a(11,0)yx^3 + a(12,0)y^2x^2 + a(13,0)y^3x + a(14,0)y^4 + a(15,0)x^5 \\
& + a(16,0)yx^4 + a(17,0)y^2x^3 + a(18,0)y^3x^2 + a(19,0)y^4x + a(20,0)y^5 \\
\tan\alpha =\; & a(0,1) + a(1,1)x + a(2,1)y + a(3,1)x^2 + a(4,1)yx + a(5,1)y^2 \\
& + a(6,1)x^3 + a(7,1)yx^2 + a(8,1)y^2x + a(9,1)y^3 + a(10,1)x^4 \\
& + a(11,1)yx^3 + a(12,1)y^2x^2 + a(13,1)y^3x + a(14,1)y^4 + a(15,1)x^5 \\
& + a(16,1)yx^4 + a(17,1)y^2x^3 + a(18,1)y^3x^2 + a(19,1)y^4x + a(20,1)y^5
\end{aligned}
$$
$$(10)$$

are fitted to both $\overline{U}$ and $\tan\alpha = V/U$ using the calibration table. The polynomial coefficients a_{ij} are determined by a least-squares method and are stored for use by the evaluation programs.

5. Skin friction

The relevant scaling velocity for turbulent boundary layers is the so called friction velocity $u_\tau = \sqrt{\tau_w/\rho}$. Therefore the determination of skin friction τ_w is of vital importance in these experiments and turned out to be one of the most difficult tasks. Most of the simple and popular methods, like the Preston tube, Preston (1953) and the Clauser chart, Clauser (1954), require the assumption

that the universal law-of-the-wall holds in the turbulent boundary layer. The most commonly used Preston tube calibration is the one by Patel (1965) where the calibration was conducted in a fully developed pipe flow where the skin friction is known from the pressure drop. Therefore it assumes similarity between pipe and boundary layer flow. Since we wanted to investigate the law-of-the-wall we had to look for other methods. Recent surveys of different skin friction measurement techniques was written by Winter (1977), Haritonidis (1989) and Fernholz *et al.* (1996). Only three methods independent of the law-of-the-wall, that do not require calibration exist: the floating element gauge, direct measurement of the velocity gradient at the wall Naqwi & Reynolds (1991) and Obi *et al.* (1996)) and the oil-film method. The latter was used to determine the skin friction in this experiment.

5.1. *Oil-film interferometry*

The oil-film interferometry is one of a few independent absolute skin-friction measurement techniques. Tanner & Blows (1976) were the first to use oil-film interferometry to measure skin friction. The method have since then been further developed by Monson (1983), Janke (1994), Seto & Hornung (1993) and Nishizawa *et al.* (1998).

The basis of the oil-film method is to measure the change in thickness of a small droplet of silicon oil on the wall when it is deformed by the skin friction from the boundary layer. The thickness of the oil-film was measured using an optical interference method. Fizeau fringes originate when light reflected from the upper surface of the oil interferes with light reflected from the plate, see figure 20. A sequence of images is shown in figure 21. The fringe pattern was registered using a video camera. The properties of the silicon oil depend on the temperature, and the cooling system of the tunnel was able to keep the temperature within ± 0.1 °C. The oil viscosity dependence on temperature was carefully calibrated as described in section 5.1.2.

Using monochromatic light the height of the k-th black fringe is given by,

$$h_k = h_0 + k\Delta h, \qquad k = 0, 1, 2 \ldots \tag{11}$$

$$\Delta h = \frac{\lambda}{2\sqrt{n^2 - \sin^2(\alpha)}} \tag{12}$$

where h_0 is the height at the zeroth fringe, Δh is the difference in height between two fringes, α the angle of the camera axes to a normal of the plate, λ the wave length of the light.

Analyzing the flow in the oil-film, see figure 24, assuming two dimensionality and applying a thin-film approximation reduces the Navier-Stokes equation
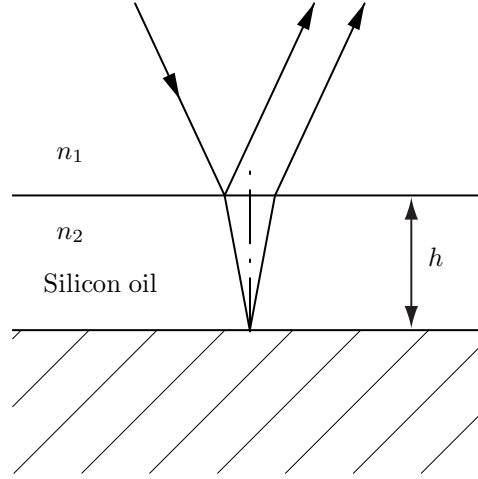
FIGURE 20. Fizeau interference in the thin layer of oil.

for the oil-film to,

$$0 = \frac{\partial^2 u}{\partial y^2}. \tag{13}$$

The continuity equation and boundary conditions are given by,

$$\frac{\partial u}{\partial x} + \frac{\partial v}{\partial y} = 0. \tag{14}$$

$$u = v = 0, \qquad y = 0 \tag{15}$$

$$\mu \frac{\partial u}{\partial y} = \overline{\tau_w}, \qquad y = h(x,t) \tag{16}$$

and the initial condition is

$$h(x,0) = \phi(x). \tag{17}$$

Equations 13–17 together with the surface condition $v = \frac{\partial h}{\partial t} + u \frac{\partial h}{\partial x}$ reduces to the following simple advection equation for the thickness of the oil-film,

$$\frac{\partial h}{\partial t} + \frac{1}{2\mu} \frac{\partial(\overline{\tau_w} h^2)}{\partial x} = 0 \tag{18}$$

For constant skin friction, a good approximation in zero pressure gradient boundary layers, equation 18 further reduces to,

$$\frac{\partial h}{\partial t} + \frac{\overline{\tau_w} h}{\mu} \frac{\partial h}{\partial x} = 0 \tag{19}$$
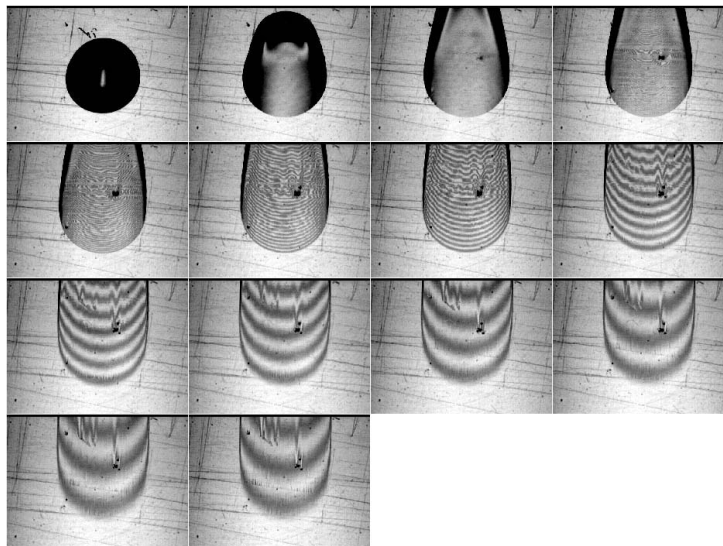
FIGURE 21. Sequence of images showing the Fizeau fringes generated from the interference of the light reflected from the top and from the bottom of the oil-film. The thinning of the oil-film is clearly seen.

with the solution,

$$h = \phi[x - \frac{\overline{\tau_w}h}{\mu}t]. \tag{20}$$

In fact, at large times the main part of the oil-film will approach the similarity solution,

$$h = \frac{\mu x}{\overline{\tau_w}t}, \tag{21}$$

regardless of the initial condition 17. Keeping $h = \text{const.} = h_k$, that is staying on one fringe, equation 20 gives,

$$\left.\frac{\partial x}{\partial t}\right|_{h=h_k} = \frac{\overline{\tau_w}h_k}{\mu} = u_k \tag{22}$$

the fringe velocity in the x–t plane. Combining 22, 11 and 12 we arrive at,

$$\overline{\tau_w}k + \overline{\tau_w}\frac{h_0}{\Delta h} = \mu u_k \frac{2\sqrt{n^2 - \sin^2\alpha}}{\lambda} \tag{23}$$

where μ, α, n and λ are known and an arbitrary number of fringe velocities u_k can be measured from the x–t diagram. We have an over-determined system of linear equations for the quantities $\overline{\tau_w}$ and $h_0/\Delta h$, which can be computed by a least squares fit.
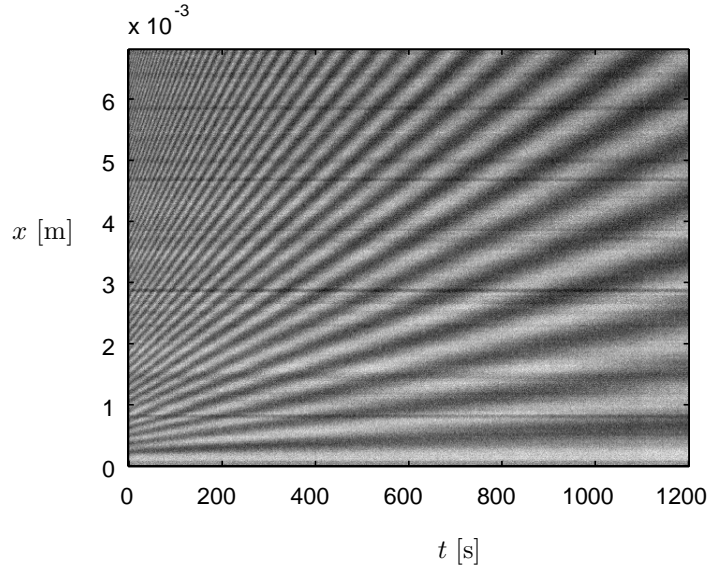
FIGURE 22. *X–t* diagram showing the development of the oil-film thickness.

The captured images were cut to generate *x–t* diagrams like figure 22. About 10 fringe velocities u_k were deduced from the *x–t* image by fitting straight lines to the fringes by use of a computer program. The skin friction τ_w and $h_0/\Delta h$ were calculated from equation 23. Results are discussed in section 5.4 and shown in figure 33.

5.1.1. *Optical set-up.* The optical set-up was determined by the need to depict an area less than one cm^2 from a distance of about 1 m. The video camera has an 8 mm black and white ccd-chip with a resolution of 512x640 pixels. A 300 mm lens from Nikkor was mounted together with the camera on a steel holder with a telescopic cover between the two, to prevent light from the sides to reach the ccd. The holder was mounted on a stand on top of the upper test-section wall, see figure 23. The optical path into the test section was through the slit in the wall where the sealing mylar films temporarily were removed under the camera and the light source. The fringes were obtained on an acrylic plug with a diameter of 100 mm that was mounted in the test station plate. To illuminate the oil-film a standard sodium lamp from Osram was used ($\lambda = 589$ nm). The analog video image from the camera was digitized by a computer (PowerMac 9500/100) at specified time intervals. The image stack was stored on the hard disc together with the necessary parameters for later processing and determination of the wall shear stress.
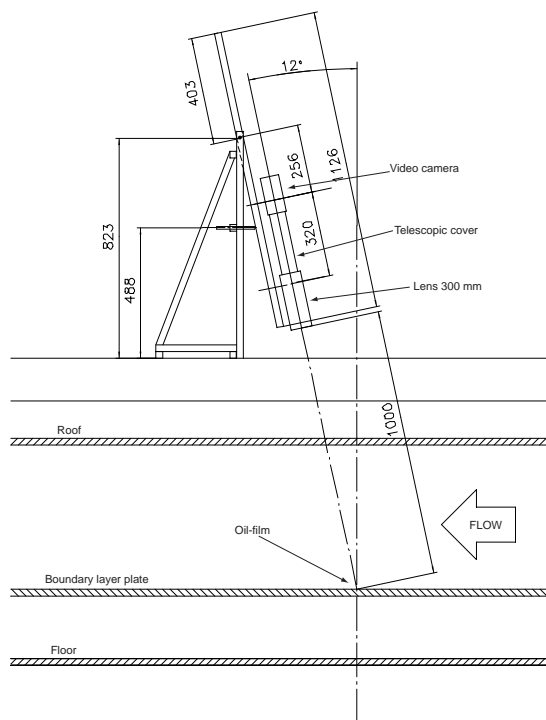
FIGURE 23. Oil-film set-up in the test section of the MTL wind-tunnel.

5.1.2. *Calibration of the Silicon oil.* Accurate knowledge of the viscosity of the silicon oil is of course of primary importance for the oil-film method. Therefore the viscosity given by the manufacturer was not used. Partly because of the low accuracy given and also due to the fact that the oil is subject to aging.

Standard viscometer tubes, see figure 25, were used in the calibration set-up. The tubes were submerged in a temperature controlled water bath (figure 26) and the viscosity was repeatedly measured at several different temperature settings. In figure 27 the results from the calibration are shown together with a curve fit of the type,

$$\nu = \nu_{25} e^{k(25-T)}. \tag{24}$$

In table 2 the properties for the two different oils are shown. The density and the refractive index were taken as the values given by the manufacturer.

5.2. *Near-wall method*

Direct measurement of the velocity gradient at the wall is one direct and independent method to determine the skin friction. To determine the gradient
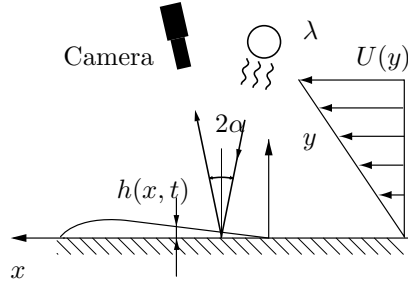
FIGURE 24. Schematic of oil-film technique.

TABLE 2. Silicon oil properties

Oil	ρ [kg/m^3]	n	k	ν_{25} [m^2/s]
DC200/200	970	1.403	$1.95 \cdot 10^{-2}$	$205.1 \cdot 10^{-6}$
DC200/20	949	1.4	$1.78 \cdot 10^{-2}$	$19.23 \cdot 10^{-6}$

by measurement of the velocity at different heights, and thereby calculate the derivative, one has to do accurate measurements below $y^+ = 3$. With currently available measurement techniques this is not possible to do, particularly not at high Reynolds numbers and/or low Prandtl numbers. In the current experiments this would require accurate measurements closer than 30 μm from the wall.

Therefore, a new method to determine the wall-shear stress has been developed. The new method is not an independent method since it needs calibration. The idea is to determine the skin friction from the measured velocity profile in the inner layer, using the law of the wall,

$$\overline{U}^+ = \frac{\overline{U}}{u_\tau} = f\left(y^+\right); \quad \overline{y}^+ = \frac{yu_\tau}{\nu} \tag{25}$$

at a distance from the wall where it is possible to make accurate measurements. The measured velocity profile is fitted to the law-of-the-wall in a procedure minimizing the mean-square error. This is similar to what is done when using the Clauser method in the logarithmic region of the velocity profile. The problem with using the Clauser method is obvious since it assumes similarity in the overlap region and that is part of our investigation. The underlying assumptions for the use of Preston tubes are similar.

In order to utilize accurate mean velocity measurements to evaluate the wall-shear stress, the form of the law-of-the-wall was chosen from available
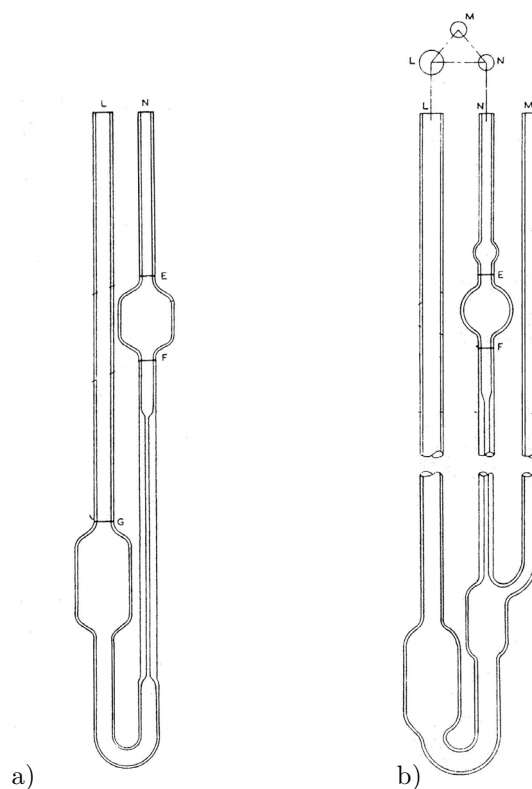
FIGURE 25. Viscometers used in the calibration of the silicon oil. a) BS/U viscometer. b) Suspended-level viscometer.

direct numerical simulations (DNS) of turbulent shear flows. Since the DNS data are available with great detail in the region where accurate measurements can be achieved and where the measurements are still well within the inner layer, the range $6 < y^+ < 20$ was selected for this near-wall method. In Figure 28, the mean velocity profiles from several recent direct numerical simulations are reproduced. The Couette flow simulation was chosen since it most closely resembles the flow in the inner part of a high Reynolds number turbulent boundary layer. In particular, there is no streamwise pressure gradient in this flow and the total shear stress is constant, over a range of distances from the wall, as shown in figure 29. Note that for this flow $\overline{\tau}^+ = 1$. This is a method which is both simple and convenient, and should yield quite accurate results. The skin friction coefficient evaluated using the near-wall method is shown in figure 33 and is discussed in section 5.4

Jens M. Österlund and Arne V. Johansson
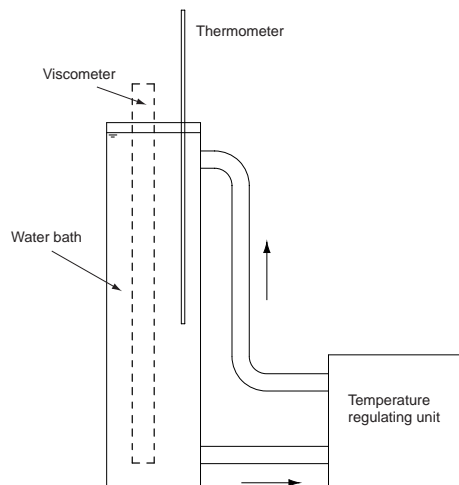
FIGURE 26. Viscometer set-up showing the temperature regulated water bath
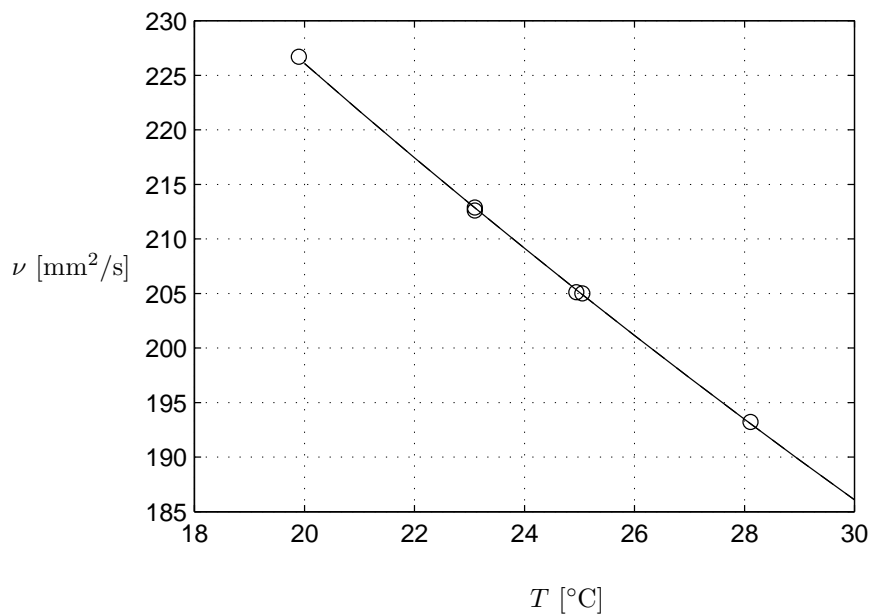
FIGURE 27. Kinematic viscosity of the silicon oil (DC200/200).
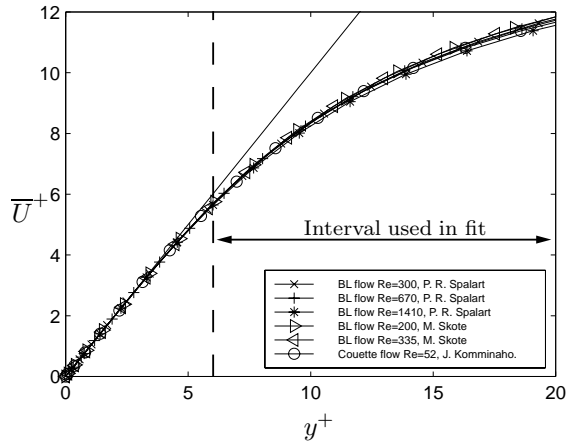
FIGURE 28. Mean velocity from DNS of boundary layer by Spalart (1988) and Skote *et al.* (1998), and Couette flow by Komminaho *et al.* (1996).
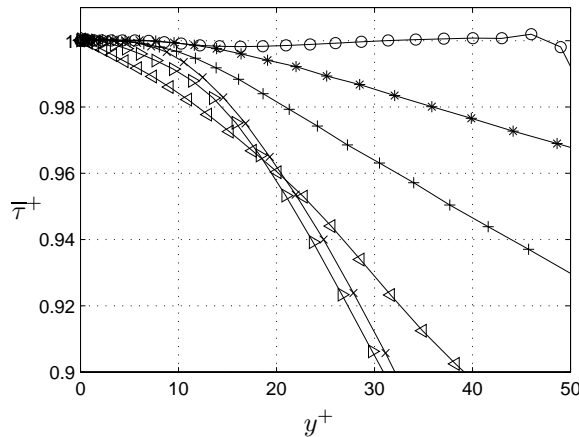
FIGURE 29. Total shear stress from DNS calculations; for legend see Figure 28

5.3. *MEMS hot-film*

For the measurements of the fluctuating part of the skin-friction MEMS-type probes were used and also the near-wall hot-wire technique, Fernholz *et al.* (1996). The MEMS probe, see figure 30, was designed and constructed by Prof. Ho's group at UCLA/Caltech, Jiang *et al.* (1996); Ho & Tai (1998). It was mounted in a cut-out of a printed circuit board (PCB) with all electrical connections on the back except the wire-bonding needed to connect the chip to the PCB, see figure 31. The PCB was fitted into a Plexiglas plug, see figure 32,

that fits into the circular hole at the measurement station. The calibration of the MEMS hot-film and the wall hot-wire was done in the turbulent boundary layer using the skin friction law determined with the oil film technique. The mean skin-friction ranged from 0.3 to 3 times the mean values of interest in the measurements (Alfredsson *et al.* 1988).

A modified Kings law was fitted to the data minimizing the mean square error of the difference between the skin friction measured by the oil film and the skin friction calculated from the hot-film using the calibration function. This method is similar to the one used by Fernholz *et al.* (1996).

Let,

$$b_j = j - 2049, \qquad j = 1, 2, \ldots, 4096 \tag{26}$$

be the sample space (12 bit A/D converter resolution). We use the modified King's law as described in Fernholz *et al.* (1996),

$$u_j = (\frac{1}{B}(E_j^2 - A))^{1/n} \tag{27}$$

$$\tau_j = \left(\sqrt{u_j + \frac{k_1}{4} - k_2} - \frac{k_1}{2} \right)^2 \tag{28}$$

where $E_j = E(b_j)$ is the relation between the sample space b_j and the measured voltages E_j. Let τ_n^* be the skin friction measured by the oil-film technique at N calibration points and $\bar{\tau}_n$ be the mean skin friction measured by the hot-film using the calibration function 27. Calculate the error at calibration point n,

$$e_n = \tau_n^* - \bar{\tau}_n \tag{29}$$

The least squares method,

$$\min \left(\sum_{n=1}^{N} e_n^2 \right) \tag{30}$$

gives,

$$\min \left(\sum_{n=1}^{N} \left(\tau_n^* - \sum_{j=1}^{4096} \tau_j P_{\tau_n}(j) \right)^2 \right) \tag{31}$$

where $P_{\tau_n}(j)$ is the probability density function at calibration point n. The minimization procedure gives the set of parameters $\{A, B, n, k_1, k_2\}$ that minimizes the mean square error of 29.
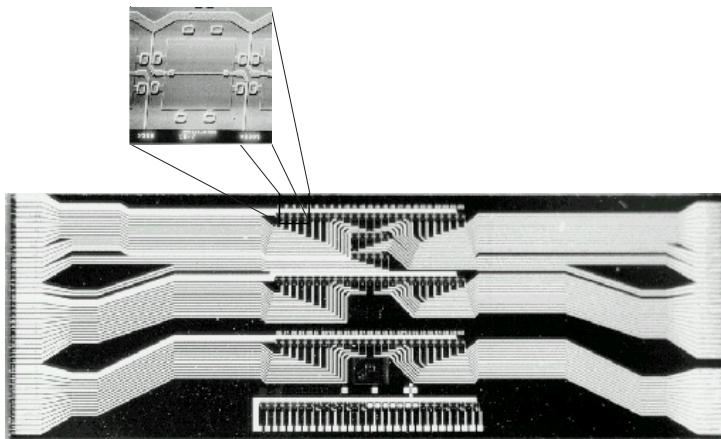
FIGURE 30. The UCLA/Caltech MEMS Hot-film sensor chip
with close-up of one hot-film.

5.4. *Skin friction results*

The results from the skin friction measurements are summarized in Figure 33.
A fit to c_f by a variant of the logarithmic skin friction law,

$$c_f = 2 \left[\frac{1}{\kappa} \ln(Re_\theta) + C \right]^{-2}, \tag{32}$$

was made for each of the data sets. The value of the von Kármán constant
determined from the oil-film data in this way was $\kappa = 0.384$ and the additive
constant was found to be $C = 4.08$ and the value of the von Kármán con-
stant determined from the near-wall method was $\kappa = 0.385$ and $C = 4.28$, see
Österlund *et al.* (1999). In Figure 33, the results from the oil-film measure-
ments together with the values of the skin friction determined from the mean
velocity by the near-wall technique, are shown together with the calculated
best fits using equation (32). The resulting logarithmic skin-friction laws agree
very well with each other and also with the correlation developed by Fernholz
(1971).
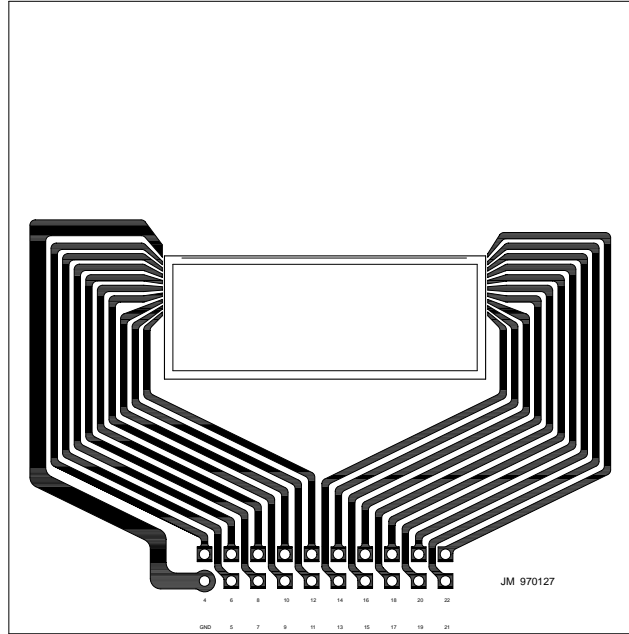
FIGURE 31. The circuit board where the MEMS chip was mounted.

6. Data Evaluation

6.1. *Calculation of statistical moments*

Calculation of statistical moments of the velocity components U, V and W is of primary importance. The mean, variance, skewness and flatness provide established descriptive characteristics of the boundary layer profile. The calculation of these moments was performed using different methods for the single-wire and the double-wire probes and are presented here for reference.

6.1.1. *Moments from single-wire data.* The analog voltage signal from the anemometer was sampled by the A/D converter and transformed into digital data consisting of N data values with an equally spaced sampling interval Δt. The sample data

$$\{B_i\} \qquad i = 1, 2, \ldots, N, \tag{33}$$

have a total record length $T = N\Delta t$ being associated with the times $t_i = i\Delta t$. The 12 bit A/D converter maps the voltage signal in the range of ± 5 V into the sample space b_j,

$$B \in \{-2048, \ldots, 2047\} = b_j \qquad j = 1, \ldots, 4096. \tag{34}$$
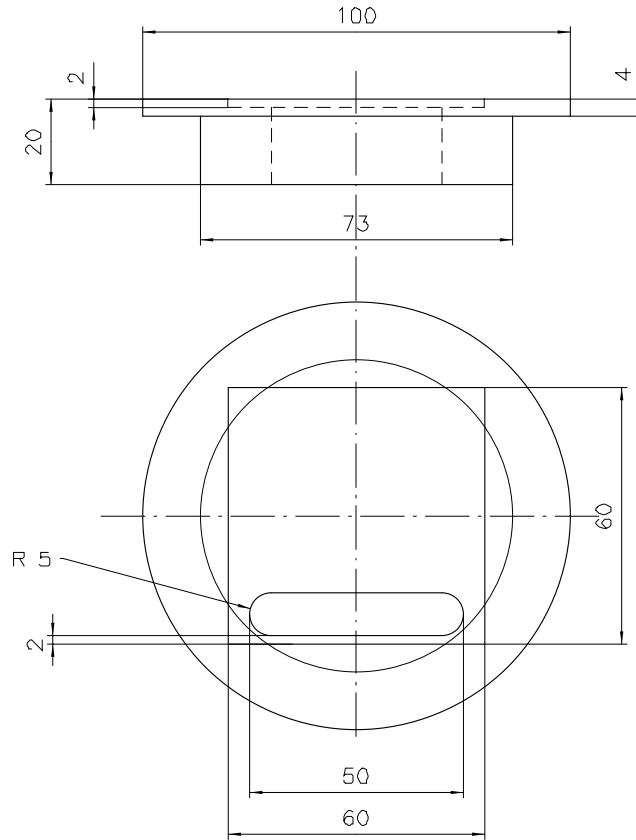
FIGURE 32. The plug where the printed circuit board with the MEMS hot-film was mounted.

The mean value of the sample data $\{B_i\}$, can be expressed as,

$$E(B) = \frac{1}{N} \sum_{i=1}^{N} B_i = \frac{1}{N} \sum_{j=1}^{4096} \sum_{B_i=b_j} B_i = \frac{1}{N} \sum_{j=1}^{4096} \sum_{B_i=b_j} b_j \qquad (35)$$

$$= \frac{1}{N} \sum_{j=1}^{4096} b_j \underbrace{\sum_{B_i=b_j} 1}_{n_j} = \sum_{j=1}^{4096} b_j P_j \qquad (36)$$

giving the discrete probability density function,

$$P_j = \frac{n_j}{N}, \qquad j = 1, \dots, 4096. \qquad (37)$$
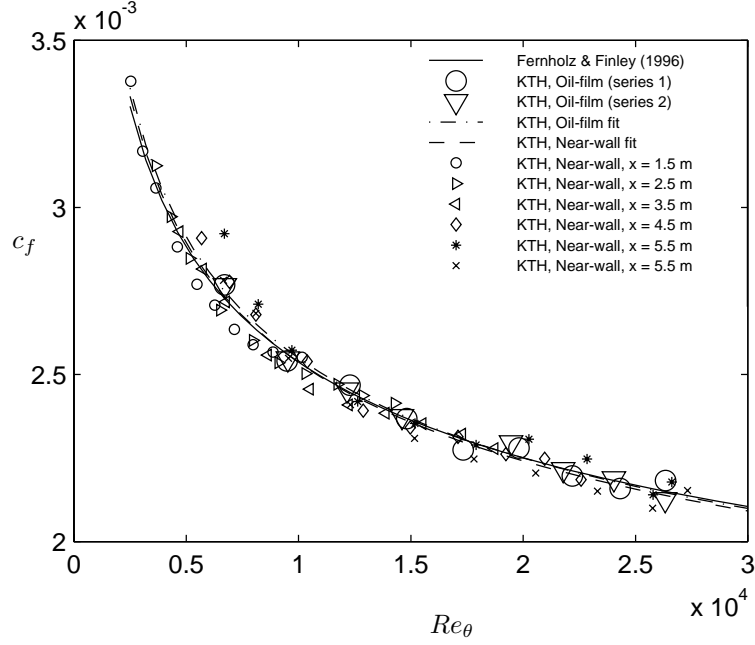
FIGURE 33. Skin-friction coefficient using the oil-film and near-wall methods, shown with best-fit logarithmic friction laws from Equation (32) and the correlation of Fernholz & Finley (1996).

If the function $F(B)$ is the calibration function mapping the sampled data to velocities U_i,

$$U_i = F(B_i) \tag{38}$$

this gives the expression for the mean,

$$\overline{U} = E(U) = \sum_{j=1}^{4096} F(b_j) P_j. \tag{39}$$

With $u_j = F(B_j) - \overline{U}$ then the variance can be expressed as,

$$\overline{u^2} = E((U - \overline{U})^2) = \sum_{j=1}^{4096} u_j^2 P_j, \tag{40}$$

the skewness,

$$S(U) = \frac{\overline{u^3}}{\overline{u^2}^{3/2}} = \frac{1}{\overline{u^2}^{3/2}} \sum_{j=1}^{4096} u_j^3 P_j, \tag{41}$$

and the flatness,

$$F(U) = \frac{\overline{u^4}}{\overline{u^2}^2} = \frac{1}{\overline{u^2}^2} \sum_{j=1}^{4096} u_j^4 P_j. \tag{42}$$

The described method is computationally very efficient since only a sum over 4096 values needs to be computed for every moment instead of a sum over the whole data set. The probability density function was generated in real time which made it possible to monitor the progress of the measurement without any delays.

6.1.2. *Moments from double-wire data.* For the calculation of statistical moments from the double-wire data another method was used since generating a 2-D (4096^2) discrete probability density function and using the same method as for the single-wire data would be very inefficient.

The calculation of these moments was instead done using a binomial expansion of the definitions shown in the expressions 43–45, to give the variance

$$\overline{u^2} = \frac{1}{N} \sum_{i=1}^{N} \left(U_i - \overline{U} \right)^2 = \frac{1}{N} \sum_{i=1}^{N} U_i^2 - \overline{U}^2, \tag{43}$$

skewness

$$\begin{aligned}
S(U) &= \frac{\overline{u^3}}{\overline{u^2}^{3/2}} = \frac{1}{N} \sum_{i=1}^{N} \left(\frac{U_i - \overline{U}}{\sqrt{\overline{u^2}}} \right)^3 \\
&= \frac{1}{\overline{u^2}^{3/2}} \left[2\overline{U}^3 + \frac{1}{N} \sum_{i=1}^{N} U_i^3 - \frac{3\overline{U}}{N^2} \sum_{i=1}^{N} U_i^2 \right],
\end{aligned} \tag{44}$$

and flatness

$$\begin{aligned}
F(U) &= \frac{\overline{u^4}}{\overline{u^2}^2} = \frac{1}{N} \sum_{i=1}^{N} \left(\frac{U_i - \overline{U}}{\sqrt{\overline{u^2}}} \right)^4 \\
&= \frac{1}{\overline{u^2}^2} \left[\frac{1}{N} \sum_{i=1}^{N} U_i^4 - \frac{4\overline{U}}{N} \sum_{i=1}^{N} U_i^3 + \frac{6\overline{U}^2}{N} \sum_{i=1}^{N} U_i^2 - 3\overline{U}^4 \right].
\end{aligned} \tag{45}$$

The cross-correlation was calculated using,

$$\overline{uv} = \frac{1}{N} \sum_{i=1}^{N} u_i v_i - \overline{U}\,\overline{V}. \tag{46}$$

These expanded versions was chosen because the sums of U, U^2, U^3 and U^4 for each velocity component plus the cross sum of uv can be calculated with one sweep through the data set.

6.2. *Power spectral estimation*

Estimation of auto spectral density functions was done using a direct FFT calculation procedure. The sampled time series, with the mean removed,

$$u_m \equiv u(t_m), \qquad t_m \equiv (m-1)\Delta t, \qquad m = 1, 2, \ldots, M \qquad (47)$$

with a total length of T_r was divided into n_d contiguous segments each of length T, giving

$$u_{in} \equiv u(t_{in}), \qquad (48)$$

$$t_{in} = ((i-1)N + (n-1))\Delta t \qquad (49)$$

$$i = 1, 2, \ldots, n_d, \qquad n = 1, 2, \ldots, N \qquad (50)$$

Use the discrete Fourier transform,

$$\widehat{u}_{ik} = \sum_{n=1}^{N} u_{in} e^{2\pi i (k-1)(n-1)/N} \qquad k = 1, 2, \ldots, N. \qquad (51)$$

to define the so called one-sided periodogram estimate of the power spectrum,

$$P_{ik} = \frac{a_k}{N^2} |\widehat{u}_{ik}|^2, \qquad k = 1, 2, \ldots, N/2 + 1 \qquad (52)$$

where,

$$a_k = \begin{cases} 1 & \text{if k=1 or k=N/2+1} \\ 2 & \text{otherwise} \end{cases} \qquad (53)$$

and

$$f_k \equiv \frac{k-1}{N\Delta t} = 2f_c \frac{k-1}{N} \qquad k = 1, 2, \ldots, \frac{N}{2} + 1. \qquad (54)$$

The periodogram has the property that its sum equals the variance of the signal. Using Parsevals relation,

$$\sum_{k=1}^{N/2+1} P_{ik} = \frac{1}{N} \sum_{n=1}^{N} |u_{in}|^2 = \overline{u^2} \qquad (55)$$

The one-sided auto spectral function can now be calculated by averaging the segments,

$$G_{uu}(f_k) = \frac{\Delta t N}{n_d} \sum_{i=1}^{n_d} P_{ik}. \qquad (56)$$

6.3. *Autocorrelation estimation*

The auto correlation function is defined as,

$$R_{uu}(r\Delta t) = \frac{1}{N-r} \sum_{n=1}^{N-r} u_n u_{n+r}, \qquad r = 1, 2, \ldots, m, \qquad (57)$$

where N is the record length, r the lag number and m the maximum lag number, $m < N$. The autocorrelation function was not calculated using the definition, instead the autocorrelation was determined via FFT.

6.4. *Storage and data structures*

The digitized data and the corresponding experimental parameters were stored in a number of data bases with similar structures. The whole data base is available on the Department of Mechanics web server at the address: `http://www.mech.kth.se/~jens/zpg/`.

6.4.1. *Single wire data base.* During the measurement the main program stores the digitized data in four kinds of files: one header file (text) containing all the experimental parameters, one binary file containing the probability density distributions generated from the data, n_j in equation 37, one binary file for each point in the boundary layer containing the actual time series and finally one text file with the calculated statistics. Another format is available for users of MATLAB. During the evaluation process the header and statistics files of all single wire measurements were processed into an array of structures containing all 80 measurements. This format is very handy for interactive work while it allows the user to have access to all data at the same time.

The experimental parameters of all single-wire measurements are gathered in tables 3 to 12.

6.4.2. *X- and V-wire data bases.* In tables 13, 14 and 15 the flow parameters for the X-and V-wire experiments are presented. The X- and V-wire programs generated three kinds of output files: one text file containing the experimental parameters, one binary file for each position in the boundary layer containing the digitized time series of the anemometer signal from the two wires and one file with statistics calculated from a subset of the time series (to speed up the measurement) for monitoring purpose. The final statistics were calculated after the experiment using the expressions in section 6.1.2.

6.4.3. *Double hot-film data base.* The double hot-film measurement program generated three kinds of files: again one text file containing all experimental parameters, one binary file containing the digitized time series from the anemometer signal from the two hot-films, one file containing the probability density distributions, and one text statistics file.

index			1	2	3	4	5	6	7
Name			SW981129A	SW981129B	SW981129C	SW981129D	SW981129E	SW981129F	SW981129G
X	m		1.5	1.5	1.5	1.5	1.5	1.5	1.5
U_∞	m/s		10.6	13.4	16.2	21.8	27.3	32.7	37.9
U_τ	m/s		0.43	0.54	0.64	0.84	1.03	1.22	1.40
c_f			3.35e-03	3.22e-03	3.10e-03	2.96e-03	2.86e-03	2.79e-03	2.72e-03
Re_θ			2533	3058	3651	4613	5486	6263	7147
θ	m		3.5e-03	3.3e-03	3.2e-03	3.0e-03	2.9e-03	2.8e-03	2.7e-03
δ^*	m		4.9e-03	4.7e-03	4.6e-03	4.3e-03	4.0e-03	3.8e-03	3.7e-03
H			1.4e+00	1.4e+00	1.4e+00	1.4e+00	1.4e+00	1.4e+00	1.4e+00
Δ	m		1.2e-01	1.2e-01	1.2e-01	1.1e-01	1.1e-01	1.0e-01	1.0e-01
δ	m		2.3e-02	2.2e-02	2.1e-02	2.0e-02	1.9e-02	1.9e-02	1.8e-02
δ^+			684	801	929	1162	1384	1579	1780
d_{wire}	m		1.25e-06	1.25e-06	1.25e-06	1.25e-06	1.25e-06	1.25e-06	1.25e-06
l_{wire}	m		2.50e-04	2.50e-04	2.50e-04	2.50e-04	2.50e-04	2.50e-04	2.50e-04
l_{wire}^+			7.5	9.3	11.1	14.5	17.9	21.1	24.3
f_s	Hz		40000.0	40000.0	40000.0	40000.0	40000.0	40000.0	40000.0
T_r	s		33.7	33.7	33.7	33.7	33.7	33.7	33.7

TABLE 3. Single-wire measurements (continued).

index		8	9	10	11	12	13	14
Name		SW981129H	SW981129I	SW981129J	SW981128A	SW981128B	SW981128C	SW981128D
X	m	1.5	1.5	1.5	2.5	2.5	2.5	2.5
U_∞	m/s	43.2	48.5	53.7	10.4	13.2	16.0	21.5
U_τ	m/s	1.58	1.75	1.91	0.41	0.51	0.61	0.80
c_f		2.66e-03	2.61e-03	2.54e-03	3.10e-03	3.00e-03	2.89e-03	2.76e-03
Re_θ		7981	8873	10162	3654	4312	5156	6511
θ	m	2.7e-03	2.6e-03	2.7e-03	5.2e-03	4.8e-03	4.7e-03	4.4e-03
δ^*	m	3.6e-03	3.6e-03	3.6e-03	7.2e-03	6.7e-03	6.6e-03	6.1e-03
H		1.4e+00	1.4e+00	1.3e+00	1.4e+00	1.4e+00	1.4e+00	1.4e+00
Δ	m	9.9e-02	9.9e-02	1.0e-01	1.8e-01	1.7e-01	1.7e-01	1.6e-01
δ	m	1.8e-02	1.8e-02	1.8e-02	3.3e-02	3.1e-02	3.1e-02	2.9e-02
δ^+		1990	2188	2385	918	1092	1270	1594
d_wire	m	1.25e-06	1.25e-06	1.25e-06	1.25e-06	1.25e-06	1.25e-06	1.25e-06
l_wire	m	2.50e-04	2.50e-04	2.50e-04	2.50e-04	2.50e-04	2.50e-04	2.50e-04
l^+_wire		27.4	30.4	33.2	7.0	8.7	10.4	13.6
f_s	Hz	40000.0	40000.0	40000.0	40000.0	40000.0	40000.0	40000.0
T_r	s	33.7	33.7	33.7	33.7	33.7	33.7	33.7

TABLE 4. Single-wire measurements (continued).

index		15	16	17	18	19	20	21
Name		SW981128E	SW981128F	SW981128G	SW981128H	SW981128I	SW981128J	SW981127H
X	m	2.5	2.5	2.5	2.5	2.5	2.5	3.5
U_∞	m/s	26.9	32.2	37.4	42.8	47.9	53.2	10.3
U_τ	m/s	0.98	1.16	1.33	1.50	1.67	1.84	0.40
c_f		2.66e-03	2.59e-03	2.53e-03	2.48e-03	2.43e-03	2.39e-03	2.95e-03
Re_θ		7970	9112	10314	11733	12867	14290	4705
θ	m	4.3e-03	4.1e-03	4.0e-03	4.0e-03	3.9e-03	3.9e-03	6.6e-03
δ^*	m	5.9e-03	5.6e-03	5.4e-03	5.4e-03	5.2e-03	5.2e-03	9.2e-03
H		1.4e+00	1.4e+00	1.3e+00	1.3e+00	1.3e+00	1.3e+00	1.4e+00
Δ	m	1.6e-01	1.6e-01	1.5e-01	1.5e-01	1.5e-01	1.5e-01	2.4e-01
δ	m	2.9e-02	2.8e-02	2.7e-02	2.7e-02	2.7e-02	2.7e-02	4.3e-02
δ^+		1919	2198	2477	2780	3045	3342	1166
d_{wire}	m	1.25e-06	1.25e-06	1.25e-06	1.25e-06	1.25e-06	1.25e-06	1.25e-06
l_{wire}	m	2.50e-04	2.50e-04	2.50e-04	2.50e-04	2.50e-04	2.50e-04	2.50e-04
l^+_{wire}		16.8	19.8	22.8	25.7	28.5	31.4	6.8
f_s	Hz	40000.0	40000.0	40000.0	40000.0	40000.0	40000.0	40000.0
T_r	s	33.7	33.7	33.7	33.7	33.7	33.7	33.7

TABLE 5. Single-wire measurements (continued).

index		22	23	24	25	26	27	28
Name		SW981127I	SW981127J	SW981127K	SW981127L	SW981127M	SW981127N	SW981127O
X	m	3.5	3.5	3.5	3.5	3.5	3.5	3.5
U_∞	m/s	13.1	15.9	21.4	27.0	32.4	37.7	43.0
U_τ	m/s	0.49	0.59	0.78	0.96	1.14	1.31	1.48
c_f		2.83e-03	2.74e-03	2.62e-03	2.53e-03	2.46e-03	2.40e-03	2.35e-03
Re_θ		5747	6769	8634	10502	12240	13878	15512
θ	m	6.4e-03	6.2e-03	5.8e-03	5.6e-03	5.5e-03	5.3e-03	5.2e-03
δ^*	m	8.8e-03	8.5e-03	8.0e-03	7.6e-03	7.3e-03	7.1e-03	6.9e-03
H		1.4e+00	1.4e+00	1.4e+00	1.4e+00	1.3e+00	1.3e+00	1.3e+00
Δ	m	2.3e-01	2.3e-01	2.2e-01	2.1e-01	2.1e-01	2.0e-01	2.0e-01
δ	m	4.1e-02	4.0e-02	3.8e-02	3.7e-02	3.7e-02	3.6e-02	3.6e-02
δ^+		1383	1613	2045	2462	2872	3257	3633
d_wire	m	1.25e-06	1.25e-06	1.25e-06	1.25e-06	1.25e-06	1.25e-06	1.25e-06
l_wire	m	2.50e-04	2.50e-04	2.50e-04	2.50e-04	2.50e-04	2.50e-04	2.50e-04
l^+_wire		8.5	10.1	13.4	16.5	19.6	22.5	25.4
f_s	Hz	40000.0	40000.0	40000.0	40000.0	40000.0	40000.0	40000.0
T_r	s	33.7	33.7	33.7	33.7	33.7	33.7	33.7

TABLE 6. Single-wire measurements (continued).

index		29	30	31	32	33	34	35
Name		SW981127P	SW981127Q	SW981126C	SW981126D	SW981126E	SW981127A	SW981127B
X	m	3.5	3.5	4.5	4.5	4.5	4.5	4.5
U_∞	m/s	48.4	53.6	10.4	13.1	15.8	21.2	26.9
U_τ	m/s	1.64	1.81	0.39	0.48	0.58	0.75	0.94
c_f		2.31e-03	2.28e-03	2.84e-03	2.73e-03	2.65e-03	2.53e-03	2.43e-03
Re_θ		17280	18720	5689	6931	8105	10387	12886
θ	m	5.2e-03	5.1e-03	8.0e-03	7.7e-03	7.5e-03	7.1e-03	7.0e-03
δ^*	m	6.8e-03	6.6e-03	1.1e-02	1.0e-02	1.0e-02	9.6e-03	9.3e-03
H		1.3e+00	1.3e+00	1.4e+00	1.4e+00	1.4e+00	1.3e+00	1.3e+00
Δ	m	2.0e-01	2.0e-01	2.9e-01	2.8e-01	2.8e-01	2.7e-01	2.7e-01
δ	m	3.5e-02	3.5e-02	5.1e-02	5.0e-02	4.8e-02	4.7e-02	4.6e-02
δ^+		4006	4367	1381	1661	1917	2432	2968
d_{wire}	m	1.25e-06	1.25e-06	1.25e-06	1.25e-06	1.25e-06	1.25e-06	1.25e-06
l_{wire}	m	2.50e-04	2.50e-04	2.50e-04	2.50e-04	2.50e-04	2.50e-04	2.50e-04
l_{wire}^+		28.3	31.2	6.7	8.3	9.9	12.9	16.1
f_s	Hz	40000.0	40000.0	29940.1	29940.1	29940.1	29940.1	40000.0
T_r	s	33.7	33.7	45.1	45.1	45.1	45.1	33.7

TABLE 7. Single-wire measurements (continued).

index		36	37	38	39	40	41	42
Name		SW981127C	SW981127D	SW981127E	SW981127F	SW981127G	SW981005A	SW981005B
X	m	4.5	4.5	4.5	4.5	4.5	5.5	5.5
U_∞	m/s	32.4	37.8	43.3	48.7	52.6	21.4	15.9
U_τ	m/s	1.11	1.29	1.46	1.63	1.75	0.75	0.57
c_f		2.37e-03	2.31e-03	2.27e-03	2.23e-03	2.20e-03	2.44e-03	2.56e-03
Re_θ		14973	17102	19235	20958	22579	12633	9707
θ	m	6.7e-03	6.6e-03	6.5e-03	6.3e-03	6.3e-03	8.6e-03	8.9e-03
δ^*	m	8.9e-03	8.7e-03	8.5e-03	8.2e-03	8.1e-03	1.2e-02	1.2e-02
H		1.3e+00	1.3e+00	1.3e+00	1.3e+00	1.3e+00	1.3e+00	1.3e+00
Δ	m	2.6e-01	2.6e-01	2.5e-01	2.4e-01	2.4e-01	3.3e-01	3.3e-01
δ	m	4.5e-02	4.5e-02	4.4e-02	4.3e-02	4.3e-02	5.7e-02	5.8e-02
δ^+		3457	3944	4418	4856	5197	2903	2272
d_{wire}	m	1.25e-06	1.25e-06	1.25e-06	1.25e-06	1.25e-06	1.27e-06	1.27e-06
l_{wire}	m	2.50e-04	2.50e-04	2.50e-04	2.50e-04	2.50e-04	2.50e-04	2.50e-04
l_{wire}^+		19.1	22.1	25.0	27.9	30.0	12.8	9.8
f_s	Hz	40000.0	40000.0	40000.0	40000.0	40000.0	29940.1	29940.1
T_r	s	33.7	33.7	33.7	33.7	33.7	35.0	35.0

TABLE 8. Single-wire measurements (continued).

index		43	44	45	46	47	48	49
Name		SW981005C	SW981005D	SW981005E	SW981005F	SW981006A	SW981006B	SW981006C
X	m	5.5	5.5	5.5	5.5	5.5	5.5	5.5
U_∞	m/s	13.1	10.4	26.8	32.2	37.4	42.5	48.3
U_τ	m/s	0.48	0.39	0.92	1.09	1.25	1.41	1.58
c_f		2.65e-03	2.75e-03	2.36e-03	2.29e-03	2.25e-03	2.20e-03	2.15e-03
Re_θ		8209	6700	15182	17901	20258	22846	25779
θ	m	9.1e-03	9.3e-03	8.2e-03	8.1e-03	7.9e-03	7.8e-03	7.8e-03
δ^*	m	1.2e-02	1.3e-02	1.1e-02	1.1e-02	1.0e-02	1.0e-02	1.0e-02
H		1.4e+00	1.4e+00	1.3e+00	1.3e+00	1.3e+00	1.3e+00	1.3e+00
Δ	m	3.4e-01	3.4e-01	3.2e-01	3.1e-01	3.1e-01	3.1e-01	3.1e-01
δ	m	5.9e-02	6.1e-02	5.5e-02	5.4e-02	5.4e-02	5.3e-02	5.3e-02
δ^+		1947	1612	3480	4067	4626	5167	5769
d_wire	m	1.27e-06	1.27e-06	1.27e-06	1.27e-06	1.27e-06	1.27e-06	1.27e-06
l_wire	m	2.50e-04	2.50e-04	2.50e-04	2.50e-04	2.50e-04	2.50e-04	2.50e-04
l^+_wire		8.2	6.7	15.8	18.8	21.6	24.3	27.2
f_s	Hz	29940.1	29940.1	29940.1	29940.1	29940.1	40000.0	40000.0
T_r	s	35.0	35.0	35.0	35.0	35.0	26.2	26.2

TABLE 9. Single-wire measurements (continued).

index		50	51	52	53	54	55	56
Name		SW981008A	SW981008B	SW981008C	SW981008D	SW981012A	SW981012B	SW981012C
X	m	5.5	5.5	5.5	5.5	5.5	5.5	5.5
U_∞	m/s	52.2	46.5	40.0	45.3	36.7	31.7	26.5
U_τ	m/s	1.71	1.53	1.34	1.50	1.24	1.08	0.92
c_f		2.14e-03	2.18e-03	2.23e-03	2.19e-03	2.28e-03	2.33e-03	2.39e-03
Re_θ		26612	23870	21099	23120	18480	16422	14207
θ	m	7.5e-03	7.5e-03	7.7e-03	7.5e-03	7.6e-03	7.9e-03	8.1e-03
δ^*	m	9.7e-03	9.8e-03	1.0e-02	9.7e-03	1.0e-02	1.0e-02	1.1e-02
H		1.3e+00	1.3e+00	1.3e+00	1.3e+00	1.3e+00	1.3e+00	1.3e+00
Δ	m	3.0e-01	3.0e-01	3.0e-01	2.9e-01	3.0e-01	3.0e-01	3.1e-01
δ	m	5.2e-02	5.2e-02	5.3e-02	5.2e-02	5.3e-02	5.4e-02	5.5e-02
δ^+		6019	5443	4828	5304	4300	3822	3313
d_{wire}	m	1.27e-06	1.27e-06	1.27e-06	1.27e-06	1.27e-06	1.27e-06	1.27e-06
l_{wire}	m	2.50e-04	2.50e-04	2.50e-04	2.50e-04	2.50e-04	2.50e-04	2.50e-04
l_{wire}^+		29.2	26.2	22.8	25.6	20.4	17.8	15.1
f_s	Hz	40000.0	40000.0	40000.0	40000.0	40000.0	40000.0	40000.0
T_r	s	26.2	26.2	26.2	26.2	26.2	26.2	26.2

TABLE 10. Single-wire measurements (continued).

index		57	58	59	60	61	62	63
Name		SW981013A	SW981013B	SW981013C	SW981013D	SW981112A	SW981112B	SW981112C
X	m	5.5	5.5	5.5	5.5	5.5	5.5	5.5
U_∞	m/s	21.4	16.0	10.5	13.3	10.4	13.1	15.8
U_τ	m/s	0.75	0.57	0.39	0.48	0.38	0.48	0.57
c_f		2.46e-03	2.57e-03	2.74e-03	2.64e-03	2.75e-03	2.65e-03	2.57e-03
Re_θ		12150	9601	6765	8299	6662	8105	9557
θ	m	8.5e-03	8.9e-03	9.6e-03	9.3e-03	9.4e-03	9.1e-03	8.9e-03
δ^*	m	1.1e-02	1.2e-02	1.3e-02	1.3e-02	1.3e-02	1.2e-02	1.2e-02
H		1.3e+00	1.4e+00	1.4e+00	1.4e+00	1.4e+00	1.4e+00	1.4e+00
Δ	m	3.2e-01	3.4e-01	3.6e-01	3.5e-01	3.5e-01	3.4e-01	3.3e-01
δ	m	5.6e-02	5.8e-02	6.1e-02	5.9e-02	6.1e-02	5.9e-02	5.8e-02
δ^+		2824	2238	1602	1917	1598	1922	2241
d_{wire}	m	1.27e-06	1.27e-06	1.27e-06	1.27e-06	2.50e-06	2.50e-06	2.50e-06
l_{wire}	m	2.50e-04	2.50e-04	2.50e-04	2.50e-04	5.00e-04	5.00e-04	5.00e-04
l_{wire}^+		12.6	9.6	6.6	8.1	13.1	16.3	19.3
f_s	Hz	29940.1	29940.1	29940.1	29940.1	29940.1	29940.1	29940.1
T_r	s	35.0	35.0	35.0	70.0	45.1	45.1	

TABLE 11. Single-wire measurements (continued).

index			64	65	66	67	68	69	70
Name			SW981112D	SW981113A	SW981113B	SW981113C	SW981113D	SW981113E	SW981113F
X		m	5.5	5.5	5.5	5.5	5.5	5.5	5.5
U_∞		m/s	21.2	26.9	32.4	37.9	43.6	49.1	54.0
U_τ		m/s	0.74	0.92	1.10	1.27	1.44	1.61	1.76
c_f			2.45e-03	2.36e-03	2.30e-03	2.24e-03	2.19e-03	2.15e-03	2.13e-03
Re_θ			12309	15165	17813	20562	23310	25767	27320
θ		m	8.5e-03	8.3e-03	8.1e-03	8.0e-03	7.9e-03	7.7e-03	7.5e-03
δ^*		m	1.1e-02	1.1e-02	1.1e-02	1.0e-02	1.0e-02	1.0e-02	9.6e-03
H			1.3e+00	1.3e+00	1.3e+00	1.3e+00	1.3e+00	1.3e+00	1.3e+00
Δ		m	3.2e-01	3.2e-01	3.2e-01	3.1e-01	3.1e-01	3.1e-01	2.9e-01
δ		m	5.6e-02	5.5e-02	5.4e-02	5.4e-02	5.4e-02	5.3e-02	5.1e-02
δ^+			2851	3461	4049	4642	5245	5780	6147
d_{wire}		m	2.50e-06	2.50e-06	2.50e-06	2.50e-06	2.50e-06	2.50e-06	2.50e-06
l_{wire}		m	5.00e-04	5.00e-04	5.00e-04	5.00e-04	5.00e-04	5.00e-04	5.00e-04
l^+_{wire}			25.4	31.4	37.3	43.0	48.9	54.7	59.8
f_s		Hz	29940.1	40000.0	40000.0	40000.0	40000.0	40000.0	40000.0
T_r		s							

TABLE 12. Single-wire measurements (continued).

	Index	1	2	3	4	5
	Name	XW981116A	XW981117A	XW981117B	XW981117C	XW981117D
X	m	5.5	5.5	5.5	5.5	5.5
U_∞	m/s	10.4	13.1	15.8	18.5	21.2
U_τ	m/s	0.38	0.47	0.56	0.65	0.74
Re_θ		6928	8389	9771	11150	12501
θ	m	9.7e-03	9.3e-03	9.0e-03	8.7e-03	8.6e-03
δ^*	m	1.3e-02	1.3e-02	1.2e-02	1.2e-02	1.1e-02
Δ	m	3.6e-01	3.5e-01	3.4e-01	3.3e-01	3.3e-01
δ	m	6.3e-02	6.1e-02	5.9e-02	5.8e-02	5.7e-02
δ^+		1676	2002	2310	2618	2919
d_{wire}	m	1.27e-06	1.27e-06	1.27e-06	1.27e-06	1.27e-06
l_{wire}	m	3.00e-04	3.00e-04	3.00e-04	3.00e-04	3.00e-04
l^+_{wire}		7.9	9.8	11.7	13.5	15.3
f_s	Hz	29940.1	29940.1	29940.1	29940.1	29940.1
T_r	s	68.4	68.4	68.4	68.4	68.4

TABLE 13. X-wire measurements.

Index		6	7	8	9
Name		XW981118A	XW981118B	XW981118C	XW981118D
X	m	5.5	5.5	5.5	5.5
U_∞	m/s	26.5	31.8	37.0	42.3
U_τ	m/s	0.91	1.08	1.25	1.41
Re_θ		15094	17621	20078	22528
θ	m	8.3e-03	8.0e-03	7.9e-03	7.7e-03
δ^*	m	1.1e-02	1.1e-02	1.0e-02	1.0e-02
Δ	m	3.2e-01	3.1e-01	3.1e-01	3.0e-01
δ	m	5.6e-02	5.5e-02	5.4e-02	5.3e-02
δ^+	m	3497	4061	4609	5156
d_{wire}	m	1.27e-06	1.27e-06	1.27e-06	1.27e-06
l_{wire}	m	3.00e-04	3.00e-04	3.00e-04	3.00e-04
l^+_{wire}		18.8	22.3	25.8	29.2
f_s	Hz	29940.1	40000.0	40000.0	40000.0
T_r	s	68.4	51.2	51.2	51.2

TABLE 14. X-wire measurements.

Index		1	2	3	4	5	6	7
Name		VW981119A	VW981119B	VW981119C	VW981119D	VW981121A	VW981121B	VW981122A
X	m	5.5	5.5	5.5	5.5	5.5	5.5	5.5
U_∞	m/s	10.4	13.2	15.9	21.4	26.4	31.1	35.7
U_τ	m/s	0.38	0.48	0.57	0.75	0.91	1.06	1.20
Re_θ		6976	8500	9953	12748	15117	17401	19532
θ	m	9.7e-03	9.2e-03	8.9e-03	8.5e-03	8.3e-03	8.1e-03	7.9e-03
δ^*	m	1.3e-02	1.3e-02	1.2e-02	1.1e-02	1.1e-02	1.1e-02	1.0e-02
Δ	m	3.6e-01	3.5e-01	3.4e-01	3.3e-01	3.2e-01	3.1e-01	3.1e-01
δ	m	6.3e-02	6.1e-02	5.9e-02	5.7e-02	5.6e-02	5.5e-02	5.4e-02
δ^+		1686	2026	2350	2974	3503	4012	4487
d_wire	m	1.27e-06	1.27e-06	1.27e-06	1.27e-06	1.27e-06	1.27e-06	1.27e-06
l_wire	m	3.00e-04	3.00e-04	3.00e-04	3.00e-04	3.00e-04	3.00e-04	3.00e-04
l^+_wire		8.0	10.0	11.9	15.6	18.9	22.0	25.0
f_s	Hz	29940.1	29940.1	29940.1	29940.1	40000.0	40000.0	40000.0
T_r	s	68.4	68.4	68.4	68.4	51.2	51.2	51.2

TABLE 15. V-wire measurements.

7. Appendix: Measurements of shear stress using a floating-element sensor from MIT

Only a few direct wall-shear stress measurement methods exist. One is to measure the tangential force on a small part of the wall, a *floating-element* technique. The wall-shear stress is then determined by

$$\tau_w = \frac{F}{A} \tag{58}$$

where F is the force on the floating-element and A the area. At first this seems to be an ideal method since it does not rely on specific characteristics of on the flow field or the fluid properties. Unfortunately the problems connected with implementing this method usually outweighs the advantages (Karlsson 1980; Bertelrud 1972). The main sources of errors are, misalignment of the floating-element, gaps around the floating-element and pressure gradients

The relatively large area of the conventional floating element sensors, see *e.g.* Smith & Walker (1959) and Karlsson (1980), will give the average shear in that area. For measurements of the fluctuating wall-shear stress the floating element size has to be of the same order as the viscous length scale. Padmanabhan (1997) used micromachining technology to develop a floating element optical shutter and integrated photodiodes for measurements of the fluctuating wall-shear stress, with the dimensions 120μm $\times$ 120μm. The floating-element is suspended by four tethers, see figures 34 and 35. A pair of photodiodes are located under the floating-element on the leading and trailing edges. The sensor is subjected to uniform illumination from a light source. With zero shear stress the exposed areas of the photodiodes are the same and the differential photocurrent $\Delta I_{\mathrm{photo}}$ is also zero. The differential photocurrent is proportional to the wall-shear stress

$$\Delta I_{\mathrm{photo}} \propto \tau_w. \tag{59}$$

In a co-operation with A. Padmanabhan and Prof. K. Breuer at MIT the micro-machined sensor was tested in the zero pressure-gradient boundary layer set-up in the MTL wind tunnel at KTH. The micro machined floating element sensor was mounted flush with the boundary layer plate in the sensor insert at $x = 5.5$ m. A laser was mounted in a traversing system on the upper wall of the test section with the beam entering through a slit in the upper wall. The optimum laser position was determined for highest possible sensitivity. The signal from the laser diodes were connected to two low noise current amplifiers (Stanford research systems, SR570) and digitized. The differential photocurrent signal $\Delta I_{\mathrm{photo}}$ was then calibrated against the wall-shear stress determined by a Preston tube.

The following conclusions were drawn from the tests with the MIT sensor. Uniform illumination of the photodiodes was very difficult to achieve for different tunnel speeds. The relative position of the laser and the sensor changed
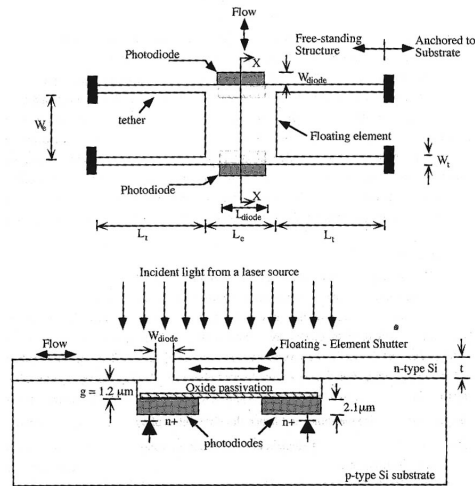
FIGURE 34. Schematic diagram illustrating the sensing principle (Padmanabhan 1997).

and resulted in a large variation in the photocurrent signals from the diodes. The displacements is believed to be caused by small changes in pressure and skin-friction on the plate and tunnel walls introduced by the change in tunnel speed during the calibration process. It was therefore impossible to make a meaningful calibration of the sensor. The general impression is that it is unsuitable to have the light source and the sensor separated a large distance making the system extremely sensitive to vibrations and small displacements caused by e.g. aerodynamic forces or thermal elongation. Future improvements should possibly include incorporating the light source into the sensor.
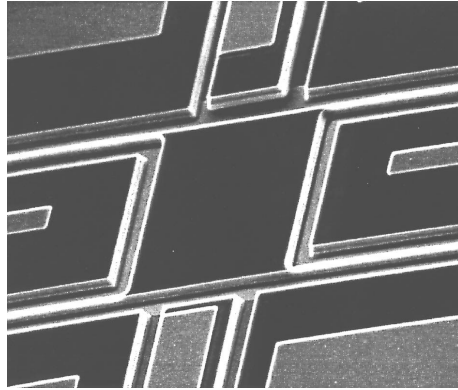
FIGURE 35. Scanning electron photograph of a floating element sensor, active area 120μm $\times$ 120μm (Padmanabhan 1997).

References

ALFREDSSON, P. H., JOHANSSON, A. V., HARITONIDIS, J. H. & ECKELMANN, H. 1988 The fluctuation wall-shear stress and the velocity field in the viscous sub-layer. *Phys. Fluids A* **31**, 1026–33.

BECHERT, D. W. 1995 Calibration of preston tubes. *AIAA J.* **34** (1), 205–206.

BERTELRUD, A. 1972 Skin friction measurement techniques in incompressible turbulent flow – a literature survey. Technical Note FFA AU–726. The Aeronautical Research Institute of Sweden.

CLAUSER, F. H. 1954 Turbulent boundary layers in adverse pressure gradients. *J. Aero. Sci.* **21**, 91–108.

FERNHOLZ, H. H. 1971 Ein halbempirisches Gezetz für die Wandreibung in kompressiblen turbulenten Grenzschichten bei isothermer und adiabater Wand. *ZAMM* **51**, 148–149.

FERNHOLZ, H. H. & FINLEY, P. J. 1996 The incompressible zero-pressure-gradient turbulent boundary layer: An assessment of the data. *Prog. Aerospace Sci.* **32**, 245–311.

FERNHOLZ, H. H., JANKE, G., SCHOBER, M., WAGNER, P. M. & WARNACK, D. 1996 New developments and applications of skin-friction measuring techniques. *Meas. Sci. Technol.* **7**, 1396–1409.

HARITONIDIS, J. H. 1989 The measurement of wall shear stress. In *Advances in Fluid Mechanics Measurements.* (ed. M. Gad-el Hak), pp. 229–261. Springer-Verlag.

HO, C.-M. & TAI, Y.-C. 1998 Micro-electro-mechanical-systems (MEMS) and fluid flows. *Ann. Rev. Fluid Mech.* **30**, 579–612.

JANKE, G. 1994 Über die Grundlagen und einige Anwendungen der ölfilm-interferometrie zur Messung von Wandreibungsfeldern in luftströmungen. PhD thesis, Technische Universität Berlin.

JIANG, F., TAI, Y.-C., GUPTA, B., GOODMAN, R., TUNG, S., HUANG, J. B. & HO, C.-M. 1996 A surface-micromachined shear stress imager. In *1996 IEEE Micro Electro Mechanical Systems Workshop (MEMS '96)*, pp. 110–115.

JOHANSSON, A. V. 1992 A low speed wind-tunnel with extreme flow quality - design and tests. In *Prog. ICAS congress 1992*, pp. 1603–1611. ICAS-92-3.8.1.

KARLSSON, R. I. 1980 Studies of skin friction in turbulent boundary layers on smooth

and rough walls. PhD thesis, Department of Applied Thermo and Fluid Dynamics, Chalmers University of Technology, Göteborg, Sweden.

KOMMINAHO, J., LUNDBLADH, A. & JOHANSSON, A. V. 1996 Very large structures in plane turbulent couette flow. *J. Fluid Mech.* **320**, 259–285.

LINDGREN, B., ÖSTERLUND, J. M. & JOHANSSON, A. V. 1998 Measurement and calculation of guide vane performance in expanding bends for wind-tunnels. *Experiments in Fluids* **24**, 265–272.

MONSON, D. J. 1983 A nonintrusive laser interferometer method for the measurement of skin friction. *Experiments in Fluids* **1**, 15–22.

NAQWI, A. A. & REYNOLDS, W. C. 1991 Measurement of turbulent wall velocity gradients using cylindrical waves of laser light. *Experiments in Fluids* **10**, 257–266.

NISHIZAWA, N., MARUSIC, I., PERRY, A. E. & HORNUNG, H. G. 1998 Measurement of wall shear stress in turbulent boundary layers using an optical interferometry method. In *13th Australian Fluid Mechanics Conferance, Monash University, Melbourne, Australia.*

OBI, S., INOUE, K., FURUKAWA, T. & MASUDA, S. 1996 Experimental study on the statistics of wall shear stress in turbulent channel flows. *Int. J. Heat and Fluid Flow* **17**, 187–192.

ÖSTERLUND, J. M., JOHANSSON, A. V., NAGIB, H. M. & HITES, M. H. 1999 Wall shear stress measurements in high reynolds number boundary layers from two facilities. In *30th AIAA Fluid Dynamics Conference, Norfolk, VA.* AIAA paper 99-3814.

PADMANABHAN, A. 1997 Silicon micromachined sensors and sensor arrays for shear-stress measurements in aerodynamic flows. PhD thesis, Massachusetts Institute of Technology, FDLR TR 97–5.

PATEL, V. C. 1965 Calibration of the Preston tube and limitations on its use in pressure gradients. *J. R. Aero. Soc.* **23**, 185–208.

PRESTON, J. H. 1953 The determination of turbulent skin friction by means of Pitot tubes. *J. Fluid Mech.* **58**, 109–1215.

SAHLIN, A. & JOHANSSON, A. V. 1991 Design of guide vanes for minimizing the pressure loss in sharp bends. *Phys. Fluids A* **3**, 1934–1940.

SETO, J. & HORNUNG, H. G. 1993 Two-directional skin friction measurement utilizing a compact internally-mounted thin-liquid-film skin friction meter. AIAA paper 93-0180.

SKOTE, M., HENKES, R. & HENNINGSON, D. 1998 Direct numerical simulation of self-similar turbulent boundary layers in adverse pressure gradients. In *Flow, Turbulence and Combustion*, , vol. 60, pp. 47–85. Kluwer Academic Publishers.

SMITH, D. W. & WALKER, J. H. 1959 Skin-friction measurements in incompressible flow. NASA TR R-26.

SPALART, P. R. 1988 Direct simulation of a turbulent boundary layer up to $Re_\theta = 1410$. *J. Fluid Mech.* **187**, 61–98.

TANNER, L. H. & BLOWS, L. G. 1976 A study of the motion of oil films on surfaces in air flow, with application to the measurement of skin friction. *Journal of Physics E: Scientific Instruments* **9**, 194–202.

WINTER, K. G. 1977 An outline of the techniques available for the measurement of skin friction in turbulent boundary layers. *Prog. Aerospace. Sci.* **18**, 1–57.